eman ta zabal zazu

Universidad del País Vasco
Euskal Herriko Unibertsitatea

DOCTORAL THESIS

Magnetic and structural characterization of magnetite nanoparticles synthesized by magnetotactic bacteria

LOURDES MARCANO PRIETO

Supervisors:

M. LUISA FDEZ-GUBIEDA

ANA GARCÍA PRIETO

2018

Acknowledgements

Es díficil resumir en unas pocas líneas el reconocimiento que merecen todas aquellas personas que han contribuido de una u otra manera a esta tésis y han estado a mi lado estos últimos cuatro años. Así que, intentando no olvidar a nadie, vamos allá.

En primer lugar, gracias a mis directoras de tesis. A Malú, por *guiarme* y proporcionarme las herramientas necesarias para hacer lo que nos hemos propuesto. Por sentarte conmigo siempre que lo he necesitado pese a tener mil cosas más que hacer. A Ana, por tu organización envidiable y porque siempre que he necesitado algo te ha faltado el tiempo para ayudarme. A Alicia, por estar siempre disponible y por la paciencia que más de una vez has tenido que tener conmigo y con los cocos que me crecian hasta debajo de las piedras. Os daría las gracias por tantas cosas... La verdad es que por mi parte no podría haber pedido nada más. Me ha encantado compartir con vosotras esta etapa de mi vida no solo a nivel profesional, si no también a nivel personal.

Gracias Iñaki, ¡eso si que es paciencia! Gracias por sentarte conmigo y explicarme las cosas una y otra y otra vez. Y cuando por fin pensabas que lo había entendido y te dabas cuenta de que no era así, otra vez. De verdad Iñaki, muchas gracias, no me imagino nada de esto sin ti.

Gracias David por tener la santa paciencia de enseñarme a trabajar en un laboratorio de microbiología. Por estar ahí cada vez que he dudado con algún aparato o cultivo. Gracias por hacer más llevaderas las horas en la prensa y cada proceso de biomineralización.

Gracias Javi por portarte como un hermano mayor en más de una ocasión. Por ayudarme cuando lo he necesitado sin importar lo lejos que estuvieses.

Gracias al Grupo de Magnetismo y Materiales Magnéticos, ha sido un placer trabajar con vosotros. Gracias en general a todo el departamento de electricidad y electrónica. Gracias Alfredo, Galina, Manu, Jon, Patricia, Jorge, Esti y a todos los demás.

Gracias al grupo de Santander y en especial a Luis y a Philipp por su ayuda y colaboración.

Chicos, gracias a vosotros. Gracias Irati, Maite, Popi, Edu, Anabel, Javi, Libe, Iván, Óscar, Eneko Axpe, Catarina, Andoni, Jorge, Luca, Pablo, Dani, Eneko Garaio, David, Lucía, Inari, Iraultza, Mattin, Vasileios, Rosa... ¿Qué puedo decir? Me llevo los mejores amigos. Gracias por haber estado ahí día tras día.

Thanks to Sergio, Florian and Radu to made me feel very welcome at Berlin during my three-months stay.

A los Servivios Generales de Investigación, SGIker, por su disposición y accesibilidad. Gracias a Ricardo Andrade, a Alejandro Díez, a Mariano Barrado y a Juan Carlos Raposo.

Gracias al Gobierno Vasco y a la Universidad del País Vasco por proporcionarme la financiación necesaria para la realización de esta tesis.

Gracias a mi familia por ser el hombro en el que apoyarme. Gracias a mis padres por darme. Gracias a Manu, por aguantarme en el día a día, por estar a mi lado y levantarme cuando más me ha hecho falta. Gracias a Jon. A Co. Gracias a mis amigos, que habeis reido y llorado conmigo.

Gracias.

"Why, sometimes I've believed as many as six impossible things before breakfast"
Lewis Carroll, Through the Looking-Glass

A Julia

Contents

Resumen **3**

1 Magnetotactic Bacteria and Magnetosomes **9**
1.1 An introduction to magnetotactic bacteria 9
1.2 *Magnetospirillum gryphiswaldense* MSR-1 12
1.3 Magnetite structure 13
1.4 Applications 14
1.5 Motivation and Thesis structure 18

2 On the chain configuration: a magnetic and structural study **21**
2.1 Introduction 21
2.2 Growth conditions and magnetosome isolation 22
2.3 Electron cryotomography imaging (ECT) of the magnetosome chain . 23
2.4 Magnetism of magnetosome chains 25
2.4.1 Magnetization of a bacterial colloid 25
2.4.2 Small angle neutron/x-ray scattering (SANS/ SAXS) on a bacterial colloid 25
2.4.3 Magnetometry on 2D and 3D bacterial arrangements 29
2.4.4 X-ray photoemission electron microscopy (XPEEM) on extracted magnetosomes 35
2.5 Equilibrium configuration of the chain 38
2.6 Summary 41
Materials and Methods 44
List of publications resulting from this Chapter 48

3 Magnetosome biomineralization **49**
3.1 Introduction 49
3.2 Growth Conditions 51
3.3 Transmission electron microscopy (TEM) 53
3.4 X-ray absorption fine structure (XAFS) 55
3.4.1 X-ray Absorption Near Edge Structure (XANES) 55
3.4.2 Extended x-ray absorption fine structure (EXAFS) 60

3.5 High resolution TEM (HRTEM) . . . 65
3.6 Electron Energy Loss Spectroscopy (EELS) . . . 68
3.7 Proposal of biomineralization process . . . 71
Materials and Methods . . . 72
List of publications resulting from this Chapter . . . 76

4 Transition metal doping of magnetosomes 77
4.1 Introduction . . . 77
4.2 Magnetotactic bacteria cultures . . . 78
4.2.1 Minimum Inhibitory Concentration (MIC) assays . . . 78
4.2.2 Growth Conditions . . . 80
4.3 Structural Characterization . . . 81
4.3.1 Transmission Electron Microscopy (TEM) . . . 81
4.3.2 Energy-Dispersive X-ray Spectroscopy (EDS) . . . 83
4.3.3 X-ray Absorption Near Edge Structure (XANES) . . . 87
4.4 Magnetic Characterization . . . 91
4.4.1 Magnetization vs temperature, M(T) . . . 91
4.4.2 Magnetization vs magnetic field M(H) . . . 92
4.4.3 X-ray Magnetic Circular Dichroism (XMCD) on Co-doped magnetosomes . . . 94
4.4.4 Magnetic model of Co-doped magnetosome chains . . . 96
4.5 Summary . . . 101
Materials and Methods . . . 102
List of publications resulting from this Chapter . . . 104

Conclusions 105

Bibliography 107

List of figures 123

List of tables 129

Resumen

Las bacterias magnetotácticas son un grupo de microorganismos acuáticos presentes tanto en entornos marinos como de agua dulce. Aparecen con facilidad en zonas de transición oxi-anóxicas de regiones sedimentarias y columnas de agua estratificadas. Estos microorganismos buscan continuamente su posición óptima en el medio a fin de satisfacer sus necesidades fisicoquímicas y nutricionales. Su particularidad se encuentra precisamente en la capacidad de alinearse pasivamente en presencia del campo magnético terrestre (25-65 μT), gracias a la presencia intracelular de una o varias cadenas de orgánulos magnéticos conocidos como *magnetosomas*, mientras nadan activamente. Esta habilidad, conocida como *magnetotaxis*, permite a la bacteria reducir su búsqueda de nutrientes en las tres dimensiones a una búsqueda unidimensional definida por las líneas de campo magnético.

Estos microorganismos se observan por primera vez en los años 60 cuando Salvatore Bellini mirando a través de su microscopio una muestra de agua pantanosa recogida cerca de Pavia (Italia), encuentra un importante número de bacterias nadando todas ellas en una misma dirección. Bellini se refiere a estos microorganismos como *bacterias magnetosensibles* y postula la presencia de una 'brújula biomagnética' en su interior como responsable de este comportamiento. El descubrimiento de Bellini queda reflejado exclusivamente en unas notas publicadas en el Instituto de Microbiología de la Universidad de Pavia en 1963, pasando desapercibido en la comunidad científica. De hecho, estas notas no se traducirán hasta 2009, cuando son publicadas nuevamente y cobran visibilidad.

Pasará más de una década desde el hallazgo de Bellini hasta que se redescubra y publique la existencia de estos microorganismos. En 1975 Richard Blakemore observa y describe el comportamiento magnético en procariotas de sedimentos marinos. En esta ocasión Blakemore advierte de la presencia de un conjunto de partículas estructuradas y ricas en hierro rodeadas por una membrana que se encuentran formando cadenas en el citoplasma celular. Para referirse a estas partículas introduce por primera vez el término de *magnetosoma*. Vaticina además que los magnetosomas dotan a las células de un momento magnético el cual explicaría la migración de estos microorganismos en campos magnéticos tan débiles como lo es el campo magnético terrestre. Es en este trabajo también donde Blakemore acuña los términos de *bacterias magnetotácticas*, para referirse a estos curiosos micoorganismos, y *magnetotaxis*,

para su habilidad.

Tras la comunicación de Blakemore, aparece un interés creciente en áreas muy variadas de investigación en lo que a bacterias magnetotácticas y a sus magnetosomas se refiere. La razón es que las nanopartículas magnéticas que sintetizan las bacterias magnetotácticas gozan de excelentes propiedades totalmente reproducibles gracias al alto control genético impuesto en su síntesis. Dichas propiedades vienen definidas por la especie bacteriana en cuestión. Actualmente se conocen numerosas especies capaces de producir magnetosomas y responder al campo magnético, ya sean cocos, espirilos o bacilos. Dependiendo de la especie con la que trabajemos, podremos encontrar nanopartículas de distinta composición química -magnetita (Fe_3O_4) o greigita (Fe_3S_4)-, con distinta forma -cuboctaedrica, prismática, con forma de flecha...- y con distintos tamaños que van desde los 40 a los 120 nm, tratándose así de monodominios magnéticos térmicamente estables a temperaturas fisiológicas. A lo largo de esta tesis, hemos trabajado con la bacteria *Magnetospirillum gryphiswaldense*. Esta especie con forma de espirilo sintetiza una única cadena de 15-20 magnetosomas de magnetita con forma de cuboctaedros truncados y un tamaño medio de 40-45 nm de diámetro.

Las excepcionales propiedades de los magnetosomas hacen que sean candidatos ideales en numerosas aplicaciones tecnológicas y médicas. Además de tener una forma y tamaño uniforme, presentar una alta pureza química y un alto momento magnético térmicamente estable, los magnetosomas están rodeados por una membrana de naturaleza lipídica-proteica que les confiere estabilidad, evitando que se agreguen una vez extraidos, facilita su funcionalización y los hace biocompatibles. Por todo ello, los magnetosomas se convierten en nanopartículas ideales para aplicaciones biomédicas, en particular para el tratamiento contra el cáncer como son la hipertérmia magnética, la liberación de fármacos de forma controlada o como agentes de contraste en imagen en resonancia magnética nuclear. Así mismo, su alta calidad convierte a los magnetosomas en sistemas ideales para el estudio fundamental de nanoparticulas magnéticas.

A su vez, más allá de las interesantes propiedades de los magnetosomas como nanopartículas magnéticas *per se*, su disposición equiespaciada y ordenada en cadenas da lugar a sistemas unidimensionales modelo de gran atractivo físico y magnético. En los últimos años nace además la idea de usar la bacteria magnetotáctica en su conjunto en aplicaciones biomédicas, derivando en un interés en el estudio de la cadena. En dichas aplicaciones, el microorganismo jugaría el papel de un microrobot que navega a través del torrente sanguíneo de forma dirigida siguiendo la dirección de campos magnéticos aplicados externamente, aprovechando la cadena de magnetosomas para orientarse. De esta forma aumentaría la eficencia en la dirección y guiado del sistema magnético, facilitandose la liberación de fármacos de forma controlada y la hipertermia localizada.

Es precisamente en este contexto donde surge la presente Tesis. Para el uso potencial de magnetosomas y bacterias magnetotácticas, se precisa de una rigurosa caracterización magnética y estructural. Esto permitirá optimizar y explotar al máximo las excelentes propiedades de los magnetosomas y de las bacterias en las futuras aplicaciones.

Así, la Tesis se centra en el estudio de las cadenas de magnetosomas sintetizadas por la bacteria *Magnetosprillum gryphiswaldense*. Con este objetivo, el trabajo recoge resultados obtenidos mediante el uso de las técnicas habituales, disponibles en la mayoría de laboratorios, combinados con técnicas más sofisticadas disponibles exclusivamente en grandes instalaciones, como fuentes de radiación sincrotrón o neutrones. Esta conjunción de técnicas da lugar a una exhaustiva caracterización, escasa hasta la fecha y necesaria para la comprensión y la optimización del uso de magnetosomas y bacterias magnetotácticas en aplicaciones biomedicas.

El trabajo se divide en tres bloques principales precedidos por una breve introdución a las bacterias magnetotácticas, en concreto a la especie *Magnetosprillum gryphiswaldense*, y a los magnetosomas. El primero de estos bloques (Capítulo 2) analiza la configuración magnética de la cadena de magnetosomas y los mecanismos subyacentes que conducen a su forma helicoidal. El segundo bloque (Capítulo 3) se centra en el estudio del proceso de biomineralización que tiene lugar en la bacteria y que da lugar a los magnetosomas. Y, finalmente, el último bloque (Capítulo 4) está dirigido al estudio del dopaje de los magnetosomas con diferentes metales de transición mediante la modificación del proceso de biomineralización para la optimización de sus propiedades magnéticas. En las siguientes páginas se presenta brevemente cada uno de estos bloques, indicando el estado del arte en cada uno de los temas, la motivación que ha llevado al desarrollo de cada capítulo y los principales resultados obtenidos.

La cadena de magnetosomas constituye un paradigma natural en lo referente a nanostructuras magnéticas unidimensionales. Puesto que los magnetosomas son monodominios magnéticos, la cadena se comporta como un dipolo magnético permanente capaz de orientarse pasivamente en presencia de un campo magnético. Debido a su alta anisotropía magnética, la cadena de magnetosomas se convierte en un objeto de sumo interés para aplicaciones biomédicas, dispositivos actuadores o micro-robots.

Mediante criotomografía electrónica se ha observado que la cadena de magnetosomas lejos de ser una línea recta, como cabría esperar *a priori*, tiene una característica forma helicoidal. Este hecho revoluciona la comprensión de la cadena introduciendo nuevas cuestiones sobre la misma.

El Capítulo 2 analiza la relación entre la forma de la cadena y la respuesta mag-

nética de los magnetosomas. Para ello, se han utilizado diferentes técnicas en distintas configuraciones de bacterias. Mediante *small angle neutron/x-ray scattering* (SANS y SAXS, respectivamente), llevados a cabo en el ILL (Grenoble, Francia) e ISIS (Oxford, Reino Unido) en un coloide bacteriano; medidas mangnéticas convencionales (M(T) y M(H)) en sistemas de dos y tres dimensiones de bacterias orientadas a distintos ángulos con respecto al campo aplicado, y *x-ray photoemission electron microscopy* (XPEEM) realizado en BESSYII (Berlín, Alemania) sobre magnetosomas extraidos, hemos observado que el momento magnético de cada uno de los magnetosomas está desviado 20°de la dirección de la cadena (eje cristalográfico [111] de la magnetita).

Esta desviación es corresponsable de la helicidad de la cadena, que nace de la competencia de los mecanismos recuperadores de naturaleza lipidica y proteica que ejerce el citoesqueleto sobre la cadena de magnetosomas -entendidos como fuerzas elásticas- y la interacción magnética de carácter dipolar entre magnetosomas vecinos.

Tras el estudio de la configuración magnética de la cadena de magnetosomas, se da paso al análisis referente a la síntesis de los magnetosoma. El alto control genético ejercido por las bacterias magnetotácticas en la síntesis de magnetosomas hace del proceso de biomineralización un asunto de máximo interés en los distintos ámbitos científicos. Por una parte, las bacterias magnetotácticas constityen el sistema unicelular más sencillo en el que se observan procesos de biomineralización, ofreciendo un modelo sencillo para el estudio de los mecanismos involucrados en la biomineralización. Por otra parte, entender los mecanismos subyacentes del proceso, ayudaría al desarrollo de métodos de síntesis inorgánica de materiales similares. En particular, conocer cómo el microorganismo es capaz de controlar el proceso de formación y las propiedades, contribuiría al diseño de síntesis *in vitro* de nanopartículas magnéticas.

Hasta la fecha, la investigación en lo referente al proceso de biomineralización se ha centrado en la identificación de las proteinas y genes asociados al proceso. Sin embargo, pese a la gran labor que se ha hecho desde el punto de vista de lo biología, utilizando métodos de genética y proteómica, el proceso de formación de la magnetita desde un punto de vista estructural es un tema aún de debate.

El capítulo 3 de esta Tesis se enfrenta directamente al estudio del proceso de biomineralización de magnetosomas por la bacteria *Magnetospirillum gryphiswaldense*. Para ello se ha realizado una caracterización estructural en función del tiempo tras la incubación de la bacteria en un medio rico en Fe. Así, se han llevado a cabo medidas de absorción de rayos-x en el sincrotrón europeo ESRF (Grenoble, Francia), tanto *x-ray absorption near edge structure* (XANES) como *extended x-ray absorption fine structure* (EXAFS), microscopía electrónica de transmisión combinado con difracción de electrones en colaboración con el laboratorio de microscopías avanzadas de Aragón, y *electron energy loss spectroscopy* (EELS), en colaboración con Nanogune. El conjunto

de estas técnicas nos permite probar la coexistencia de dos fases a lo largo del proceso de biomineralización: bacterioferritina, una proteina de tipo ferrihidrita cuya función principal sería la acumulación de hierro, actuando como fuente de iones de Fe para la formación de los magnetosomas, y la magnetita, cuya presencia aumenta a medida que el proceso de biomineralización avanza y la presencia de magnetosomas va cobrando importancia. A partir de los resultados obtenidos y los datos encontrados en la bibliografía proponemos además un modelo para el proceso de biomineralización que va desde la captura del hierro ionico presente en el medio de cultivo hasta la formación de los magnetosomas de magnetita en estadio final.

Finalmente, el tercer bloque de la tesis se enfrenta a la caracterización magnética y estructural de magnetosomas dopados con distintos elementos de transición. Desde hace algo más de una década distintos grupos se han centrado en la modificación de las propiedades de los magnetosomas para así optimizar su posterior uso en las distintas aplicaciones. Así surge la idea de dopar los magnetosomas *in vivo* mediante la adición de los distintos elementos en el medio de cultivo. Es posiblemente la similitud entre iones la que da lugar a que pequeñas cantidades de cobalto o manganeso se incorporen en el magnetosoma mediante la sustitución de átomos de Fe durante el proceso de biomineralización.

El capítulo 4 recoge de esta forma el cultivo de la bacteria *M. gryphiswaldense* en presencia de Mn, Co, Ni, Cu y Zn. Mediante el uso de XANES (medidas realizadas en el ESRF), *energy-dispersive x-ray spectroscopy* (EDS) y *x-ray magnetic circular dichroism* (XMCD) (en BESSYII) hemos probado la incorporación de pequeñas cantidades de Mn y Co ($\sim 1\%$), mientras que no hemos encontrado evidencia de la presencia de Ni, Cu o Zn en la estructura de los magnetosomas. La incorporación de Mn y Co en los magnetosomas da lugar a cambios notables en su comportamiento magnético. Por una parte, la presencia de Mn origina una reducción del campo coercitivo de los magnetosomas. Por el contrario, la coercitividad de los magnetosomas, junto con su imanación remanente, aumenta con la incorporación de Co.

Centrándonos en el efecto del Co como dopante, hemos llevado a cabo una serie de simulaciones numéricas capaces de reproducir las medidas magnéticas experimentales. Basándonos en el modelo de Stoner-Wohlfarth, en este capítulo hemos analizado la evolución de los ciclos de histeresis en función de la temperatura. Esto nos ha permitido determinar las distintas contribuciones de anisotropía magnética y su evolución con la temperatura. Mientras que la anisotropía efectiva de las cadenas de magnetosomas no dopados es uniaxial en todo el rango de temperaturas que va de 300 a 5 K, la anisotropía efectiva de las cadenas de magnetosomas dopados con cobalto tiene una fuerte dependencia con la temperatura pasando de uniaxial -de 300 a 150 K-, a biaxial -hasta 100 K- y finalmente a triaxial por debajo de los 100 K.

Estos tres bloques ofrecen una descripción detallada de las cadenas de magnetosomas desde un punto magnético y estructural, desde su formación hasta la modificación de sus propiedades magnéticas mediante su dopaje con Co y Mn. Los aspectos físicos fundamentales que aquí se tratan, contribuyen a la optimización y posterior uso de magnetosomas y bacterias magnetotácticas en las distintas aplicaciones.

Chapter 1

Magnetotactic Bacteria and Magnetosomes

1.1 An introduction to magnetotactic bacteria

Magnetotactic bacteria (MTB) are able to passively align parallel to the Earth's geomagnetic field lines while they actively swim. This behavior, known as magnetotaxis, is due to the presence of unique intracellular magnetic organelles called magnetosomes[1–4]. The magnetosomes are intracellular inclusions composed by a core of magnetic iron mineral, typically magnetite (Fe_3O_4) or greigite (Fe_3S_4), enclosed by a thin membrane. Both MTB and magnetosomes spark interest among scientific community due to their special magnetic and structural characteristics that make them good candidates for nanotechnological applications[5–10]. The magnetotactic behavior in bacteria was first observed by Salvatore Bellini (1963)[11] in freshwater samples. He observed bacteria swimming northward persistently, and then suggested the presence of an internal magnetic compass responsible of the orientation of the cells. More than ten years later, R.P. Blakemore (1975)[12] observed the magnetic organelles within the bacterial cells and coined the term *magnetosome* to refer to them.

Magnetotactic bacteria are aquatic motile microorganisms widespread in freshwater and marine environments[13]. These microorganisms are easily detected in chemically and redox stratified sediments and water columns, predominantly at the oxic-anoxic transition zones (OATZ). Bacteria living in OATZ, with vertical chemical gradients, are continually searching the optimal position in the stratified water column in order to satisfy their nutritional requirements. Under these circumstances, magnetotaxis is thought to be a great advantage by increasing the efficiency of chemotaxis[1]. Due to inclination, the geomagnetic field lines act as vertical pathways in a stratified environment, therefore the bacteria aligned in the Earth field reduce a three dimensional search to a single dimension, swimming up-downwards the stratified column (Fig. 1.1). Another possible role of the magnetosomes has been suggested as detoxifying agents scavenging metal ions[14].

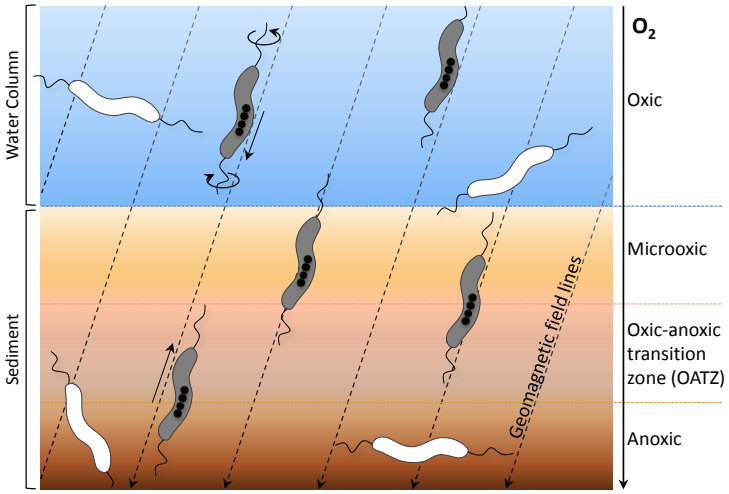

FIGURE 1.1: Schematic model of magnetotaxis in the oxic-anoxic transition zone (OATZ) (modified from Komeili et al.[15]). Magnetotactic bacteria (grey) swim along the Earth's field lines (one dimensional search). Other non-magnetotactic bacteria (white) swim randomly (three dimensional search).

At present, all the MTB described are motile gram-negative bacteria although they show a great diversity based on the morphology and physiology. The morphotypes observed, see Fig.1.2 (top), include curved (a), spirilla (b), cocci (c), rods (d) and even some colonial bacteria, which form multicellular aggregates[3,16]. The only signature trait they share should be the ability to swim along the lines of magnetic fields, including the Earth's field.

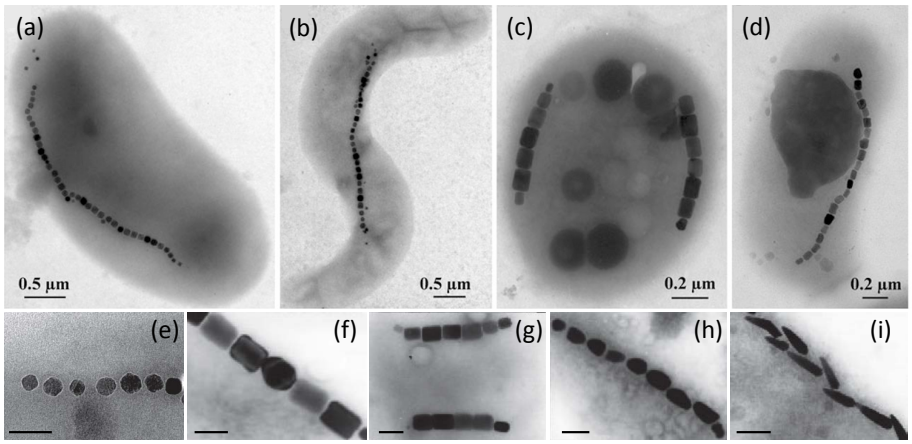

FIGURE 1.2: TEM images of magnetotactic bacteria and magnetosomes. Top) Diversity of bacterial shape: (a) curved; (b) spirillum; (c) coccoided and (d) rod. Bottom) Crystal morphologies and intracellular arrangement of magnetosomes: (e) cubooctahedral; (f,g) elongated prismatic; (h) tooth-shaped and (i) bullet-shaped. Scale bars, 100 nm. Adapted from Bazylinski et al.[3] (a-d) and from Uebe and coworkers[17] (e-i)

The characteristics of the magnetosomes differ among the different types of magnetotactic bacteria but are consistent within a single species. This fact clearly reflects

that the formation of these biogenic nanoparticles is under strict biological control. The morphologies of the crystals fit to three main patterns see Fig. 1.2(bottom): cuboctahedral (e), elongated prismatic (f,g) and bullet- or tooth-shaped (h,i). The size of the magnetic crystals also varies among species ranging from around 35 to 120 nm. Nevertheless, each species synthesizes magnetosomes with a characteristic size and a narrow size distribution. Interestingly, the diameter range of the magnetosomes always remains within the range of variation of the stable single-magnetic domain particles thermally stable at physiological temperature[1,3,18,19].

Two different phases could be differentiated in the magnetosome: the mineral core and the organic envelope. The mineral core presents high chemical purity, being magnetite, Fe_3O_4, in most of the species but some of them synthesize greigite, Fe_3S_4. The magnetic core is surrounded by a proteinaceous lipid membrane that controls the biomineralization process [15,20,21]. The magnetosome membrane is originated by invagination of the cytoplasmic membrane and can be observed within the cell, as empty vesicles, before the formation of the mineral phase [21,22]. As could be expected, the lipid composition of the magnetosome membrane is similar to that of the cytoplasmic membrane. However the inserted proteins are special functional proteins involved the synthesis of the magnetic core.[23].

The magnetosomes are mainly arranged in one or more chains positioned in the long axis of the cell. Each chain, of variable length, may contain 10-20 magnetosomes. In this arrangement the magnetic moments of the individual magnetosomes sum up and turn the cell into a single magnetic dipole that functions as a magnetic needle enabling the bacteria to passively align in magnetic fields[18,24]. The formation of the chain is guided by specific cytoskeletal elements, which also anchor the chain in a correct position within the cell [22,25].

The underlying biological control is the reason why the size, shape, chemical composition and intracellular arrangement of magnetosomes varies among species but remains nearly invariant in each one.

Despite their ubiquity and abundance in the environment, MTB are fastidious microorganisms, difficult to grow and maintain in the laboratory[13]. At present, only a few representatives have been isolated in axenic culture and deposited in bioresource centers. This explains why much of the knowledge rests on the two first species isolated and easy-cultured, *Magnetospirillum magneticum* AMB-1 and *Magnetospirillum gryphiswaldense* MSR-1. They were isolated from freshwater sediment in the early 1990s [26,27]. Both strains are spirilla and biomineralize cubooctahedral magnetite crystals arranged in a single chain. Along the present thesis we have worked with *Magnetospirillum gryphiswaldense*, strain MSR-1.

1.2 *Magnetospirillum gryphiswaldense* MSR-1

As introduced in previous section, the morphology and size of the magnetosomes are specific of each bacteria species. In particular, *Magnetospirillum gryphiswaldense* synthesize cubo-octahedral magnetite nanoparticles with an average diameter of $\approx$ 45 nm and a narrow size distribution of $\approx$ 8 nm. Transmission electron microscopy (TEM) and cryo-tomography techniques reveal that the magnetosome presents faceted morphology where the [111] axes define the growth directions of the hexagonal faces of the truncated cuboctahedrons. Bacteria organize the magnetosomes forming a chain where the hexagonal faces are disposed face to face being the total magnetic moment oriented along the chain axis ([111] axes). In this configuration the magnetosome chain behaves as a compass needle and under the action of an external magnetic field, the magnetic torque reorients the bacteria towards the field direction. Fig. 1.3 displays TEM and cryoelectron tomography images of *M. gryphiswaldense* and the synthesized magnetosomes.

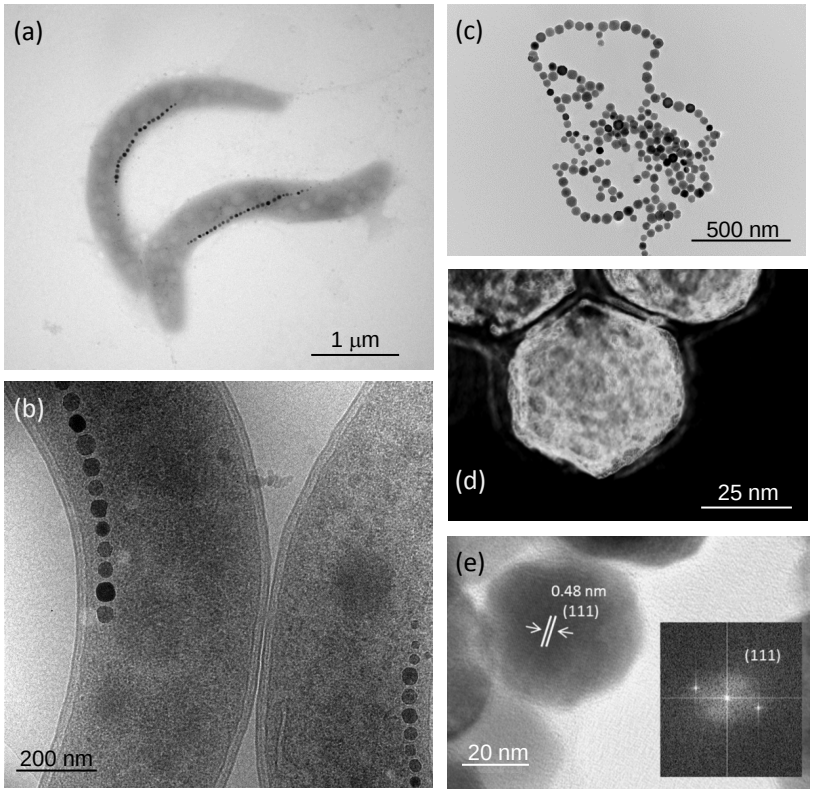

FIGURE 1.3: Electron micrographs of cells and magnetosomes of *Magnetospirillum gryphiswaldense*. (a) TEM image of bacteria with the chain of magnetosomes along the long axis and one flagellum in each pole; (b) Cryoelectron tomographic slide showing a chain of magnetosomes lined up the long axis of the cell; (c) TEM image of isolated and purified cubooctahedral magnetosomes; (d) cryoelectron tomography of isolated magnetosomes; (e) HRTEM and Fourier trasform of isolated magnetosome.

Electron micro-diffraction on a single magnetosome confirms that they are sin-

gle magnetite crystals, Fe_3O_4. Fig. 1.3e shows the electron diffraction pattern of a [111] zone axis of magnetite. The magnetic response of the cells also corresponds to pure magnetite, as confirmed by the evolution of the magnetization as a function of temperature, M(T), measured at 5 mT (see Fig.1.4), which shows a sharp feature at 107 K that is due to the Verwey transition, a well-known characteristic of pure magnetite. It should be noted that although this Verwey transition occurs at 120 K in bulk magnetite, lower values (between 102 and 117 K) are found in magnetosomes[28], a shift attributed to nanoscale effects. The presence of this sharp transition temperature is a clear indication of the high quality in terms of stoichiometry of the biogenic magnetite crystals obtained from the biomineralization process.

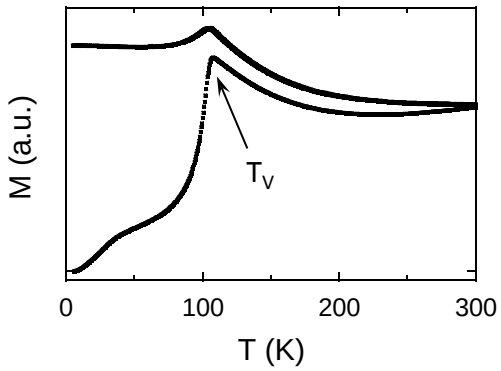

FIGURE 1.4: M(T) curve of *M. grysphiswaldense* measured at 5 mT. The sharp transition observed at 107 K is the Verwey transition.

1.3 Magnetite structure

Magnetite, Fe_3O_4, presents a spinel structure, a complex structure composed by eight formula units, or a total of 8×7=56 ions, per unit cell. The large oxygen ions (radius $\sim$0.14 nm) are packed close together in a face-centered cubic arrangement, and the smaller metal ions (radius $\sim$ 0.08 nm) occupy the spaces between them (see Fig. 1.5). These spaces are of two kinds. One is called a tetrahedral (Th), because it is located at the center of a tetrahedron whose corners are occupied by oxygen ions (Fig. 1.5b). The other is called an octahedral site (Oh), because the oxygen ions around it occupy the corners of an octahedron (Fig. 1.5c). The crystallographic environments of the tetrahedral and octahedral sites are therefore distinctly different[29,30].

However, not all of the available sites are actually occupied by metal ions. Only one-eighth of the Th sites and one-half of the Oh sites are occupied. In magnetite, the Fe cation distribution is as follows: 8 Fe^{2+} in octahedral sites (Fe_{Oh}), 8 Fe^{3+} in tetrahedral (Fe_{Th}) sites, and 8 Fe^{3+} in octahedral (Fe_{Oh}) ones.

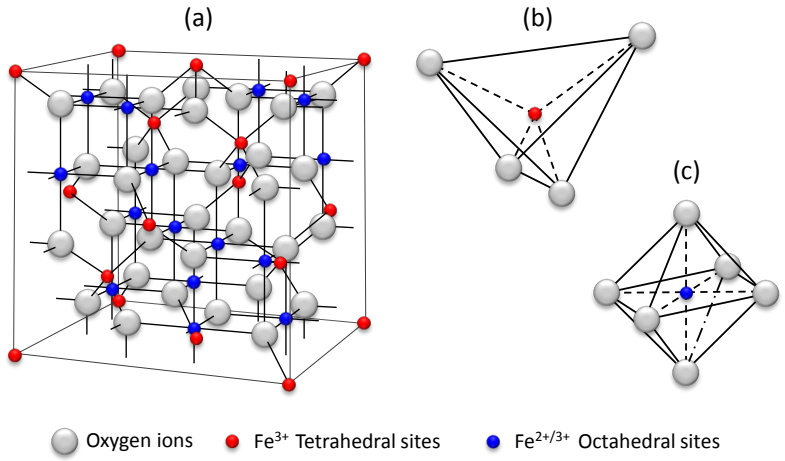

FIGURE 1.5: Crystal structure of magnetite.

1.4 Applications

The outstanding properties of magnetosomes make them ideal candidates for a number of technological applications (see Fig. 1.6). On top of their uniform size and shape, chemical purity, and easy reproducibility, they display a high magnetic moment thermally stable at room temperature and, very importantly, they are surrounded by a lipid-protein membrane, which confers them stability avoiding aggregation of extracted magnetosomes, easy functionalizability and biocompatibility.

Here we will review some of the potential applications of magnetosomes and MTB, with special focus on biomedical applications, and will discuss the main drawbacks that are delaying the transfer of the magnetosome-based technology to the market.

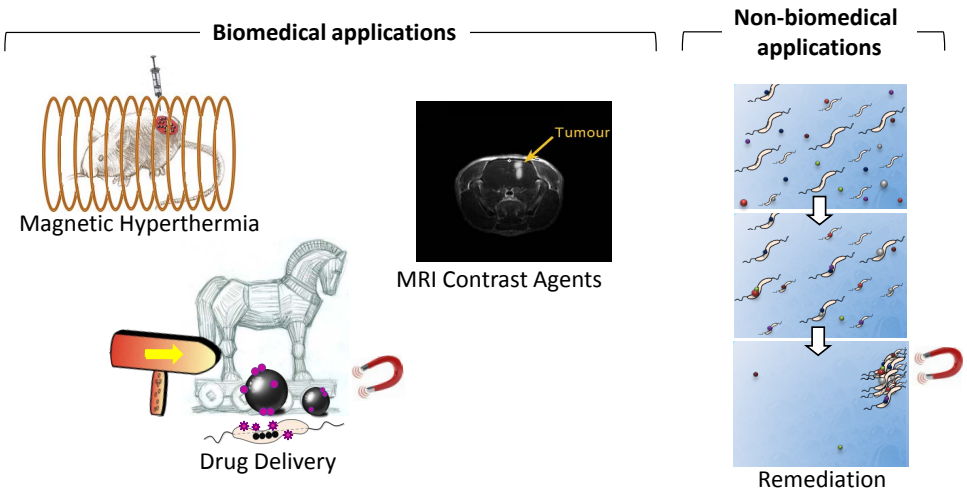

FIGURE 1.6: Applications diagram.

Magnetic hyperthermia

Magnetic hyperthermia is a therapy that aims at debilitating cancer cells by delivering heat to them. In magnetic hyperthermia the magnetic nanoparticles are attached to or internalized into the tumor cells and an alternating magnetic field (AMF) is applied. Under the action of the AMF, the magnetic moment of the nanoparticles describes a hysteresis loop, whose area is proportional to the dissipated energy that increases the temperature of the tumor. By reaching temperatures around 40 - 45 °C in the tumor area, the cancer cells can be 'deactivated' (dead or driven to apoptosis) without affecting the healthy ones. The study of magnetic nanoparticles with high heating capability, namely large hysteresis loop area for a given magnetic field intensity H and frequency f, has generated wide interest. In this context, magnetosomes from *M. gryphiswaldense*[31–34] and *M. magnetotacticum*[34,35] have been proven to exhibit large specific absorption rate (SAR) values at AMFs within the clinical limits ($H \cdot f \leq 5 \times 10^9$ $Am^{-1}s^{-1}$)[36], constituting ideal candidates for magnetic hyperthermia. The SAR values observed for magnetosomes are considerably higher than those for chemically synthesized magnetite nanoparticles[37–39]. This is mainly attributed to the magnetosomes being single magnetic domains stable at room temperature, a condition met by magnetosomes due to their size (between 30-50 nm for *M. gryphiswaldense* and *M. magnetotacticum*), sizes that otherwise are hardly achievable with synthetic procedures.

Targeted drug delivery

The magnetosome membrane provides a matrix for the functionalization of the magnetosomes with biomolecules of interest and is a unique characteristic of magnetosomes over synthetic magnetic nanoparticles. Functionalization is possible either by chemical modification of the isolated particles or by genetic engineering of magnetosome membrane proteins. Genetic approaches involve fusing magnetosome membrane proteins to other enzymes or proteins of interest[40]. Functionalization opens up a wide range of applications in which magnetosomes bind specifically to cells, proteins, or nucleic acids of interest that are subsequently separated, detected or guided with magnetic fields[4]. For example, Ginet et al.[41] engineered a nanobiocatalyst to degrade ethyl-paraoxon, a commonly used pesticide, by genetically functionalizing the membrane surrounding the magnetite particles of *M. magneticum* with a phosphohydrolase and subsequently sequestering (and reusing) the particles with a magnet. Magnetosomes functionalized with anti-tumour drugs have been proposed as potential carriers for targeted cancer therapies. *In vitro* studies demonstrate the suitability of anti-cancer drug-loaded magnetosomes from *M. gryphiswaldense*[42] and *M. magneticum*[43] as drug carriers, but it is still to be proven the magnetic guiding capability and controlled drug release.

In this sense, instead of the isolated magnetosomes, the whole MTB have been proposed as potential biorobots with the ability to target and destroy cancer cells.

Since MTB incorporate the magnetosome chain, they can be externally detected, manipulated, and guided. In addition, MTB naturally migrate towards their preferred oxygen concentration region, which is close to, or below, the oxic-anoxic transition zone. This faculty is very appropriate for cancer treatment because since the tumor area is low in oxygen due to the tumor tendency to rapidly outgrow its blood supply, MTB are inherently attracted towards these hypoxic regions of the tumor. Therefore, targeting the tumor area with live MTB could become easier and more efficient than with nanoparticles. Preliminary works in this field have shown that *M. magneticum* can navigate in capillaries and target multicellular tumors[44], and that *Magnetococcus marinus* carrying drug-containing nanoliposomes can be magnetically guided towards hypoxic regions of colorectal xenografts[45], with 55% of the injected cells penetrating into the hypoxic regions of the tumour.

Magnetic resonance imaging (MRI)

The potential of magnetosomes as diagnosis tools has been also demonstrated recently. It is well known that superparamagnetic iron oxide nanoparticles (SPION) can be used as magnetic resonance imaging (MRI) contrast agents as they shorten the T_2 relaxation time. Recently, Mériaux et al.[46] have demonstrated that magnetosomes show an improved MRI contrasting perfomance as compared to commercially available SPIONs, attributed to the particles being monodomain and magnetically stable at room temperature. Indeed, *in vitro* relaxometry measurements showed that magnetosomes of *M. magneticum* AMB-1 and *Magnetovibrio blakemorei* MV-1 display a transverse relaxivity r_2 between three and four times higher than commercial SPIONs that leads to a significant gain in MRI sensitivity. The improved MRI contrasting potential of MV-1 magnetosomes with respect to commercial SPIONs was demonstrated in *in vivo* tests aimed at visualizing mouse brain angiograms after systemic injection. These experiments did also prove that a lower dose of iron was needed when using magnetosomes as contrast agents instead of commercial SPIONs. As a step forward, magnetosomes have been proposed as probes for molecular imaging. Molecular imaging is a technique that combines MRI imaging with cell tracking and/or molecular targeting via the functionalization of the magnetosome membrane. A proper functionalization allows not only detecting with MRI where a tumour is located in the body, but also the activity and expression of specific molecules. The feasibility of using magnetosomes as molecular imaging probes to target breast cancer cells[47] and brain tumor in a mouse model of human glioblastoma[48] have been recently demonstrated. In the latter work magnetosomes of *M. magneticum* AMB-1 were genetically modified so that their outer surface expressed the RGD peptide, whose binding efficiency to $\alpha_v\beta_3$ integrin receptors overexpressed by tumor cells has been largely demonstrated. *In vivo* MRI at 11.2 T revealed the enhanced retention time of the RGD-labelled magnetosomes within the tumor compared to the unlabelled magnetosomes. The combined activity of magnetosomes

as diagnosis and therapeutic agents (as molecular imaging probes and drug carriers/hyperthermia agents) has also been proposed[31].

Given the potential of magnetosomes in biomedical applications, their biocompatibility must be addressed before they can be of clinical use, although a good compatibility is expected due to the natural membrane surrounding the magnetic cores, as preliminary *in vitro* and *in vivo* studies suggest[34,49–52].

Although being magnetosomes the result of a genetically controlled biomineralization process assures their reproducibility and outstanding properties, the feasibility of tuning their magnetic properties could expand their potential applications. In this sense, exposure of MTB to transition metal elements (Co, Mn, and Cu) has been shown to change the magnetic properties of magnetosomes[53–55]. In particular, Co doping of magnetosomes from *M. magneticum* increases the magnetic coercivity[55], which could improve the heating power of these magnetosomes for hyperthermia applications. Doping of magnetosomes is generally achieved upon addition of the doping element to the growth medium, but other routes involving genetic modifications have been explored based on the expression of a metallophore specific for Co and/or Ni in magnetospirilla[56].

Remediation

Other biotechnological potential applications involve the use of MTB as biosorbents for trace radionuclides and heavy metals in environmental bioremediation[57]. MTB are being investigated in this field because unlike other microorganisms usable for bioremediation, MTB allow recovering the metal from the medium by subsequently trapping the MTB with a magnet[58].

Other nanotechological applications

There are additional nanotechnological applications of magnetosomes not necessarily related to biotechnology. Owing to their uniform shape and size, magnetosomes can be self-assembled forming regularly ordered 2D superstructures[59] with potential applications as miniaturized information storage materials or biosensors. Magnetite nanoparticles can be fabricated by a biomimetic approach, that is, mimicking the MTB biomineralization process *in vitro*, by using one of the biomineralization proteins that control the formation of the magnetite crystals within the MTB cell (in particular *M. magneticum* AMB-1), namely the *Mms6* protein[60]. In this way a novel strategy for the production of magnetic arrays has been reported that involves the fabrication of biotemplates of the *Mms6* protein with interferometric lithographic patterning, resulting in arrays of uniform magnetite nanoparticles (86 $\pm$ 21 nm) with a period of 357 nm[61]. Finally, magnetosome chains form natural 1D magnetic nanostructures that have inspired the fabrication of highly anisotropic

structures for magnetic field detection in electronic devices, biosensing or biometric techniques[62].

Drawbacks

Although the advantages of magnetosomes and MTB as potential (bio)technological agents are largely demonstrated, the commercial exploitation has not yet been achieved, primarily because MTB are slow and difficult to culture outside their natural environment, and also because of the fastidious process needed to extract magnetosomes from the bacteria. Despite advances in scaling up the bacterial production in large bioreactors for *M. gryphiswaldense*[63] and *Magnetovibrio blakemorei*[64], an alternative strategy to overcome this problem comes from instigating the magnetosome biogenesis in alternative microbes easier to grow in the laboratory. In this sense, gene clusters of *M. gryphiswaldense* have recently been transferred into the photosynthetic bacterium *Rhodospirillum rubrum*, a microorganism with 90% genetic similarity with *M. gryphiswaldense*, and magnetosome biogenesis with a formation of well-ordered magnetosome chains has been achieved[65]. Magnetosomes bisoynthesized by *R. rubrum* are however slightly smaller than those of *M. gryphiswaldense* and so does the mass of magnetite per cell. A crucial next step will be to instigate magnetosome biosynthesis in *Escherichia coli*, which is the most widely used and characterized model bacterium and onto which the entire microbiological and biotechnology industries are based[66].

1.5 Motivation and Thesis structure

The employment either of magnetosomes or magnetotactic bacteria in the different applications presented above requires a deep understanding of their properties and features. This is where the present Thesis comes from. This work is devoted to the magnetic and structural characterization of these fascinating magnetic systems. With this aim, the Thesis is divided in three main blocks.

First, we address the magnetic configuration of magnetosome chains. The potential use of MTB as biorobots in cancer treatment make the comprehension of the chain configuration an issue of paramount importance. Magnetosome chains constitute a natural paradigm of 1D magnetic nanostructures. Electron cryo-tomography evidence that rather than the *a priori* expected straight lines, magnetosomes chains present an helical shaped structure. Chapter 2 address the relationship between the chain structure and the magnetic response of magnetosomes. By means of magnetic and structural characterization this Chapter proposes a mechanism of chain formation arising from the competition between the dipolar interaction of magnetosomes within the chain and the lipid/protein based mechanism, induced by the forces exerted on each particle by the cytoskeleton.

After that, we face the biomineralization process. This complex biochemical process genetically controlled gives rise to magnetosomes with a characteristic crystalline and chemical purity. A deep insight into the biomineralization process could lead to advances in the development of bioinspired routes for the synthesis of large amount of high quality magnetic nanoparticles. So far, research efforts have been focused in genetic and proteomic studies while there is little research on the mineral evolution preceding the full-sized magnetite magnetosomes. Chapter 3 is devoted to analyze the phase evolution from the early stages of the process until the presence of well-formed magnetosome chains. With this aim, we perform a time-resolved structural study of the biomineralization process. This Chapter evidences the coexistence of two phases: bacterioferritin, mostly observed at the early stages of the process, and magnetite, more abundant as the process evolve.

Finally, the third block addresses the doping of magnetosomes. The substitution of iron cations by transition metal dopants in magnetite is a proven method to change the magnetic properties of the magnetic nanoparticles. Namely, the incorporation of Co within the structure of magnetite increase the coercivity and hence the hysteresis losses and the specific absorption rate (SAR) of the nanoparticles, which is directly related with the efficiency of nanoparticles in hyperthermia treatment. In this sense, the doping of magnetosomes results in the overcoming of the natural limitations imposed by the genetic control of the synthesis and the expanding of the range of applications. Chapter 4 investigates the incorporation of Mn, Co, Ni, Cu and Zn by adding these elements into the growth medium. While no evidence of Ni, Cu and Zn-doping was found, small amount of Mn and Co substitute the magnetite structure. The presence of these elements strongly modify the magnetic properties of magnetosomes. A deeper insight of the role of Co in the magnetic properties of Co-doped magnetosome chains is addressed. Modeling of hysteresis loops with a modified Stoner-Wohlfarth approach sheds light on the different anisotropy contributions and their dependence on temperature for control magnetosomes and Co-doped magnetosome chains.

Chapter 2

On the chain configuration: a magnetic and structural study

2.1 Introduction

Magnetosome chains constitute a natural paradigm of 1D magnetic nanostructures. Since magnetosomes are single magnetic domains, the chain behaves as a large single permanent dipole magnet which is able to passively reorient the whole bacteria along external magnetic field lines, even at fields as small as those existing near the Earth's surface ($\approx$ 20-60 μT)[1,13,17].

Due to their large magnetic anisotropy, 1D magnetic nanostructures show high potentiality in biomedical applications[38,45,67,68], in actuation devices as nanorobots[69], in nanosensor devices[62], and in magnetic memory devices[70].

The present Chapter is devoted to shed light on the assembling of magnetosomes in chains. In particular, here we address the underlying mechanisms that determine the arrangement of the magnetosomes and consequently the geometry of the chain.

As shown by cryotomography imaging on *Magnetospirilla*, bundles of cytoskeletal filaments intervene in the chain assembly[22,25,71]. These filaments, formed by the actin-like protein MamK, traverse the cell and position the chain in the middle of the cell. Another important protein involved in the chain formation is MamJ. One possible function of MamJ is to connect the magnetosome membrane to the cytoskeletal filament. As magnetosomes get closer together, magnetic dipolar interactions arise. The dipolar interactions depend on the direction of the net magnetic moment of the nanoparticle, determined by the magnetic anisotropy.

Here we show by electron cryotomography imaging that magnetosome chains of *M. gryphiswaldense* are not straight lines but appear slightly bent, a fact that has been also observed in previous works[2,71]. The implications of the chain shape on the magnetic response of magnetosome chains have then been addressed with complementary techniques performed on a set of bacterial arrangements: i) small angle neutron/x-ray scattering (SANS/SAXS) on a bacterial colloid, ii) macroscopic mag-

netometry on 3D and 2D fixed arrangements of randomly distributed and aligned bacteria, and iii) x-ray photoemission electron microscopy (XPEEM) on an individual chain of magnetosomes extracted from bacteria.

Two main findings are achieved from this Chapter. Firstly, the equilibrium magnetic moment of the magnetosomes is tilted 20° out of the [111] crystallographic axis of magnetite, that is parallel to the chain axis, as concluded from the magnetic analysis. Secondly, the tilting of the magnetic moment is the key to understand the helical-like shape of the magnetosome chains. Indeed, the experimental chain patterns imaged by electron cryotomography are accurately reproduced by counterbalancing the magnetic dipolar interactions between magnetosomes, strongly affected by the orientation of the individual magnetic moments, and a lipid/protein-based mechanism, modeled as an elastic recovery force exerted on magnetosomes.

Besides the basic interest of this study, a precise knowledge of the mechanisms determining the chain shape is decisive in applications of MTB such as biological micro-robots. Precisely, recent works propose MTB to be exploited as motors with embedded source propulsion secured by their flagella and embedded steering system to control the directional motion provided by their magnetosome chain[45].

2.2 Growth conditions and magnetosome isolation

For the present study we have employed *Magnetospirillum gryphiswaldense* bacteria in the last stages of their biomineralization process, i.e. when well-formed magnetosomes are observed.

M. gryphiswaldense MSR-1 (DMSZ 6631) was grown in three-fourths 1L-bottles loosely capped at 28 °C without shaking in an iron rich medium[63]. A magnetic inoculum, with cells at early stationary phase was employed. After 96 h-incubation, when bacteria present well-formed magnetosomes chains, cells were fixed with 2% glutaraldehyde, harvested by centrifugation, washed three times and finally concentrated up to $10^9 - 10^{11}$ cell/mL in ultrapure water.

Magnetosomes were isolated according to the protocol described by Grünberg et al.[72] with minor modifications. Cells were collected by centrifugation, suspended in 20 mM HEPES-4 mM EDTA (pH=7.4), and disrupted using a French press (1.4 kbar). Then, the magnetosomes were collected from the supernatant by magnetic separation and rinsed 10 times with 10 mM Hepes-200 mM NaCl (pH=7.4). Finally, the isolated magnetosomes were suspended in ultrapure water reaching a concentration of 20 μg/mL.

2.3 Electron cryotomography imaging (ECT) of the magnetosome chain

Cells of *M. gryphiswaldense* have been imaged by electron cryotomography (ECT). Imaging was carried out at Biogune in collaboration with Dr. David Gil. Details of sample preparation are specified in *Materials and Methods* section (page 44).

Since bacteria are cryoembedded, the cells and as a consequence the magnetosome chains inside them preserve their natural shape, avoiding artifacts associated to cell drying processes. ECT images of three cells are shown in Figs. 2.1a,b,c. The upper part of Fig. 2.1a,b,c shows the reconstructed 3D tomograms from the tilt-series of images obtained by ECT of the three cells and the insets show the Z-projected images of the tomograms. These projections are equivalent to the images obtained by transmission electron microscopy. The chains shown in Fig. 2.1 are composed of $N = 15$, 22 and 20 magnetosomes, respectively, and the mean distance between magnetosomes is $d \approx 60\,\text{nm}$. ECT imaging evidences that magnetosome chains are certainly not straight lines but exhibit more complex 3D patterns. Three slices (XY, YZ and XZ) of each of the 3D reconstructions are shown below the tomograms. The three slices are cuts of the corresponding tomograms taken along the marked lines and intersect in one of the magnetosomes, so that the XYZ coordinates of that particular magnetosome can be determined. By determining the XYZ coordinates of all the magnetosomes in the chain we have been able to reconstruct the three magnetosome chains shown at the bottom of the figure, where a zoom-in of one of the magnetosome chain reconstructions emphasizes the deviation from a straight line.

In order to further investigate the morphology of each single particle, a similar analysis was carried out in magnetosome extracted from *M. gryphiswaldense*. Fig. 2.2a displays a reconstructed 3D tomogram, and Fig. 2.2b presents the XY, YZ and XZ central sections of the tomogram. These images evidence that magnetosomes have a strongly faceted morphology similar to the truncated octahedral one, which is adopted as a reference (Fig. 2.2c), with a mean size of 40 nm. In this truncated octahedron the $\langle 001 \rangle$ crystallographic axes define the growth directions of the square faces and the $\langle 111 \rangle$ those of the hexagonal faces. The magnetosome in the image has two neighbours (only partially observed in the image). The three magnetosomes have self-assembled so that their hexagonal faces are towards each other. In the same way, when magnetosomes are forming the chain inside the cell, numerous studies in *Magnetospirilla* show that they align with their hexagonal faces towards each other[73,74], i.e., along one of their $\langle 111 \rangle$ crystallographic directions. The [111] direction along which magnetosomes align defines the so-called *chain axis* (see Fig. 2.1c).

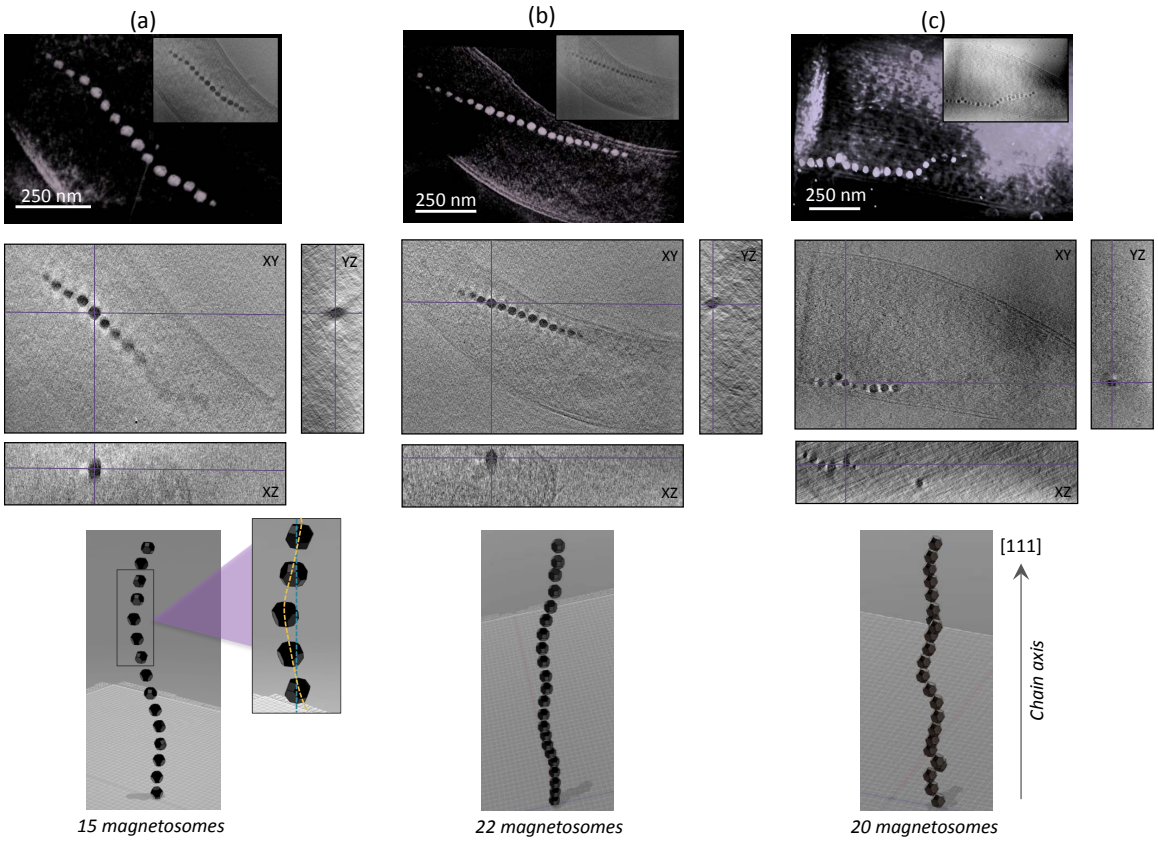

FIGURE 2.1: Electron cryotomography (ECT) of magnetosome chains. (a), (b) and (c) are ECT images of three different bacteria. Top: 3D tomograms reconstructed from the tilt-series of images obtained by ECT. The insets show the Z-projection of the tomograms. Center: XY, YZ and XZ slices of the tomograms shown on top. The three slices are taken along the marked lines and cross on one of the magnetosomes. Bottom: Experimental reconstruction of magnetosome chain. A zoom-in of the magnetosome chain reconstruction highlights the deviation from a straight line.

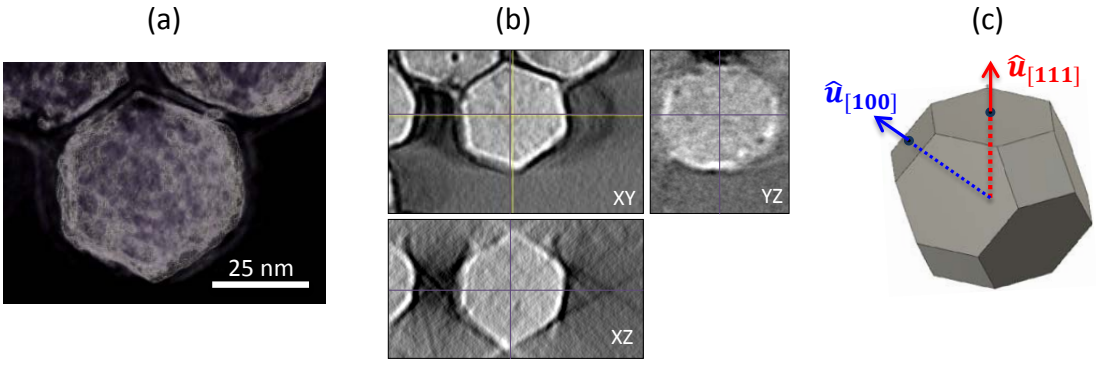

FIGURE 2.2: ECT images of extracted magnetosomes. (a) Reconstructed tomograms. (b) Central XY, YZ and XZ slices of the magnetosome tomogram shown on (a). (c) Schematic representation of a cuboctahedral magnetosome. Blue and red arrows represent the [001] and [111] crystallographic axes, respectively.

2.4 Magnetism of magnetosome chains

ECT images of the magnetosome chain show a complex structure and an evident deviation from a straight linear configuration. This must have an effect on the magnetic behaviour of the chain. We have analyzed the magnetic properties of magnetosome chains from *M. gryphiswaldense* by complementary magnetic techniques in three different arrangements: i) a colloidal dispersion of bacteria, this means that we have a 3D distribution of bacterial chains, studied by magnetization and small angle neutron/x-ray scattering (SANS/SAXS); ii) macroscopic magnetization measurements on bacteria forming 3D and 2D distributions; iii) x-ray photoemission electron microscopy (XPEEM) on individual chains of magnetosomes extracted from the bacteria forming a 1D magnetosome arrangement.

2.4.1 Magnetization of a bacterial colloid

The magnetization curve of a highly concentrated bacterial colloid ($6 \cdot 10^{11}$ cell/mL) suspended in ultrapure water was measured on a vibrating sample magnetometer up to an applied field of 1 T, leaving two minutes between each measurement to assure thermal equilibrium was achieved at each point.

Fig. 2.3a shows the obtained magnetization curve $M(H)$ in logarithmic scale. The magnetization increases rapidly with the applied field until it reaches a plateau between $3\,\mathrm{mT} \leq \mu_0 H \leq 15\,\mathrm{mT}$ at a value that is 90% of the saturation value ($M = 0.90 M_s$). Then, the magnetization increases again slowly up to saturation. This behavior opens up two possible scenarios: i) an initial chain alignment ($\sim 3\,\mathrm{mT}$) followed by a coherent rotation of the magnetosome moments at higher magnetic fields (see Fig. 2.3b) or ii) the misalignment of chains with respect to the applied magnetic field below 15 mT (2.3c), as will be discussed in the following.

2.4.2 Small angle neutron/x-ray scattering (SANS/ SAXS) on a bacterial colloid

The magnetic properties of the bacterial colloid have been further investigated via small angle X-ray scattering (SAXS) and polarized small angle neutron scattering (SANS). In a SAXS/SANS experiment the x-ray/neutron beam ($\vec{k}_{IN}$) hits the colloidal sample and the scattered beam ($\vec{k}_{scat}$) impacts on a 2D detector perpendicular to the incoming beam (Fig. 2.17 in *Materials and Methods* section).

The SAXS data were at collected in a Xenocs Nano-InXider at ISIS (Rutherford Appleton Laboratory, Didcot, UK). The colloidal dispersion was filled into a quartz glass capillary and was measured in absence of an externally applied magnetic field (see 2.17a). Measurements conditions are detailed in page 45 in the *Materials and Methods* section. Via SAXS exclusively the nuclear scattering intensity $I(\vec{q}) \propto |\tilde{N}|^2$ is determined, with $\vec{q}$ being the scattering wave vector and $\tilde{N}(\vec{q})$ being the Fourier

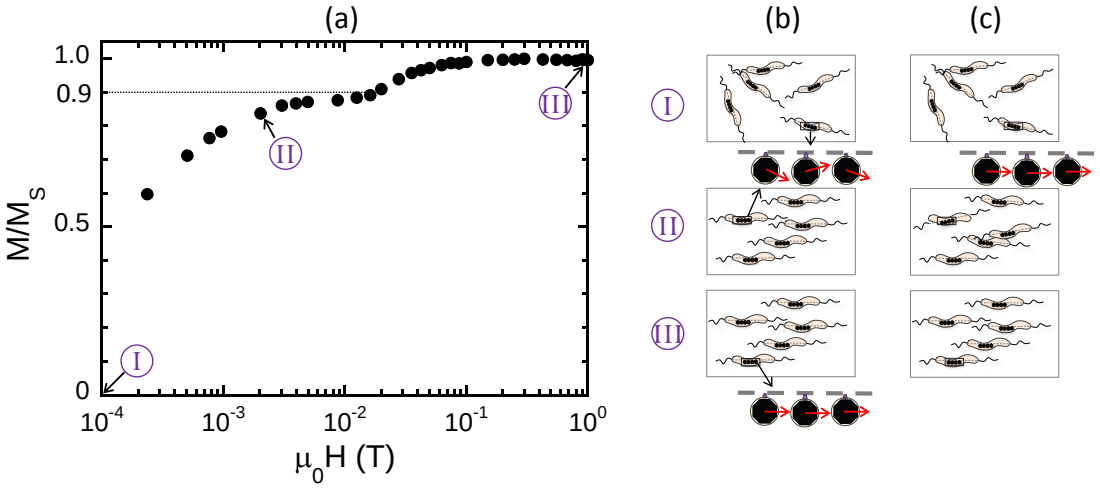

FIGURE 2.3: (a) Magnetization curve of the colloidal dispersion of bacteria. The field axis is in logarithmic scale to magnify the low-field region. The experimental data marked with arrows correspond to the points measured by SANS/SAXS ($\mu_0 H = 0\,\text{mT}; 2\,\text{mT}$; and $1\,\text{T}$). The sketches display the two-step magnetization process proposed, either (b) due to the misalignment of the magnetization with the chain axis or (c) owing to the angular dispersion of cells in the colloid.

transform of the nuclear scattering length density $\rho(\vec{r})$.

To analyze the data we performed an indirect Fourier transform[75] of the radially averaged 1D intensity $I(q)$ to extract the pair distance distribution function $P(r)$. The real space function $P(r)$ provides direct information about the distances between scatterers from the scattering sample[76] and hence contains information about the average particle geometry as well as correlations between neighboring particles. For the indirect Fourier transform we used an approach based on Vestergaard et al. [77] and computational details can be found on Bender et al.[78].

Fig. 2.4a shows the radially averaged 1D SAXS intensity $I(q)$ of the colloidal dispersion measured in zero field. An indirect Fourier transform of $I(q)$ results in the pair distance distribution function $P(r)$ displayed in Fig. 2.4b. The extracted distribution function exhibits three distinct peaks. The first peak has its maximum at about 25 nm and is nearly bell-shaped. The comparison of this peak with the pair distance distribution function of a homogeneous sphere with diameter D_{SAS}=48 nm shows qualitatively very good agreement. Hence, we surmise that the first peak corresponds to the nuclear scattering of the individual magnetosome of an average size of about 48 nm. This particle size is considerably larger than the one obtained by ECT ($\approx$ 40 nm). The reason for this difference is that ECT is only sensitive to the core of the magnetosome (the magnetic nanoparticle), while the small angle scattering (SAS) techniques are sensitive to both the core and the surrounding lipid bilayer membrane. In fact, for neutrons, the scattering cross section of H is very large, which means that organic materials with many H-atoms (such as the lipid membrane in our

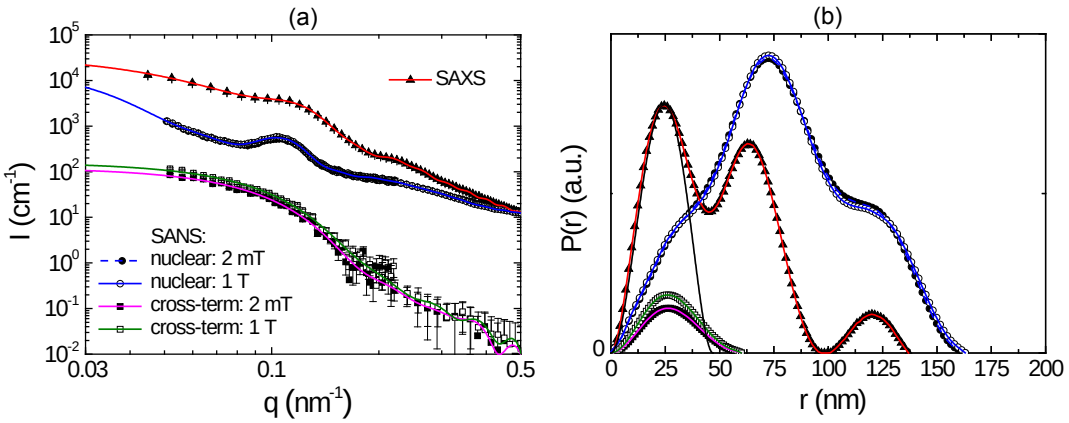

FIGURE 2.4: (a) 1D scattering intensities measured by SAXS in zero field (radial average, offset by scale factor 100) and the field dependent nuclear scattering intensities $I_{nuc}(q)$ (offset by scale factor 10) as well as the cross-terms $I_{cross}(q)$ determined by polarized SANS. The lines are the corresponding fits by an indirect Fourier transform. (b) Pair distance distribution functions $P(r)$ obtained from the indirect Fourier transform of the 1D scattering intensities shown in (a). The black line is the $P(r)$ of a homogeneous sphere with diameter D_{SAS}=48 nm. The distribution function determined by SAXS is offset by arbitrary scaling factors.

case) can generate large scattering signals[79]. Considering a membrane thickness of $\approx$ 4 nm, the core diameter obtained by SAXS is 48-8=40 nm, in agreement with the value obtained from ECT. The maxima of the second and third peak of the distribution function are at about 75 and 125 nm, and both peaks are also nearly bell-shaped. The positions of the peaks agree well with the expected positions of the center of mass of the next neighbors in a chain-like structure of D_{SAS}=48 nm sized particles with a center-to-center distance of d_{SAS} $\approx$50 nm, close to the $d \approx 60$ nm distance measured by ECT.

On the other hand, SANS instrument D33 at the Institut Laue Langevin (ILL, Grenoble, France)[80,81] was employed in order to get a longitudinal neutron-spin analysis (POLARIS)[82] (see details on page 45 in *Materials and Methods* section). A homogeneous magnetic field $\vec{H}$ was applied perpendicular to the neutron beam ($\vec{H} \perp \vec{k}$) with field amplitudes of $\mu_0 H = 2\,\mathrm{mT}$ and 1 T (see Fig. 2.17b).

The application of the POLARIS mode enabled us to detect the non spin flip (nsf) intensities $I^{++}(\vec{q})$, $I^{--}(\vec{q})$, where the superscripts indicate the polarization of the incoming neutron beam and the scattered neutrons with regard to the applied field direction, respectively ("+": parallel, "-": antiparallel). Defining x as the direction of the neutron beam and z as the direction of the applied magnetic field at the sample position ($\vec{H} \perp \vec{k}$) the nsf intensities can be written as[82]:

$$
\begin{aligned}
I^{\pm\pm}(\vec{q}) \propto & |\tilde{N}|^2 + b_H^2|\tilde{M}_z|^2\sin^4\Theta \\
& + b_H^2|\tilde{M}_y|^2\sin^2\Theta\cos^2\Theta \\
& - b_H^2(\tilde{M}_y\tilde{M}_z^* + \tilde{M}_z\tilde{M}_y^*)\sin^3\Theta\cos\Theta \\
& \mp b_H(\tilde{N}\tilde{M}_z^* + \tilde{N}^*\tilde{M}_z)\sin^2\Theta \\
& \pm b_H(\tilde{N}\tilde{M}_y^* + \tilde{N}^*\tilde{M}_y)\sin\Theta\cos\Theta.
\end{aligned} \tag{2.1}
$$

Here, Θ is the angle between the scattering vector $\vec{q}$ and the magnetic field $\vec{H}$ and the terms $\tilde{M}_{y,z}(\vec{q})$ represent the Fourier transforms of the magnetization in y, z direction. The superscript $*$ indicates the complex-conjugated quantities and the constant $b_H = 2.7 \cdot 10^{-15}\,\mathrm{m}/\mu_B$, with μ_B being the Bohr magneton[82]. To investigate the alignment of the bacteria in field direction we analyzed the 1D nuclear cross sections $I_{nuc}(q) \propto |\tilde{N}|^2$ and the 1D nuclear magnetic cross-terms $I_{cross}(q) \propto (\tilde{N}\tilde{M}_z^* + \tilde{N}^*\tilde{M}_z)$. The purely nuclear scattering intensities were determined by integration of the nsf intensities in 10° sectors around $\Theta = 0°$ ($\vec{q} \parallel \vec{H}$, Eq. 2.1) and the cross terms $I_{cross}(q)$ by integration of $I^{--}(\vec{q}) - I^{++}(\vec{q})$ in 10° sectors around $\Theta = 90°$ ($\vec{q} \perp \vec{H}$, Eq. 2.1). The difference between the two nsf cross sections yields information on the polarization-dependent nuclear-magnetic terms. This difference allows one to highlight weak magnetic contributions relative to strong nuclear scattering (or vice versa). From the determined cross sections we extracted the underlying pair distance distribution functions in the same manner as for SAXS. In H_2O, there is contrast match of bacteria in the dispersion, such that only the magnetosomes and their arrangement are probed by SANS.

Fig. 2.4a shows the structural 1D SANS intensities $I_{nuc}(q)$ detected for field strengths of $\mu_0 H = 2\,\mathrm{mT}$ and 1 T applied perpendicularly to the neutron beam. Both $I_{nuc}(q)$'s are virtually identical, which means that already at 2 mT the bacteria are fully aligned in the field direction. Consequently an indirect Fourier transform of both nuclear scattering intensities results in superimposed pair distance distribution functions, whose second peak ($r \sim 75\,\mathrm{nm}$) is about twice the height of the first peak (Fig. 2.4b). This verifies that the bacteria align with the chain axis parallel to the field, considering that within the chain each particle is surrounded on average by two neighbors and thus the probability to find a scatterer at this position is two times the probability to find a scatterer within the primary particle (first peak). To investigate if structural alignment equals magnetic saturation the cross-terms $I_{cross}(q)$ were analyzed.

The two cross-terms $I_{cross}(q)$ detected at 2 mT and 1 T display the same functional form (Fig. 2.4a) and accordingly the extracted distribution functions are qualitatively similar (Fig. 2.4b). The observation of only one peak can be explained by the fact that the cross terms depict the correlation between nuclear scattering length density and magnetization $M_z(r)$ along the axis perpendicular to the applied field. In all cases

the shape of the distribution function is comparable to the distribution function of a single sphere with a homogeneous scattering length density. This verifies that the particles are homogeneously magnetized (i.e. $M_z(r) = M_z$) and thus can be regarded as single-domain particles. However, the absolute values of $P(r)$ detected at 2 mT are over the whole r-range systematically reduced by a factor of 0.83 compared to 1 T. Assuming that at $\mu_0 H = 1$ T the system is saturated in field direction (i.e. $M_z = M_s$) this means that at 2 mT the magnetization in field direction amounts to $M_z = 0.83 M_s$ and that the magnetic saturation is achieved by a coherent rotation of the spins within the individual nanoparticles towards the field direction. These two processes (chain alignment followed by a coherent rotation of the magnetosome spins) explain the isothermal magnetization measurement of the colloid shown in Fig. 2.3. In the latter, in agreement with the SANS result, at 2 mT $M_z = 0.83 M_s$, and the coherent rotation of magnetosome spins would start at $\approx$ 15 mT, where $M_z = 0.9 M_s$ corresponds to a misalignment of the magnetic moment with the chain axis of $\theta \approx 25°$, where $M_z = M_s \cos\theta$.

2.4.3 Magnetometry on 2D and 3D bacterial arrangements

Macroscopic hysteresis loops of *M. gryphiswaldense* cells have been measured by SQUID and VSM magnetometry. 2D arrangements of aligned bacteria have been obtained by depositing the cells onto a Si substrate under an applied 'aligning' uniform magnetic field $\vec{H}_{al}$. A TEM image of randomly distributed and aligned *M. gryphiswaldense* cells deposited onto a Si substrate are shown in Fig. 2.5a and b, respectively. Similarly, 3D arrangements of aligned bacteria have been obtained by pouring the cells under $\vec{H}_{al}$ into liquid agar that hardens upon cooling. Details about sample preparation are found in *Materials and Methods* section (pages 46 and 48).

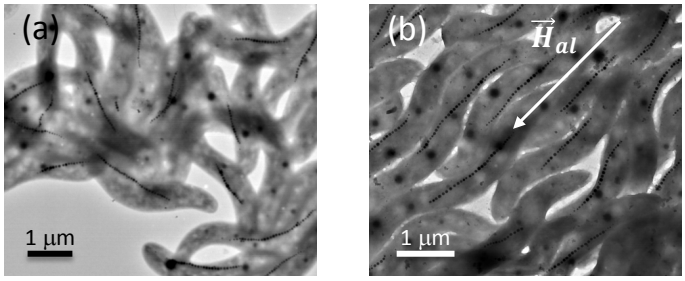

FIGURE 2.5: TEM image of bacteria arranged in a 2D configuration with their chain axes either (a) random or (b)oriented along the aligned magnetic field $\vec{H}_{al}$.

Fig. 2.6a,b shows the hysteresis loops of randomly arranged and oriented bacteria. The hysteresis loops of oriented bacteria have been measured at different angles with respect to $\vec{H}_{al}$ between 0°and 90°in steps of 20 degrees for 3D arrangement and at discrete angles, 0°, 45° and 90°, for 2D arrangement. These measurements evidence that bacteria are highly anisotropic magnetic objects, since their hysteresis

loops depend strongly on the direction of the applied field. This is not surprising, as one would expect that magnetosome chains behaved as a good compass, with a single magnetic easy axis oriented along the chain axis, which, as noted previously, is coincident with one of the magnetosomes ⟨111⟩ crystallographic axes. However, the hysteresis loops of 3D and 2D bacterial arrangements do not correspond to those expected for a uniaxial Stoner-Wohlfarth model[83] along the chain, since the hysteresis loop perpendicular to the chain axis is not anhysteretic as expected. This could be attributed to the misalignment of the magnetic moment already detected by SANS measurements.

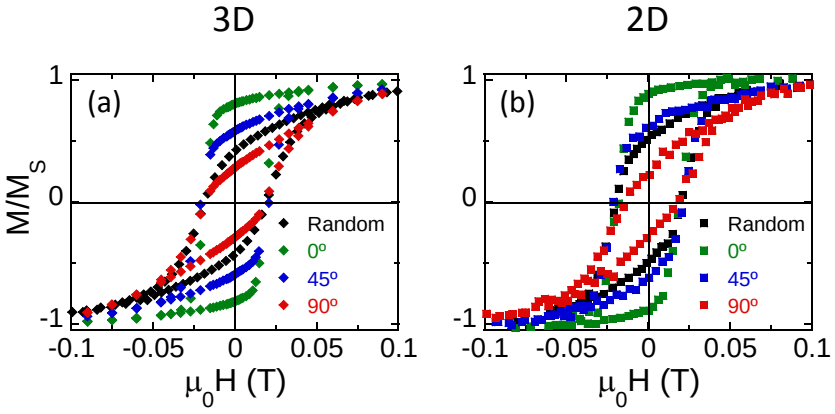

FIGURE 2.6: Hysteresis loops of bacteria in 3D (a) and 2D (b) arrangements forming 0°, 45°, and 90° with the aligning field ($\vec{H}_{al}$), together with the hysteresis loops of randomly arranged bacteria.

More information on the magnetism of magnetosome chains has been gathered from the theoretical modelling of the hysteresis loops.

Magnetosomes along the chain have been managed as a collection of independent single domain particles which are large enough to be thermally stable and so to have the magnetization firmly anchored at the minimum energy states. Therefore the physical problem can be implemented by using single particle approach described by the Stoner-Wohlfarth model. Inter-particle dipolar interactions are assumed to impose an additional anisotropy contribution, equal for all, referred to as 'interaction' anisotropy. The functional form of the energy density for a magnetic single domain depends on the orientation of magnetization given by two variables (polar (θ) and azimuthal (φ) angles in spherical coordinates). Such energy density landscape $E(\theta, \varphi)$, in the presence of arbitrary external magnetic fields contains the magnetic anisotropy terms (that includes dipolar interactions) plus the Zeeman energy:

$$E(\theta, \varphi) = E_{anisotropy}(\theta, \varphi) + E_{Zeeman}(\theta, \varphi) \tag{2.2}$$

For a given function $E(\theta, \varphi)$, determination of M_H (magnetization projection over $\vec{H}$) is performed by a dynamical approach in which the single domain magnetization can switch between the available energy minima states at a rate determined by ν_{ij}, which is dependent on the applied field, given by,

$$\nu_{ij} = \nu_0 \exp(-\Delta E_{i,j} V / k_B T) \tag{2.3}$$

where ν_0 is the natural frequency of jumps attempts of electron spins (10^9 Hz), of the order of the Larmor precession frequency, denoted by $\nu_0 \sim 10^9$ Hz, and $\Delta E_{i,j} V$ are the energy barriers between such minima (ΔE_{ij} is the energy density barrier between minima i and j, and V is the particle volume) and can be calculated from the field dependent energy landscape.[84,85].

The magnetizatization is given by

$$M_H(\vec{H}) = M \sum_i p_i(\vec{H}) \hat{u}_i(\vec{H}) \cdot \hat{u}_H \tag{2.4}$$

where $p_i(\vec{H})$ are the probabilities of finding the magnetization at state i, $\hat{u}_i(\vec{H})$ are the director vectors of energy minima, dependent on the external field $\vec{H} = H\hat{u}_H$.

The quasi-static condition for the externally applied magnetic field in DC magnetometry can be reproduced by a slowly varying sinusoidal field ($H(t) = H_0 \sin \omega t \hat{u}_H$), of frequency much smaller (~ 1 Hz) than $\nu_0 \sim 10^9$ Hz. In this way, probabilities $p_i(\vec{H})$ become time-dependent functions $p_i(t)$ that can be calculated by numerically solving ordinary differential equations as:

$$\frac{\partial p_i}{\partial t} = \sum_{j \neq i} \nu_{j,i} p_j - \Big(\sum_{j \neq i} \nu_{i,j} \Big) p_i \tag{2.5}$$

This continuity equation reflects the fact that the increment of population i results from the balance between incoming jumps (first term) and outcoming jumps (second term) to or from the rest of the minimum states, with the conservation of magnetization condition given by $\sum p_i = 1$.

The simplest situation corresponding to a perfect uniaxial single domain nanoparticle, where $E(\theta, \varphi) = K_{uni}[1 - (\hat{u}_{uni} \cdot \hat{u}_m)^2] = K_{uni} sin^2\theta$, where $\hat{u}_m$ and $\hat{u}_H$ represent the particle magnetization and external magnetic field unit vectors, respectively, is schematically represented in Fig. 2.4.3.

Either because the whole chain is free to rotate around itself or because magnetosomes can be rotated relative to each other, simulations for the whole chain for a given orientation between the external field H and the chain axis (angle α, in the scheme of Fig. 2.8) must be averaged for the equally probable azimuthal orientations (between 0° and 360°) relative to the polar axis defined by the chain:

$$M(H) = \int_0^\pi M_H(H, \lambda) d\lambda \tag{2.6}$$

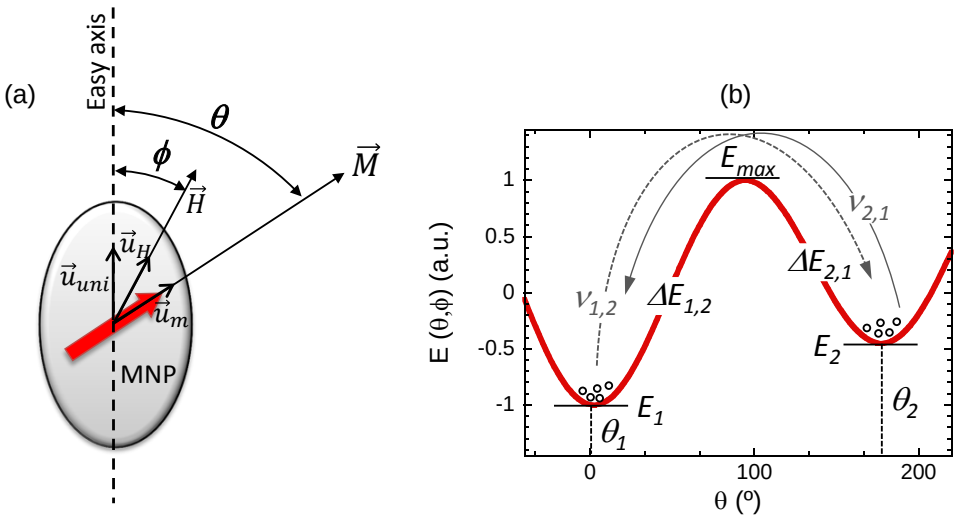

FIGURE 2.7: (a) Schematic representation of a uniaxial single domain magnetic nanoparticle (MNP). The large red arrow represents the magnetization. (b) Illustration of the energy landscape as function of θ in the presence of an arbitrary fixed external magnetic field.

where $M_H(H,\lambda)$ is the magnetization as a function of external field for a given orientation of the azimuthal angle λ, which exact definition will depend on the particular reference system of the problem (see fig. 2.8).

Except for the case of external field applied parallel to the chain ($\alpha = 0$), where all particles are equivalent by symmetry, the resultant hysteresis loop is calculated by averaging 18 single loops from $\lambda = 0°$ to $\lambda = 180°$ in steps of $10°$. In the random case (un-oriented bacteria), simulation is obtained by averaging simulations for all the orientations weighted by $\sin\alpha$. In this way, the simulation needs the calculation of 180 single simulations.

Previous works on *M. gryphiswaldense* show that the magnetic anisotropy of magnetosome chains can be described as a superposition of the cubic magnetocrystalline anisotropy of magnetite, with four equivalent easy axes directed along the $\langle 111 \rangle$ crystallographic directions, and a uniaxial shape anisotropy directed along the chain axis (thus parallel to one of the $\langle 111 \rangle$ axes) that originates from intra-chain dipolar interactions and dominates the magnetic response of the chain[86,87]. Following this argumentation, the single dipole energy density, E, is expressed as the sum of three contributions: i) cubic magnetocrystalline energy of magnetite with anisotropy constant K_c, ii) uniaxial anisotropy energy along the chain axis ([111] direction defined as $\hat{u}_{uni} = \hat{u}_{111}$ in Fig. 2.2d) with anisotropy constant K_{uni}, and iii) Zeeman energy in an external magnetic field $\mu_0\vec{H}$:

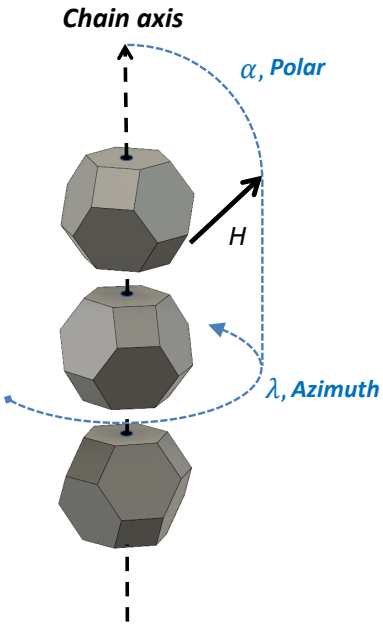

FIGURE 2.8: Polar (α) and azimuthal (λ) angles defining the orientation of the external field relative to the chain axis.

$$E(\theta,\varphi) = K_c \frac{[sin^4(\theta)sin^2(2\varphi) + sin^2(2\theta)]}{4} + K_{uni}[1 - (\hat{u}_{uni} \cdot \hat{u}_m)^2] - \mu_0 MH(\hat{u}_H \cdot \hat{u}_m) \tag{2.7}$$

Misalignments of the chains with respect to the aligning field that could occur during sample preparation have been considered by including a Gaussian angular distribution of the chain axes. Fig. 2.9 displays the simulated hysteresis loops obtained considering a uniaxial anisotropy directed along the chain axis and an angular distribution of 25 °. The data used for the simulations are the magnetocrystalline anisotropy constant ($K_c = -11\,\mathrm{kJ/m^3}$) and magnetization ($M_s = 48 \cdot 10^4\,\mathrm{A/m}$), characteristic of magnetite, and an effective uniaxial anisotropy constant along the chain axis $K_{uni} = 12\,\mathrm{kJ/m^3}$ to account for both shape and magnetic interaction anisotropies. Even though the simulations are good enough at the perpendicular orientation, that is to say, with the applied magnetic field perpendicular to the orientation of the bacterial chain axis, they clearly deviate at smaller angles as shown in the polar representation in Fig. 2.9c,d, where the experimental and calculated reduced remanent magnetization and coercivity of bacteria in 2D and 3D arrangements are plotted for different orientation angles between 0 and 90°.

Since the misalignment of the bacteria due to sample preparation, does not reproduce the hysteresis loops, we have tried a different approach in which we have considered that there is a tilting of the magnetization with respect to the chain axis inherent to the magnetosome. This approach allows reproducing accurately the ex-

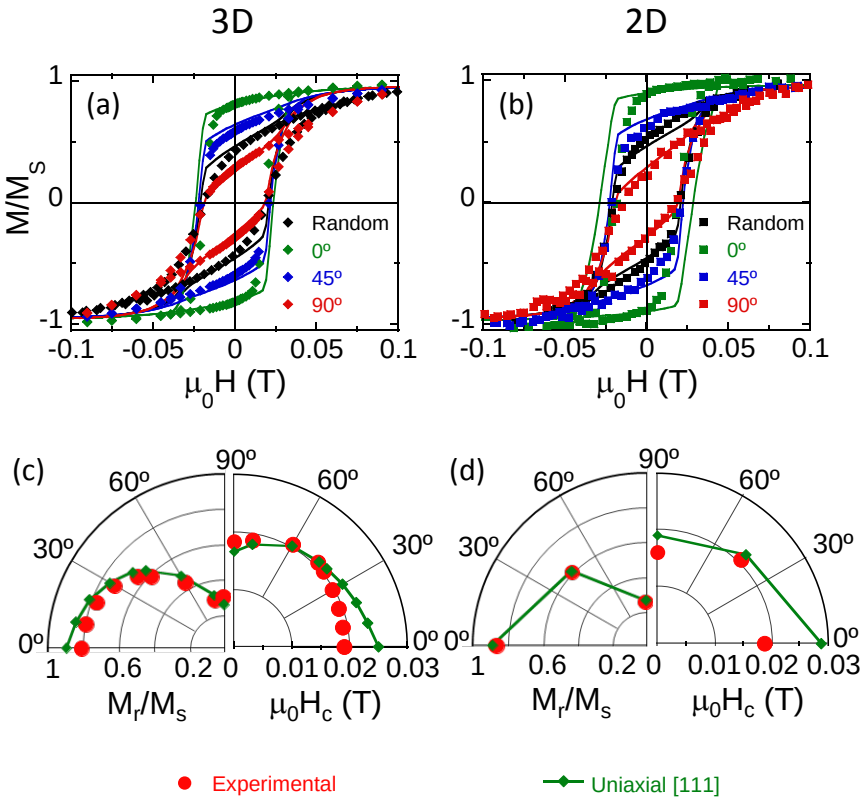

FIGURE 2.9: H
ysteresis loops of random and oriented bacteria in 3D and 2D arrangements compared to simulations considering an uniaxial shape anisotropy directed along the chain axis and an angular distribution of 25 °.] Hysteresis loops of bacteria in 3D (a) and 2D (b) arrangements forming 0°, 45°, and 90° with the aligning field ($\vec{H}_{al}$), together with the hysteresis loops of randomly arranged bacteria. Continuous lines correspond to the values obtained from the simulation considering an uniaxial shape anisotropy directed along the chain axis and an angular distribution of 25 °. Polar plots of the coercivity and reduced remanent magnetization at different orientation angles of the chain axis with $\vec{H}_{al}$ in the 3D (c) and 2D (d) arrangements. The experimental points are compared to the results obtained from simulations.

perimental hysteresis loops for both 2D and 3D arrangements by setting the uniaxial easy axis $\hat{u}_{uni}$ at 25° with the chain axis in eq. 2.7, in the plane containing the chain axis ([111]) and the [100] directions. By setting this angle, the effective easy axis, and as a consequence the equilibrium magnetic moment, is found to lie 20° out of the chain axis, in close agreement with the 25° tilting observed in the previous SANS analysis of the colloid (see Fig. 2.10). We used the same data for the simulations of the hysteresis loops at all orientation angles and for both 3D and 2D arrangements, $K_c = -11\,\mathrm{kJ/m^3}$, $M_s = 48 \cdot 10^4\,\mathrm{A/m}$ and $K_{uni} = 12\,\mathrm{kJ/m^3}$. The resemblance with experiment is more evident in the polar plots of the reduced remanent magnetization and coercivity shown in Figs. 2.10c,d.

The tilting of the magnetosome magnetization with respect to the chain axis is

attributed to the competition between the shape anisotropy of the magnetosome, which presents a well faceted morphology as shown in Fig. 2.2, and the magnetic interactions trying to align the magnetic dipoles along the [111] direction parallel to the chain axis. In fact, electron holography experiments on individual magnetosomes from *Magnetovibrio blakemorei* MV-1 clearly show that the magnetization direction of the particle is tilted with respect to the [111] crystallographic direction towards a long dimension of the particle, consistent with shape anisotropy dominating the magnetic state of the crystal[88].

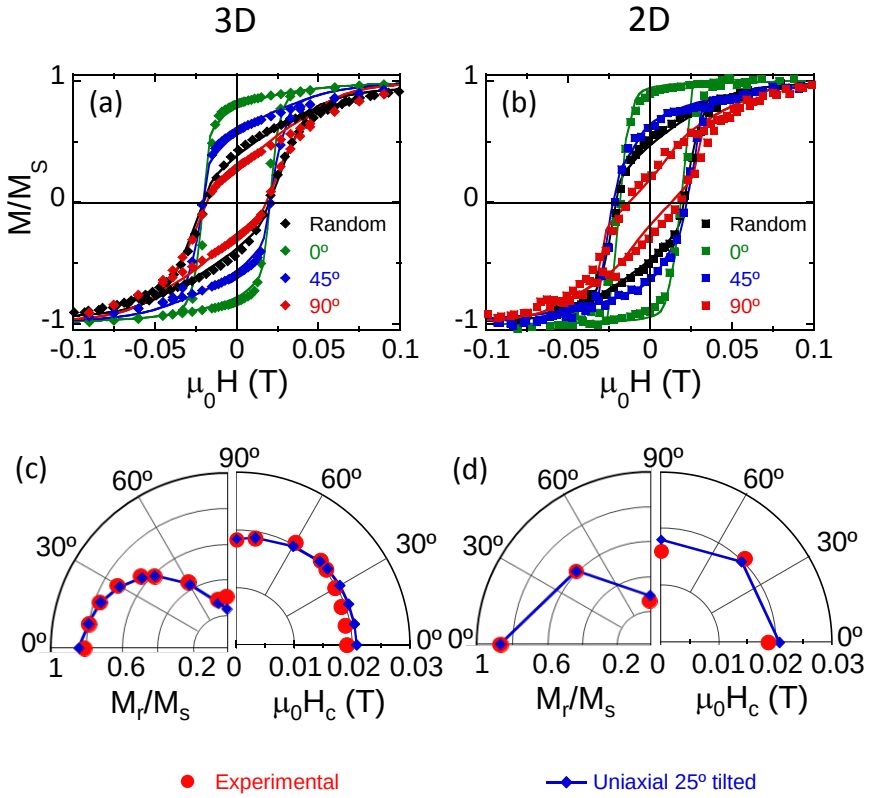

FIGURE 2.10: Hysteresis loops of bacteria in 3D (a) and 2D (b) arrangements forming 0°, 45°, and 90° with the aligning field ($\vec{H}_{al}$), together with the hysteresis loops of randomly arranged bacteria. Continuous lines represents the simulated hysteresis loops considering an uniaxial easy axis $\hat{u}_{uni}$ tilted 25° with the chain axis. Polar plots of the coercivity and reduced remanent magnetization at different orientation angles of the chain axis with $\vec{H}_{al}$ in the 3D (c) and 2D (d) arrangements. The experimental points are compared to the results of simulations.

2.4.4 X-ray photoemission electron microscopy (XPEEM) on extracted magnetosomes

Previous magnetic results are supported by x-ray photoemission electron microscopy (XPEEM)[89]. Unlike the macroscopic SQUID and VSM measurements above, which provide an average measurement of the whole sample, XPEEM is an element-specific

and spatially-resolved technique that by using x-ray magnetic circular dichroism (XMCD) as a magnetic contrast mechanism, allows obtaining element-specific magnetic hysteresis loops of selected sample areas with a resolution down to 30 nm[89].

XPEEM experiment was performed at the UE49_PGM SPEEM beamline at Helmholtz-Zentrum Berlin. Measurements were carried out at room temperature on extracted magnetosomes due to the high absorbing power of the whole bacteria. Two different samples were prepared: randomly arranged magnetosomes (Fig. 2.11b) and magnetically oriented magnetosomes (Fig. 2.11c). Sample preparation and experimental details are indicated in page 46 in *Materials and Methods* section.

In order to reach the maximum XMCD signal and high-contrast imaging, we performed an energy scan. For both, left (σ^-) and right helicities (σ^+) of the incoming circular polarized radiation, XAS images were obtained as the incoming photon energy crossed the Fe $L_{3,2}$ edges (690-730 eV). Computing of local X-ray absorption spectra (XAS) for σ^+ and σ^- allows calculation of the X-ray magnetic circular dichroism (XMCD) spectrum as $\sigma^+ - \sigma^-$ from a selected region.

Fig. 2.11a displays the XAS and the XMCD signal obtained from the chain parallel to the applied magnetic field enclosed in the green rectangle (Fig. 2.11b). As expected for magnetite, the L_3 XMCD signal shows three peaks (Fig. 2.11a): two minima at 707.4 eV and 709.6 eV and a maximum at 708.6 eV. The sign of the magnetic dichroism for each component is defined by the direction of its magnetic moment. Thus, the two minima correspond to the Fe^{2+} and Fe^{3+} ions occupying octahedral sites, and the maximum corresponds to the Fe^{3+} ions occupying tetrahedral places (see the crystal magnetite structure in Fig. 1.5). The subsequent magnetic contrast images were recorded by tuning the incoming photon energy to the Fe L_3 resonance, at 709.6 eV.

The set of magnetic images displayed in Figs. 2.11b,c show the space-resolved dichroic images obtained at different values of an in-plane magnetic field. The dichroic signal yields the magnetic moment, so that the hysteresis loops of selected areas of the magnetic images (enclosed in rectangles in Figs. 2.11b,c) have been obtained by plotting the corresponding dichroic signal as a function of the applied magnetic field (Fig. 2.11d). Note that even when the employed sample holder allowed the application of a pulsed magnetic field ranging ± 0.1 T to saturate the sample, during imaging the magnetic field range was restricted to ± 27.5 mT. A local background subtraction was performed by calculating the intensity variation observed within nearby regions with no magnetic particles (substrate). The XMCD is then calculated as the difference of background corrected σ^+ and σ^- divided by their sum, i.e. XMCD = $(\sigma^+ - \sigma^-)/(\sigma^+ + \sigma^-)$.

The hysteresis loops of the randomly deposited magnetosomes enclosed in the region marked with the black rectangle in Fig. 2.11b and of a chain parallel to the applied field, marked with the green rectangle in Fig. 2.11b, are shown in Fig. 2.11d.

Magnetosomes deposited under an applied aligning field form longer chains.

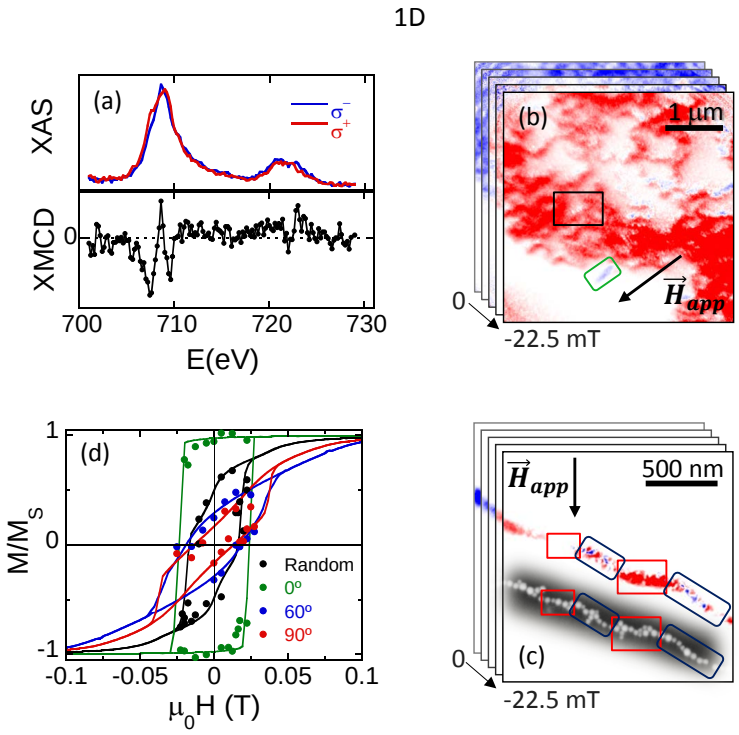

FIGURE 2.11: (a) X-ray absorption spectra (XAS) of the chain parallel to the applied field (green rectangle in (b) with the incoming beam right-polarized (σ^+) and left-polarized (σ^-). Computing $\sigma^+ - \sigma^-$ gives the XMCD signal below. (b) XPEEM images as a function of the applied field of random magnetosomes and (c) oriented magnetosomes deposited under $\vec{H}_{al}$. In (c) the SEM image of the chain is shown together with the XPEEM image. (d) X-ray photoemission electron microscopy (XPEEM) hysteresis loops of the regions enclosed in the rectangles marked in the images in (c) and (d), corresponding to chain sections which are either randomly arranged or forming 0° (green), 60° (blue), and 90° (red) with the applied field. The continuous line is the fit to the magnetic model explained in the text.

The XPEEM image together with the SEM image of one of these chains is shown in Fig. 2.11c. This chain is clearly not a straight line but is rather a zigzag, formed by segments oriented at different angles with the applied field. Two of these segments, enclosed in blue rectangles in Fig. 2.11c, form 60° with the applied field, and another two segments (red rectangles), form 90°. The corresponding hysteresis loops are shown in Fig. 2.11d.

As shown in Fig. 2.11d, the experimental XPEEM loops can be accurately simulated to the theoretical model developed previously for the 3D and 2D chain arrangements (eq. 2.7) with a smaller tilting angle of the effective easy axis (15°) and a larger anisotropy constant $K_{uni} = 16\,\mathrm{kJ/m^3}$ as compared to the SQUID loops ($K_{uni} = 12\,\mathrm{kJ/m^3}$). This is attributed to the larger distance between magnetosomes in chains inside the bacteria ($d = 60\,\mathrm{nm}$) than in chains of extracted magnetosomes ($d = 50\,\mathrm{nm}$). Indeed, for a 40 nm sized particle, the dipole pair potential energy is given by $\sim \mu_0 m^2/4\pi d^3 = 0.75\,\mathrm{eV}$ (being $m = M_s V$ the particle magnetic moment and $d = 60\,\mathrm{nm}$), while for the chains of extracted magnetosomes the dipolar energy

from the neighbors at $d = 50\,\text{nm}$ would increase up to $\sim 1.35\,\text{eV}$.

2.5 Equilibrium configuration of the chain

Following the results gathered from the magnetic analysis, here we will assess the impact on the magnetosome chain configuration of the tilting of the magnetosome magnetization with respect to the chain axis, where the latter, as noted above, is defined as the [111] crystallographic direction along which magnetosomes align in the chain (Fig. 2.12).

With this aim, we have developed an approach to explain the shape of the magnetosome chains that consists on quantifying the total energy of the chain by including the magnetostatic interactions between nanoparticles, and the contribution of the lipid/protein-based architecture embedding the magnetosome chain, modeled as a spring-like elastic energy. We focus on the stable geometry of chain arrangements and assume that close loop configurations such as rings or 3D clusters are avoided by the cytoskeleton inside bacteria. The same approach has been used by other authors[90,91], but in the present case, as proposed previously, the magnetization of each magnetosome is tilted 20° out of the chain axis.

Fig. 2.12 shows a section of a magnetosome chain composed of three magnetosomes. The particle in the centre is subjected to the stray magnetic field produced by the two neighbors (the dotted red lines in Fig. 2.12 represent the stray field produced by the particle at the bottom).

We implicitly assume that the local torque that tends to align neighboring dipoles is counter-balanced by the cytoskeleton, since cryotomography and TEM images reflect that the hexagonal faces are face to face[73,74]. The particle in the middle will tend to align its magnetization along the stray field lines and will undergo a magnetic force that compels it to shift towards the direction of its own magnetic moment. The magnetostatic energy associated to the magnetic force on magnetosomes is then implemented as the sum of the dipolar pair potential energies between nearest neighboring particles, where particles are taken as uniformly magnetized spheres:

$$U_m = \frac{1}{2}\frac{\mu_0 m^2}{4\pi}\sum_{i,j}^{N}\frac{1}{r_{ij}^3}[\hat{u}_i\cdot\hat{u}_j - 3(\hat{u}_i\cdot\hat{u}_{ij})(\hat{u}_j\cdot\hat{u}_{ij})] \tag{2.8}$$

where N is the total number of particles in the chain, $\hat{u}_i$ is the dipole unit vector of particle i, $\vec{r_{ij}} = r_{ij}\hat{u}_{ij}$ is the vector position of particle j from particle i. $m = M_s V$ is the magnetic moment of particles, where $V = \pi D^3/6$ is the volume and D the particle diameter. The magnetic moments m are assumed identical for simplicity, and according to the proposed anisotropy model they form a fixed polar angle of 20° with respect to the chain axis.

On the other hand, magnetite crystals are embedded in a lipid/protein-based architecture composed, among others, of the magnetosome membranes, the cytoskele-

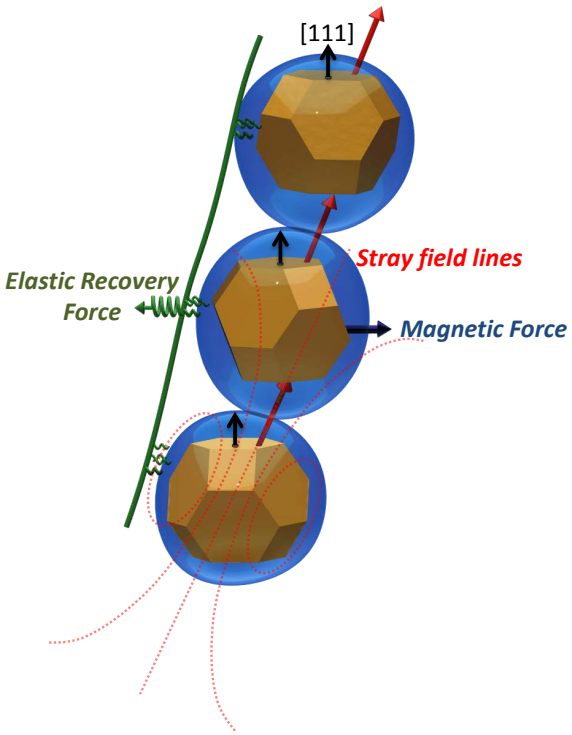

FIGURE 2.12: Equilibrium configuration of the magnetosome chain. Schematic representation of two competing mechanisms: magnetic force pushing to align magnetosome magnetic moments along the stray field lines from neighboring particles, and lipid/protein-based mechanism modeled as an elastic recovery force acting perpendicularly to the chain axis, where the chain axis is the [111] crystallographic direction along which magnetosomes align, as highlighted in the figure.

tal filaments, and the proteins connecting the magnetosome membranes with the cytoskeleton. The contribution to the total chain energy of this lipid/protein-based architecture is much more challenging to quantify. For the sake of simplicity we follow two assumptions. Firstly, we consider that the inter-particle distance is constant ($r_{i,i+1} \equiv d$). This means that chains can bend or twist but cannot stretch. Secondly, the forces exerted on each particle work like springs acting perpendicularly to the z axis and proportional to the projection on the horizontal plane of the relative vector positions. In this way, the spring-like elastic energy can be expressed as:

$$U_{elastic} = \frac{1}{2} k d^2 \sum_{i}^{N} [2 - (\hat{u}_{i,i+1} \cdot \hat{u}_z)^2 - (\hat{u}_{i,i-1} \cdot \hat{u}_z)^2] \tag{2.9}$$

Here, d is the center-to-center inter-particle distance and k is the elastic constant. Except for particles at both ends, each particle is subjected to forces from two nearest neighbors ($i+1$ and $i-1$), as expressed by the terms inside the summation in eq. 2.9. Fig. 2.13 sketches the orientation of the magnetic dipoles together with the elastic force acting on them.

The most stable chain configurations have then been predicted by minimizing

the total energy of the chain, $U = U_m + U_{elastic}$, considering three independent variables per particle, namely the radial (ρ) and azimuthal (ϕ) coordinates for the magnetosome positions, and azimuthal orientation (φ) of the magnetic dipoles (see sketch in Fig. 2.13b). The results have then been compared to the 3D reconstructions obtained from the chains imaged by ECT (Fig. 2.14).

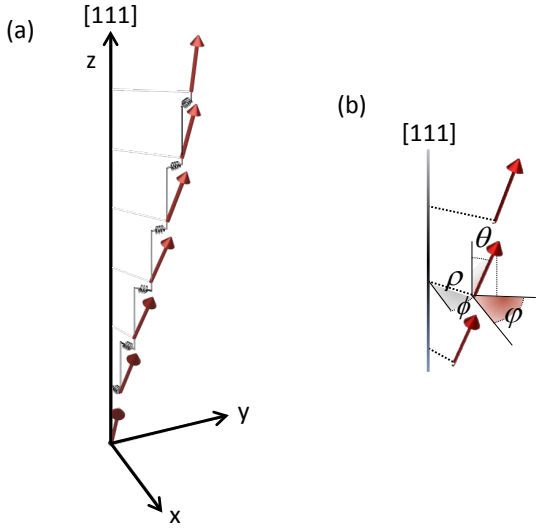

FIGURE 2.13: (a) Sketch showing the orientation of the magnetic dipoles and the elastic force acting on them. (b) Schematic representation of the magnetic dipoles and the three independent variables used in the simulation: radial (ρ) and azimuthal (ϕ) coordinates for the magnetosome positions, and azimuthal orientation (φ) of the magnetic dipoles. θ is the polar angle of the magnetic dipoles, fixed to 20°.

Considering a particle diameter $D = 40$ nm, distance between them $d = 60$ nm, and $k = 0.1 \cdot 10^{-3}$ N/m, three stable solutions give the patterns shown in Fig. 2.14b, in excellent match with the three experimental chain reconstructions shown in Fig. 2.14a. They are helical-like shaped chains with slowly bending axes and a different pitch, given by $\approx 2L/n$, being $L = Nd$ the chain length and $n = 1$, 2 and 3, respectively. The energy difference between the chains shapes is less than 1% of the total energy, hence they are approximately equally stable.

A zoom-in of a section of one of the simulated chains shows the magnetosome dipole moments. The azimuthal increment of the individual dipole orientations ($\Delta\varphi$) between consecutive positions along the chain increases with n approximately as:

$$\Delta\varphi \approx 2\pi\frac{n}{N} \tag{2.10}$$

Where N is the number of magnetosomes per chain ($N = 15$, 22 and 20 in the three examples shown). Consequently, the component of the chain magnetization vector (the vector sum of the magnetic moment of each magnetosome) perpendicular to the chain axis cancels out, so that the chain magnetization lies along the chain axis. Note also that when magnetic dipoles are projected in a 2D view of the chain,

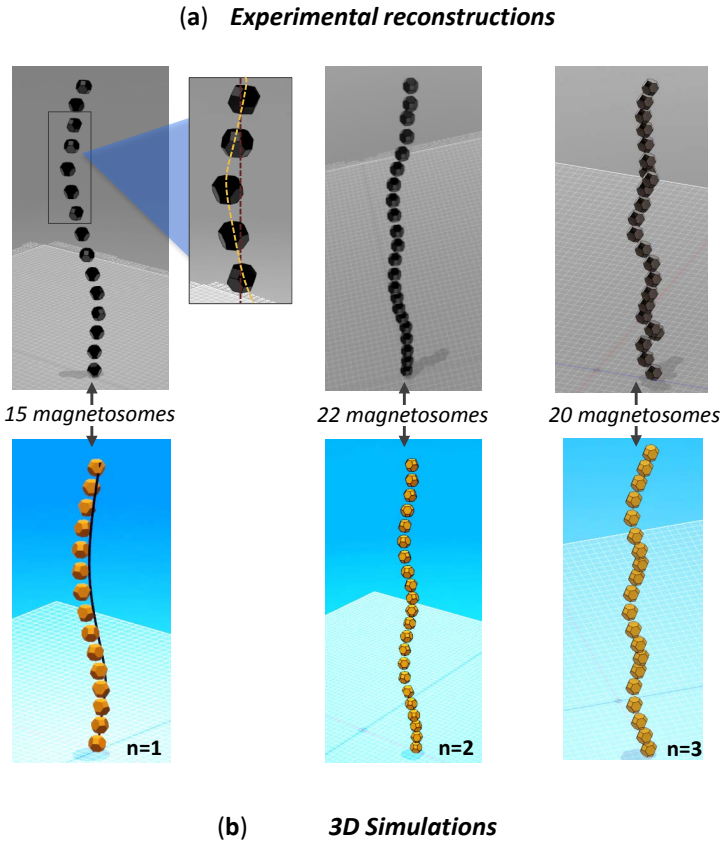

FIGURE 2.14: (a) Experimental reconstructions of the magnetosome chains obtained from ECT imaging shown in Fig. 2.1. A zoom-in of the first magnetosome chain reconstruction highlights the deviation from a straight line. (b) Three stable solutions for the chain patterns obtained as explained in the text.

apparent tilting between consecutive dipoles is no more than 7° (see Fig. 2.15), which is very compatible with projected electron holography images[92].

The role of k on the chain geometry is to scale up or down the radial positions of magnetosomes along the chain, so that larger k favours configurations approaching straight lines (see Fig. 2.16). k=0 leads to helical-shape chains purely driven by magnetic dipolar interactions. In our case, $k = 0.1 \cdot 10^{-3}$ N/m results in assembling forces of the order of 0.6 pN for radial displacements of $\approx$ 10 nm as obtained from the simulations, similar to the force generated by the actin filament[93], and far below recent estimations of the fracture limit of the actin-based scaffolding filaments ($\approx$ 30 pN) by Körnig *et al.*[94].

2.6 Summary

On the basis of our results, a mechanism of chain formation is proposed. Our findings reveal that the chain shape is mostly driven by passive spontaneous magnetostatic effects triggered by the intrinsic anisotropy of magnetosomes, ultimately de-

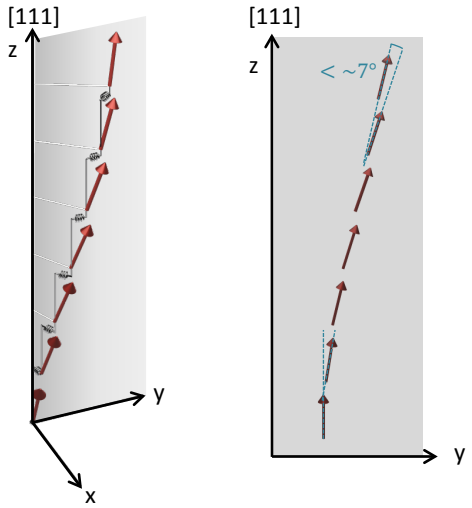

FIGURE 2.15: 2D projection on the yz plane of the magnetic dipoles configuration shown in the left.

fined by their morphology. The magnetosomes morphology is regulated during the biomineralization process. This is a genetically controlled process which involves a specific set of about 30 *Mam* (magnetosome membrane) and *Mms* (magnetic particle-membrane specific) genes[17]. The product of the *MamJ* gene is an acidic protein that connects the magnetosome membrane to the filament. The deletion of *MamJ* results in bacteria that produce magnetosomes arranged in compact three-dimensional clusters instead of arranged in chains[71]. The fact that they form clusters and not closed rings is consistent with our conclusions, namely the tilting of the magnetosome magnetic moment with respect to the chain [111] axis, since according to previous works, more than four magnetosomes tend to form closed rings when their magnetic moment is parallel to the [111] axis[90]. In the same way, when depositing the magnetosomes onto a 2D surface, magnetosomes tend to self-assemble in a close-packing configuration[59], and the tilting could be also behind the zigzag configuration of the chains observed by SEM in oriented magnetosomes.

But, why would this helical-like shape benefit the bacteria? *M. gryphiswaldense* are long cells, easily reaching several microns long. They need a high magnetic torque to overcome the drag forces and orientate along the Earth's magnetic field. As a consequence, their magnetosome chain needs to be long to maximize the chain net magnetic moment. Indeed, their chain is frequently composed of more than 20 magnetosomes, which brings the total length of the chain to 1.5 μm or more, about 50–60% of the bacterial length.

Such an object should necessarily be bent in order to accommodate to this spiral-shaped microorganism. Thus a helical-like shape fits better, but it only changes slightly the total magnetic moment, hence hardly affecting the magnetic orientation. A genetic control of the magnetosome shape towards an energetically optimum

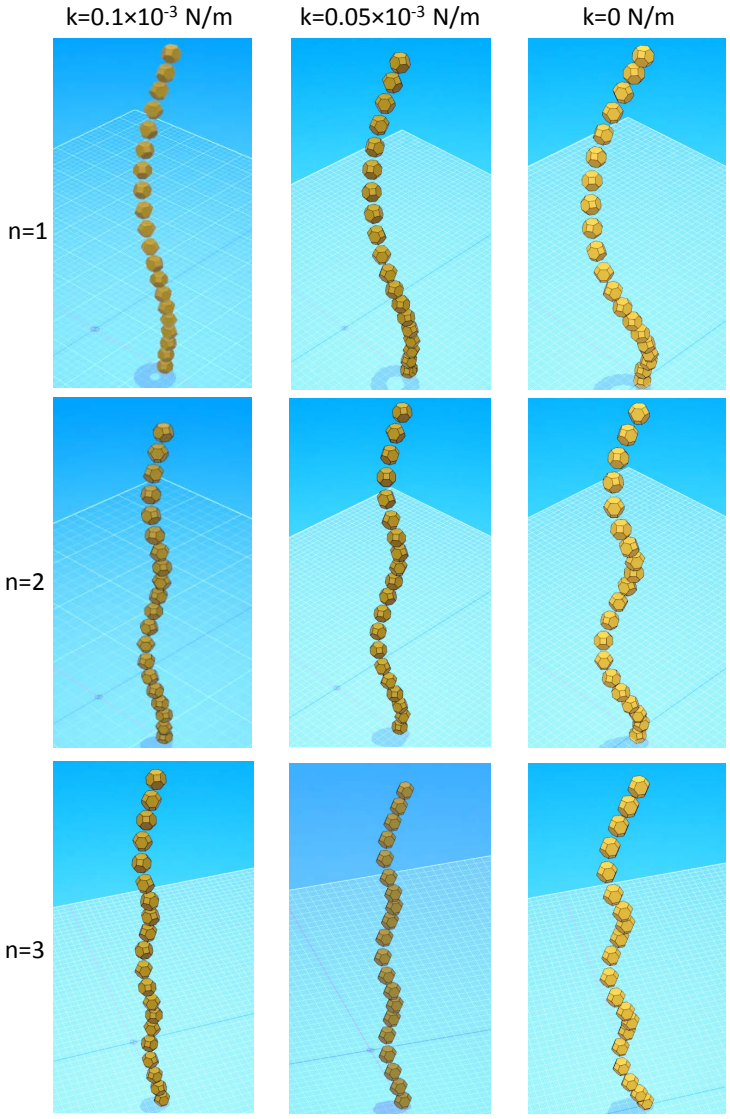

FIGURE 2.16: Chain geometries simulated for the three stable solution (n=1, 2, 3) described in the text for different values of the elastic constant k. Chains of 20 magnetosomes have been considered.

chain arrangement is also observed in *Magnetobacterium bavaricum* MYR-1, a species which synthesize bullet-shaped magnetosomes arranged into bundles of magnetosome chains. The magnetosome magnetization within MYR-1 magnetosomes is parallel to the chain axis, which coincides with the long axis of the magnetosomes. Unexpectedly, the latter is parallel to the [100] crystallographic axis, a magnetically hard axis in magnetite, rather than along the [111] magnetocrystalline easy axis, due to compromise effects of shape anisotropy and intra-chain and intra-bundle interactions[95].

Our finding sheds light on the understanding of the magnetosome chain assembly during the biomineralization process of MTB, which may influence their poten-

tial future applications as biological micro-robots. Indeed, one of the major technical issues in the development of interventional platforms for guiding drug-loaded MTB is the directional magnetic field strength that needs to be produced at the human scale to induce sufficient directional torque on the chain of magnetosomes. A good knowledge of the magnetic configuration of the magnetosome chain will lead to more efficient and less costly drug-delivery platforms that may benefice a larger population.

Materials and Methods

Electron cryotomography imaging (ECT)

Sample preparation for cryotomography was as follows: a 10 μl volume of fixed and washed *M. gryphiswaldense* cells (10^9 cel/mL) was mixed with a 3 μl volume of 10 nm Au nano-particles (Aurion®BSA gold tracer 10 nm) (used as fiducial markers). This mixture is frozen-hydrated following standard methods using a Vitrobot Mark III (FEI Inc., Eindhoven, The Netherlands).

In brief, a grid is placed in the controlled environment of the Vitrobot chamber, which is at 4°C and at a relative humidity of 95%. An aliquot (4 μl) of the sample is applied to a glow-discharged grid. After 1 min incubation most of the drop is removed by blotting with two filter papers, to produce a thin liquid film, and rapidly plunged into liquid ethane (91 K), previously cooled by liquid nitrogen.

Vitrified grids are stored under liquid nitrogen until cryo-TEM data collection. For cryo-tomographic tilt series acquisition, vitrified grids were cryo-transferred into a 914 high tilt tomography cryo-holder (Gatan Inc., Warrendale, PA, USA), which is inserted in a JEM-2000FS/CR field emission gun transmission electron microscope (Jeol, Europe, Croissy-sur-Seine, France) operated at 200 kV. Grids are kept around 103 K in the high vacuum of the microscope column containing the sample embedded in a thin layer of glass-like vitreous ice, in a near native-state.

Different single-axis tilt series were collected under low-dose conditions on a UltraScan 4000, 4k×4k CCD camera (Gatan Inc., Pleasanton, CA, USA), over a tilt range of $\pm 64^\circ$ with 1.5° increments and at underfocus values ranging from 5 to 8 μm, using the semi-automatic data acquisition software SerialEM[96]. Tilt-series were collected at a nominal magnification of $25,000\times$ and a binning factor of 2 (2048×2048 pixels micrographs), thus producing a pixel size of 0.95 nm. The in-column omega energy filter helped to record images with improved signal-to-noise-ratio by zero-loss filtering with an energy window of 60 eV centered at the zero-loss peak. CCD images in each tilt-series were acquired at the same underfocus value and under the same low-dose conditions. The maximum total dose used for a tilt-series was 90 electrons/Å^2 consisting of about 1-2 electrons/Å^2 for each digital image.

For the alignment and 3D reconstruction of the tilt-series, we used IMOD soft-

ware[97]. We employed the Au fiducial markers during the alignment process, and 3D reconstruction was carried out by weight back-projection followed by a reconstruction algorithm named Simultaneous Iterative Reconstruction Technique (SIRT). Resulting tomograms were visualized with ImageJ[98] as a sequence of cross sectional slices in different plane orientations. Tomograms were processed using a median filter and visualized as 3D electron density maps using UCSF Chimera[99] software.

Small angle neutron/x-ray scattering (SANS/SAXS) on a bacterial colloid

In a SAXS/SANS experiment the x-ray/neutron beam ($\vec{k}_{IN}$) hits the colloidal sample and the scattered beam ($\vec{k}_{scat}$) impacts on a 2D detector perpendicular to the incoming beam (Fig. 2.17).

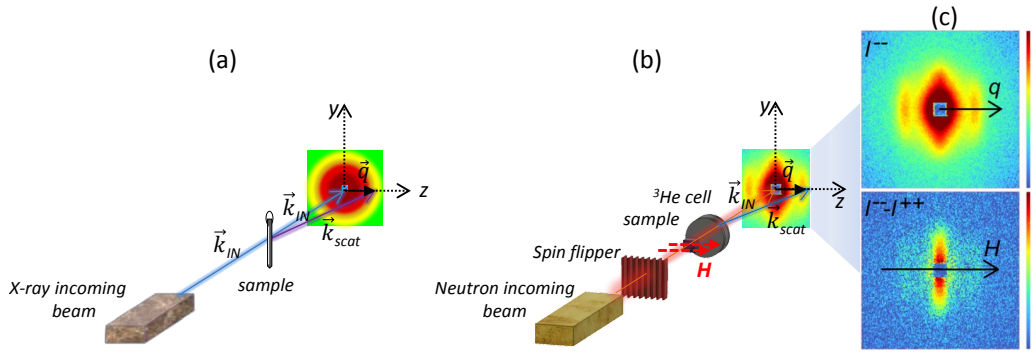

FIGURE 2.17: Schematic representation of the (a) SAXS and (b) SANS experiment. In SANS, the polarized incoming neutron beam can be set to either parallel (+) or antiparallel (-) to the applied field by means of an RF spin flipper. The ^{3}He cell discriminates the polarization of the scattered neutrons (+ or -), hence the recorded intensity is either I^{++} or I^{--}, where superindexes refer to the polarization of the incoming/scattered neutrons. (c) 2D SANS scattering patterns for $\mu_0 H = 2\,\mathrm{mT}$. Top: I^{--}; bottom: $I^{--} - I^{++}$

The SAXS data were at collected in a Xenocs Nano-InXider utilizing a 40 μm microfocus Cu anode as X-ray source and a multilayer monochromator to collect only the Cu-Kα radiation. The detector (a Pilatus 3) is at 938 mm from the sample, spans an area of 83.8×33.5 mm^2 and a pixel size of 172× 172 μm^2.

On the other hand, SANS data were collected in instrument D33 at the Institut Laue Langevin (ILL, Grenoble, France)[80,81]. A homogeneous magnetic field $\vec{H}$ was applied perpendicular to the neutron beam ($\vec{H} \perp \vec{k}$) with field amplitudes of $\mu_0 H$=2 mT and 1 T. The mean wavelength of the neutrons was $\lambda = 0.6\,\mathrm{nm}$, with a wavelength spread of $\Delta\lambda/\lambda = 10\%$. The scattering intensities were measured at two different detector distances (3 m as well as 13.4 m) giving a q-range of about $0.05 - 0.5\,\mathrm{nm}^{-1}$.

Magnetic measurements

Magnetic measurements on bacteria forming 2D and 3D arrangements were performed on a superconducting quantum interference device magnetometer (SQUID, Quantum Design MPMS-7) in DC mode and on a vibrating sample magnetometer (VSM). Isothermal magnetization loops were recorded between ± 1 T at 300 K.

The 2D bacterial configurations were prepared by depositing five 5 μL drops of the bacterial suspension (10^9 cell/mL) by the drop coating method[59,100] onto a Si substrate. For the oriented bacteria, the deposition was done under an external applied magnetic field of 0.5 T. To obtain homogeneous samples, infrared radiation was used during the deposition aimed at accelerating the drying and minimising the surface tension. The resulting samples were finally oriented at different angles with respect to the applied magnetic field.

Similar samples were deposited onto 300 mesh carbon-coated copper grids to analyze the goodness of the alignment by Transmission electron microscopy (TEM). TEM images were obtained with a JEOL JEM-1400 Plus electron microscope at an accelerating voltage of 120 kV. TEM images of randomly oriented and aligned *M. gryphiswaldense* cells deposited onto a Si substrate are shown in Fig. 2.5a.

The 3D bacterial configurations were prepared by resuspending 250 μL of a bacterial colloid (10^{11} cell/mL) in 750 μL of an agar solution (2% agar and 98% water) at 80°C to maintain the solution in a liquid state. To align the bacteria, a uniform magnetic field of 1 T was applied. After 3 minutes, the field was turned off, and the sample was cooled using liquid nitrogen until the temperature reached around 0°C. This caused the agar to solidify, trapping the bacteria, and keeping this solid state at room temperature.

X-ray photoemission electron microscopy (XPEEM) on extracted magnetosomes

For the X-ray photoemission electron microscopy (XPEEM) experiments isolated magnetosomes extracted from the bacteria were employed. Two different samples were prepared. The first one consists of randomly arranged magnetosomes prepared by the deposition of a 5 μL drop of the magnetosome suspension onto a conductive Si substrate. The drop was dried under infrared radiation. The second sample consists of magnetically oriented magnetosomes. In this case, the drop was dried under an external magnetic field of 0.5 T and infrared radiation. The Si substrate was marked with an Au reticule to allow subsequent match by scanning electron microscopy (SEM) of the chains imaged by XPEEM.

Magnetic imaging of the isolated magnetosomes was performed at room temperature by means of photoelectron emission microscopy (PEEM) by using X-ray magnetic circular dichroism (XMCD) as magnetic contrast mechanism. XMCD is based on the differential absorption between right and left circularly polarized x-

ray. The difference arises from the imbalance of the spin-up/spin-down electrons in ferri- and ferromagnetic materials. The spin-selectivity in the x-ray absorption process leads to a XAS with different peak intensities for the different helicities . XMCD is then calculated as the difference of the two absorption spectra (see Fig. 2.18a).

Measurements were carried out at the UE49_PGM SPEEM beamline at Helmholtz-Zentrum Berlin. The schematic layout of the XPEEM experiment and the XMCD mechanism are presented in Fig. 2.18b. The sample is placed on the top of a magnetic yoke. Two symmetric solenoids attached to the sample holder allowed application of an in-plane pulsed magnetic field ranging ± 0.1 T to saturate the sample. During imaging the magnetic field range was restricted to ± 27.5 mT. X-ray beam hit the sample and the emitted photoelectrons are collected by the objective lens after passing through an accelerating voltage of 20 kV[101]. The incoming photon energy was tuned to the Fe L_3 resonance (709.6 eV) to obtain element specific XMCD images of the magnetosomes as a function of the applied magnetic field. At each field a sequence of images was acquired with incoming circular polarized radiation (90% of circular photon polarization) with left (σ^-) and right helicity (σ^+), respectively. To improve statistics we acquired up to 400 images per helicity and field (3 s of exposure time). After normalization to a bright-field image, the sequence was drift-corrected, and frames recorded with same helicity were averaged.

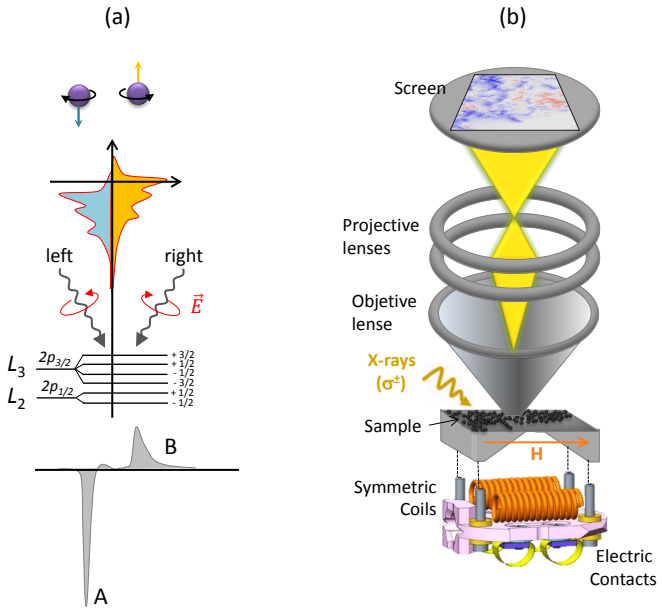

FIGURE 2.18: (a) XMCD mechanism diagram. (b) Schematic drawing of the photoemission electron microscope installed the BESSY II beamline.

Space-resolved XAS and XMCD spectra: For both, left and right helicities of the incoming circular polarized radiation, five stack of images were obtained as the in-

coming photon energy crossed the Fe $L_{3,2}$ edges. The photon energy was varied between 690 eV and 730 eV in 0.2 eV steps. Total integration time per energy was 2.5 s. After normalization to a bright-field image, the sequence was drift-corrected, and frames recorded with same helicity and photon energy were averaged. Computing of local X-ray absorption spectra (XAS) for σ^+ and σ^- allows calculation of the X-ray magnetic circular dichroism spectrum as $\sigma^+ - \sigma^-$ from a selected region.

XMCD images: Displayed XMCD images were obtained by computing XMCD = $((\sigma^+ - \sigma^-)/(\sigma^+ + \sigma^-))$. Due to the low signal, the XMCD strength at the regions of interest was comparable to the noise level at nearby regions with no magnetic particles. In order to enhance the magnetic contrast, for visualization purposes only, the XMCD images have been multiplied by the X-ray absorption image, i.e. XAS= $\sigma^+ + \sigma^-$ after background subtraction.

Space-resolved magnetic hysteresis loops: The data analysis allowed obtaining the magnetic hysteresis loop of any region within the field of view. In order to obtain the magnetic hysteresis (XMCD vs magnetic field) of a selected magnetosome region we computed the intensity as a function of field and helicity (σ^+ and σ^-) on the selected area. A local background subtraction was performed by calculating the intensity variation observed within nearby regions with no magnetic particles (substrate). The XMCD is then calculated as the difference of background corrected σ^+ and σ^- divided by their sum, i.e. XMCD = $(\sigma^+ - \sigma^-)/(\sigma^+ + \sigma^-)$.

Scanning Electron Microscopy (SEM)

SEM imaging was performed on the two magnetosome samples measured in XPEEM (magnetically oriented and randomly arranged). SEM images were collected at 10 kV with a JEOL JSM-7000F equipped with secondary and retro dispersive electron detectors.

List of publications resulting from this Chapter

1. D. Peddis, G. Muscas, R. Mathieu, P. Anil Kumar, G. Varvaro, G. Singh, I. Orue, D. Gil-Carton, L. Marcano, A. Muela, and M. L. Fdez-Gubieda, "Studying nanoparticles' 3D shape by aspect maps: Determination of the morphology of bacterial magnetic nanoparticles", *Faraday Discussion*, vol. 191, pp. 177-188, 2016.

2. I. Orue, L. Marcano, P. Bender, A. García-Prieto, S. Valencia, M. A. Mawass, D. Gil Carton, D. Alba Venero, D. Honecker, A. García-Arribas, L. Fernández Barquín, A. Muela, and M. L. Fdez-Gubieda, "Configuration of the magnetosome chain: a natural magnetic nanoarchitecture", *Nanoscale*, vol. 10, no. 16, pp. 7407-7419, 2018.

Chapter 3

Magnetosome biomineralization

3.1 Introduction

The biomineralization of magnetosomes is a complex biochemical process genetically controlled. Up to date, more than 30 specific genes implicated in magnetosome biomineralization have been identified[17]. Even though the biomineralization process[15,20,102] is not well understood yet, different steps have been well described.

First, the magnetosome vesicles are formed in the cell by invagination of the cytoplasmic membrane. The vesicle acts as a "nano-reactor" in which the conditions of the nanocrystal nucleation and growth (pH, redox, etc.) can be controlled, and at the same time, protects the cell from harmful byproducts[103]. The vesicle will grow up to a certain size before the magnetite nucleation process starts. This seems to allow supersaturation of Fe to facilitate nucleation[104]. Depending on the bacterial strain, these vesicles will keep connected to the cytoplasmic membrane during all the stages of the biomineralization process, as in the case of *Magnetospirillum magneticum* AMB-1, or they will quickly detach from the external cell membrane, like in the case of *Magnetospirillum gryphiswaldense* MSR-1. This suggests a variation in membrane biogenesis between different species.

As the vesicles are formed, the magnetosome membrane is targeted by several proteins (MamA, MamP, MamY, etc.), most of which are encoded in a conserved genomic segment named the magnetosome island (MAI) [105], although it is still not well known how the process works[15]. These proteins will control, among other things, the size, shape and morphology of the biomineralized nanoparticles.

Then, iron is transported into the vesicle and mineralized as a nanocrystal.

Magnetosomes are aligned into chains through the interaction of the magnetosomes with a cytoskeletal filament that traverses the cell, as described in Chapter 2.

All steps are regulated by a complex genetic machinery which has been thoroughly described in the literature[17]. In this Chapter we address the biomineralization of the magnetite crystals.

The intracellular formation of the magnetite nanocrystal inside the magnetosomes requires first the transport of iron from the surrounding environment into the cell. Three possible routes have been proposed for the iron uptake: *i)* iron is introduced into the vesicle when it is still attached to the cell membrane, *ii)* (alternative to *i*,but not mutually exclusive) iron is first taken up by cellular iron transport systems and then introduced into the vesicle through specific transporters, and *iii)* iron is transported from the cytoplasmic membrane to the magnetosome membrane by ligation to unknown organic substrates[17]. Recent studies seem to indicate that in some species the Fe is stored as a compound inside the cytoplasm before being introduced into the vesicle[106]. It has also been shown that magnetotactic bacteria are capable of taking up either Fe^{2+} or Fe^{3+}, and this process involves in some cases the use of iron chelators called siderophores[107]. Although no mechanism common to all the magnetotactic bacteria has been revealed yet, several proteins involved in this process have been identified. In order to synthesize magnetite nanocrystals, the conditions of the reaction need to be carefully adjusted inside the magnetosome (oxygen level, pH, etc.). Environmental conditions seem to also influence the physicochemical conditions in the interior of the magnetosomes. The nucleation of the magnetite nanocrystals starts when iron ions crystallize under optimal conditions ($pH > 7$ and low redox potential).

Regarding the magnetite nucleation, different models have been proposed. First, by means of Mössbauer spectroscopy and transmission electron microscopy (TEM), Frankel et al.[108] suggest that magnetite is formed from a ferrihydrite precursor, which in a later work[73] is suggested to form an amorphous phase located on the surface of not fully developed magnetite particles. On the other hand, Faivre et al.[109], using the same techniques in a time-resolved study, do not find evidence of the existence of a mineral precursor, and suggest as a possible mechanism of magnetite biomineralization a fast coprecipitation of Fe^{2+} and Fe^{3+} ions within the magnetosome vesicle, a hypothesis that was proposed earlier by Arakaki et al.[110] According to Faivre et al.[109], these Fe^{2+} and Fe^{3+} ions would be converted into an intracellular ferrous high-spin species (Fe^{2+}) predominantly located in the membrane and into a membrane-associated ferritin (Fe^{3+}). The role of ferrihydrite as a source of Fe for magnetite biomineralization has also been suggested by Watanabe et al.[111] by means of Raman spectroscopy. A different mechanism is proposed by Staniland et al[112]. In this work, by means of x-ray absorption spectroscopy and x-ray magnetic circular dichroism on the soft Fe $L_{2,3}$-edges, they found a shell of an Fe oxide, hematite (α-Fe_2O_3), around the magnetite particles, which they suggest acts as the precursor of magnetite.

In 2013 our group studied the biomineralization process of the magnetotactic bacteria *Magnetospirillum gryphiswaldense* strain MSR-1 in a time-resolved magnetic and structural study[113]. By means of Fe *K*-edge x-ray absorption near edge structure

(XANES) and high-resolution transmission electron microscopy the group identified and quantified two phases of Fe (ferrihydrite and magnetite) involved in the biomineralization process, confirming the role of ferrihydrite as the source of Fe ions for magnetite biomineralization in *M. gryphiswaldense*. We distinguished two steps in the biomineralization process: the first, in which Fe is accumulated in the form of ferrihydrite, and the second, in which the magnetite is rapidly biomineralized from ferrihydrite. XANES analysis suggests that the origin of the ferrihydrite could be at bacterial ferritin cores, characterized by a poorly crystalline structure and high phosphorus content.

The physiological role of ferritin-like proteins is dual: storing Fe, an essential nutrient, and protecting cells from potentially toxic effects of excess free Fe^{2+} [114–118]. There are three types of ferritin-like proteins in prokaryotes: bacterioferritin (Bfr), bacterial ferritins (Ftn) and DNA-binding proteins from starved cells (Dps proteins) [119]. Among them, Bfr has been the only protein identified so far in magnetotactic bacteria [120,121], suggesting that it should be the one involved in the biomineralization process. This protein is composed of 24 similar or identical subunits self assembled into a hollow globular shell that contains an iron core consisting of a ferric oxyhydroxide mineral similar to the nanomineral ferrihydrite with a high phosphate content (Fe:P 1:1) [122] .

In order to shed light on the mineral evolution which takes place in the biomineralization process, in this Chapter we present a time resolved structural study of the biogenesis of magnetite. At the same time, we analyze native prokaryotic cores from Bfr of *Escherichia coli* as a feasible initial phase. Thus, we made use of state-of-the-art techniques such as x-ray absorption fine structure (XAFS), high resolution transmission electron microscopy (HRTEM) and electron energy loss spectroscopy (EELS), plus other laboratory techniques.

3.2 Growth Conditions

Here I will describe the growth conditions of the two cultures employed along the Chapter. On the on hand, we cultivated *E. coli* overexpressing Bfr aiming to characterize the protein core with the different techniques and prove its role in the biomineralization process. On the other hand, we performed a time-course experiment to analyze the process at the different stages of the biomineralization.

Bacterioferritin (Bfr)

Aiming to produce vast quantities of protein cheaply and rapidly, bacterial expression systems are typically used, being *E. coli* one of the most popular hosts for this purpose. Protein expression in bacteria is quite simple. DNA coding for the protein of interest is inserted into a expression vector that is introduced into the bac-

terial cells. Then the transformed cells are grown so that they produce the desired protein.

In our particular case, *E. coli* DH5-α harbouring plasmid pGS281(*bfr, Apr*)[123] that overexpresses Bfr were prepared. The cultures were grown aerobically at 37°C and 250 rpm in Luria Bertani Broth (LB) supplemented with 100 μg mL^{-1} Fe(III)-citrate and with 100 μg mL^{-1} ampicillin to assure core mineralizetion. *E. coli* DH5-α strain was growth to the stationary phase. Cells were harvested by centrifugation at 4°C and 5500 rpm for 15 min and washed three times in PBS.

Time-Course Experiments *M. gryphiswaldense* non magnetic cells were obtained after 4 or 5 passages in a free-iron medium (t=0 min) incubated under aerobic conditions (agitation at 170 rpm). To induce the magnetite biomineralization, iron starved cells at mid-logarithmic growth phase were harvested by centrifugation and transferred into a fresh medium supplemented with 100 μM of Fe(III)-citrate. To minimize the effect of physicochemical gradients generated in big flasks, the experiment was performed in separate 60 mL-flasks with 50 mL-subsamples of the same Fe culture. The entire subsample was processed each time. Culture was carried out at 28°C under microaerobic conditions (without agitation). At specified times after the iron incubation, from t=0 to 1440 min, the cells were collected and fixed in 2% glutaraldehyde. Later, cells were harvested by centrifugation at 4°C and 6200 rpm for 15 min and washed three times in mQ water for subsequent analysis.

The formation of magnetosome chains along the biomineralization process was monitored by optical density (OD) assays. This method is based on the differential light scattering properties of magnetic cells (those with magnetosome chain) suspensions whose long axes are aligned parallel or perpendicular to a light source. If the applied magnetic field is directed parallel to the light beam, a minimum scattering occurs, whereas a perpendicular orientation with respect to the light results in maximal scattering . When $H = 0$, magnetic cells are randomly oriented leading to an intermediate scattering intensity. C_{mag} (coefficient of magnetically induced differential light scattering), which is defined as[124],

$$C_{mag} = \frac{OD_{max}}{OD_{min}} - 1 \tag{3.1}$$

correlates well with the presence of magnetosome chain in cells. Thus, it is maximum if all cells are aligned parallel to the magnetic field lines. Schematic representation of the physical fundament together with technical details of the C_{mag} measurements can be found in *Materials and Methods* section (page 72).

Fig 3.1 displays the evolution of the C_{mag} coefficient along the biomineralization process. At early stages, low values are obtained due to the lack of magnetosome chain in cells. From 60 min on, a rapid increase of C_{mag} values takes place as consequence of the progressive formation of chains, reaching a plateau at 270 min, evi-

dencing the presence of magnetosome chain in most of the cells.

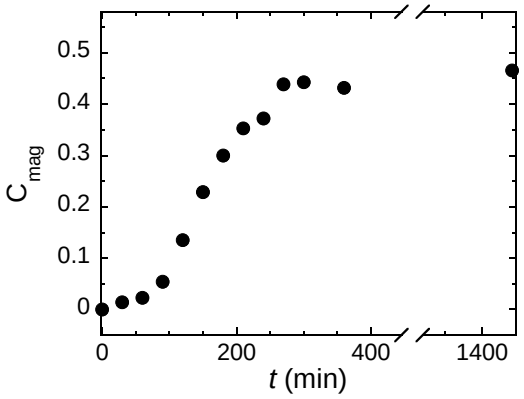

FIGURE 3.1: Coefficient of magnetically induced differential light scattering (C_{mag}) as function of the biomineralization time. Error bars representing the standard deviation estimated from three independent measurements are within the size of the point.

3.3 Transmission electron microscopy (TEM)

Transmission electron microscopy (TEM) allows to analyze Bfr and follow the magnetosome mineralization process and the formation of magnetosome chains at a glance. Details of sample preparation are specified in *Materials and Methods* section (page 72). The particle size distribution was analyzed using a standard software for digital electron microscope image processing, ImageJ[125].

Bfr presents a cage-like architecture of 12-13 nm diameter with a central cavity of several nanometers that essentially defines their function. TEM imaging can not see the case, only the core is distinguishable. The biomineral cores, that are reversibly formed inside the protein cages, are heterogeneous in size and can vary from 1 to 4500 iron atoms per protein cage, depending upon the cellular iron availability[114,122,126,127]. Fig. 3.2 shows the image of the Bfr nanoparticles together with the size histogram. The observed biomineral cores present spherical shapes with a mean size diameter of 3.5 nm.

On the other hand, Fig. 3.3 displays a series of TEM images with the corresponding size histograms at specific times after Fe incubation. As shown in Fig. 3.3, the number and size of magnetosomes increase as the process evolves.

At early stages, t=0 min, no magnetosome chains are evidenced, however some bacteria manifest the presence of odd subsistent well-formed magnetite magnetosomes at the initial point (Fig. 3.3, blue arrow). As the process evolves, the number of bacteria with magnetosomes does also increase. Magnetosome nucleation and growth takes place simultaneously in different regions of the cell, in the preexisting full-sized vesicles imperceptible by TEM due to the low contrast with the rest of the cell[21]. Thus, at 60 min, primitive chains composed of small subchains

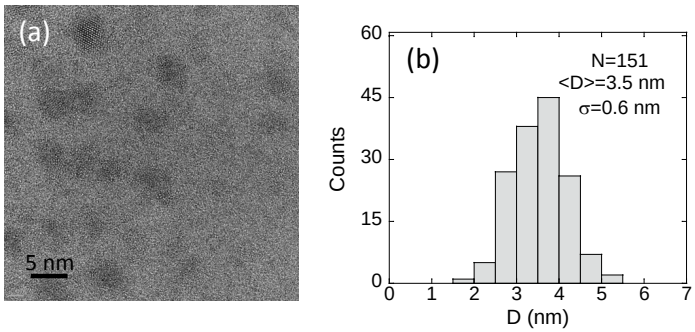

FIGURE 3.2: (a) TEM images of *E. coli* overexpressing Bfr and (b) size histograms. The number of particles analyzed (N), the mean diameter ($\langle D \rangle >$) and the standard deviation (σ) are presented on the top of the histogram.

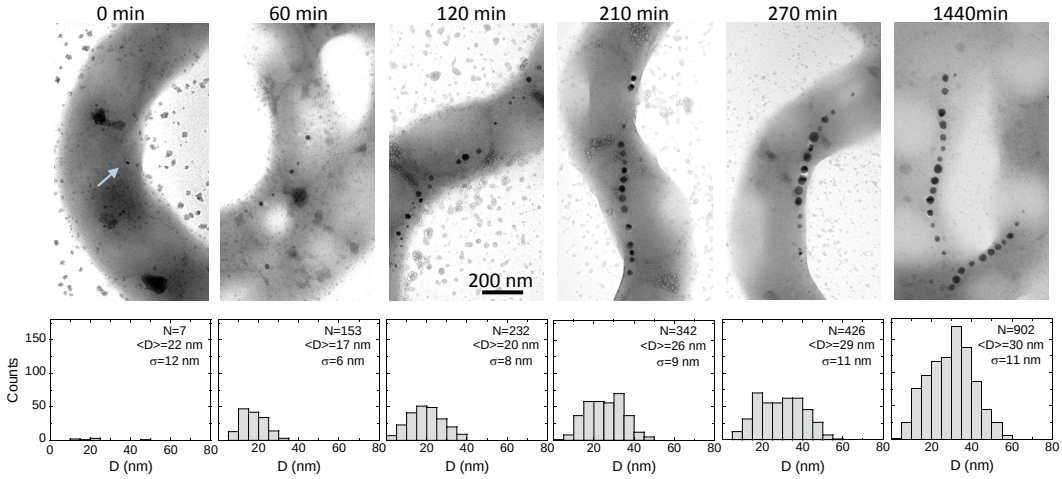

FIGURE 3.3: Time-resolved magnetosomes and chain formation followed by TEM together with their corresponding size-distribution histograms. The population of particles considered for the analysis (N), the mean diameter ($\langle D \rangle$) and the standard deviation (σ) of each biomineralization time have been added in the histogram.

are already distinguishable. These subchains are increasingly common and closer together (t=120 min). The integration of various of these subchains leads to more homogenous and longer chains as early as 210 min. From there on, magnetosomes chains are gradually better defined formed by increasingly bigger magnetosomes, obtaining arranges of 15-20 magnetosomes with a recurring center to center-distance of $\sim$60 nm. The chain-formation tendency is in good agreement with C_{mag} results presented above.

Similar evolutions have been reported in previous works[21,112,113,128,129]. However, it is worth highlighting the existence of discrepancies between the rates of magnetosome formation reported. Even for the same bacteria strain, biomineralization times vary widely from one culture to other. For example, Staniland et al.[112] reported the presence of full-sized magnetosomes and well-formed chains 15 min after the iron addition in *M.gryphiswaldense*, while our previous work evidenced long

chains from 240 min[113]. For that reason, biomineralization times should be considered just as guide values. The present case evidences an in-between rate, being faster than the previosly studied process by the group even when similar growth conditions were followed.

3.4 X-ray absorption fine structure (XAFS)

X-ray absorption fine structure (XAFS) spectroscopy provides valuable short-range structural information. XAFS consists on measuring a signal related to the absorption coefficient, $\mu(E)$, as a function of the x-ray incoming energy E around the binding energy of a core level electron in an atom. Since the energy of the absorption edge varies with the atomic number, XAFS is an element-specific technique in which we can select the element to study by tuning the energy of the incident x-ray photon. Details of technique are specified in page 73 of *Materials and Methods*.

The versatility of XAFS allows us to analyze matter in a wide range of concentrations, from 1 to 10^{-6} M. It is an important advantage for us, making possible to work with the whole cell, with low concentrations of magnetite, avoiding the process of extraction of magnetosome, specially limited at the earlier stages of the biomineralization process. It is worth noting that high doses of hard x-rays could damage the biological sample, however, no damage are expected in inorganic phases as magnetosomes.

Fig. 3.4 displays an example XAFS measurement where two regions can be distinguished: the near-edge (XANES: x-ray absorption near edge structure) and the extended (EXAFS: extended x-ray absorption fine structure). Each region provides different but complementary information. The XANES region starts with the jump of the absorption signal and extends up to 100-150 eV above the edge. The XANES features originate from the details of the density of states close to the Fermi level and the large multiple scattering phenomena, providing information on the electronic properties and the local geometry of the absorber. On the other hand, EXAFS is mainly due to single scattering events and provides quantitative information about local structure parameters: coordination numbers, interatomic distances and disorder of neighboring shells. More details on the information gathered from both regions, XANES and EXAFS, can be found in sections 3.4.1 and 3.4.2, respectively.

3.4.1 X-ray Absorption Near Edge Structure (XANES)

The shape and intensity of XANES features are determined by the density of empty states (DoS) close to the Fermi level and the full multiple scattering (FMS). Thus, this region provides information about the electronic properties of the absorbing atom and the symmetry of the local atomic structure around the absorber. The am-

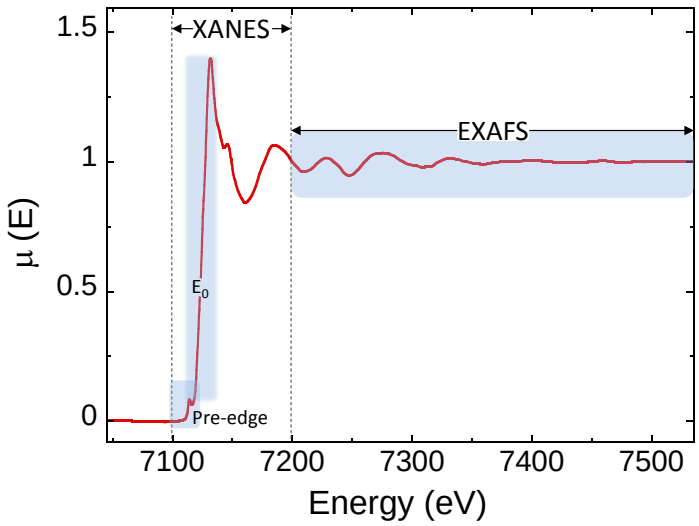

FIGURE 3.4: X-ray absorption spectrum of magnetite biomineralized by *M. gryphiswaldense* bacterium. The two characteristic regions, near-edge (XANES) and extended (EXAFS), are indicated.

plitude of the XANES features is much higher than EXAFS oscillations, being sensitive to low concentrated samples even down to 10^{-6} Molar. Hence, regardless the very small concentration of nanoparticles present in each bacterial sample (down to ppm of magnetite per sample), the high sensitivity of XANES allows obtaining good quality spectra.

The first time-resolved XANES study on *M. gryphiswaldense* bacterium was reported by the group in 2013[113]. In this work, they identify a initial phase as a phosphorous-rich ferrihydrite like-phase, and the final phase as magnetite. As already mentioned in TEM section, the paper discusses a slower biomineralization process than the covered in this Chapter combined with an initial state (t=0) essentially free of magnetite. It is worth noting that the presence of odd magnetosomes at early stages of the biomineralization process, as evidenced in our experiment by TEM, partially masks the spectroscopic signature of the precursor of the magnetosome biogenesis.

Fig. 3.5 displays the Fe *K*-edge XANES spectra of bacteria at the first step of the biomineralization process (t=20 min) presented by Fdez-Gubieda et al.[113], a sample essentially free of magnetosomes. It is presented together with XANES spectra of *E. coli* overexpressing Bfr and inorganic 6-line ferrihydrite synthesized at the laboratory following the method described by Pollard et al.[130]. All the analyzed samples present the same edge position, coincident with that of inorganic ferrihydrite, which is a clear indication of the Fe ions being Fe^{3+}. The low intensity of the pre-peak evidences a high centrosymmetric environment confirming the octahedral nature of the compounds[131–134]. The early stage of the biomineralization process was indentified as a ferrihydrite-like structure due to the similitude with ferrihydrite spectrum.

However, the bacterial spectrum presents a shoulder ∼7137 eV that is not present in the inorganic ferrihydrite. This shoulder has also been observed in $FePO_4 \cdot 2H_2O$[132], in poorly ordered ferric phosphates[106,135], and it has been related to the presence of phosphorous in the surrounding of the Fe atoms. It commonly appears in ferrihydrite cores of ferritin proteins with high phosphorous content, such as bacterial ferritin-like proteins[119,136]. Fig. 3.5 evidences the match between the XANES spectrum of the sample '20 min' and Bfr.

On the other hand, the sample obtained at t=1440 min (24h) after Fe incubation corresponds to the bacteria with fully formed magnetosome chains. A comparison of this spectrum with the one of bulk magnetite shows that both are identical (see Fig. 3.5).

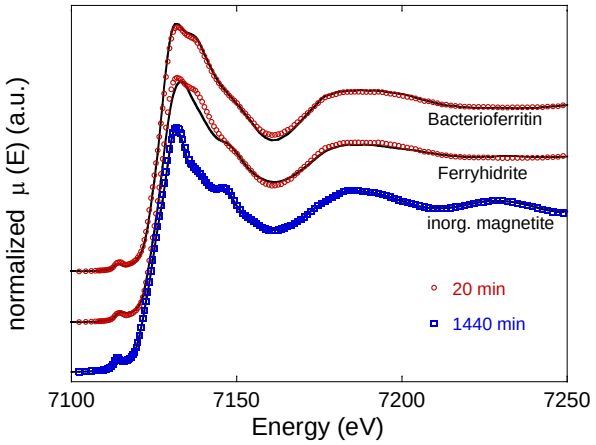

FIGURE 3.5: Comparison of the normalized XANES spectra of bacteria at t=20 min after Fe incubation, presented by Fdez-Gubieda et al.[113], with inorganic ferrihydrite and with *E. coli* overexpressing Bfr. And XANES spectra of bacteria at t=1440 min compared to inorganic magnetite.

Fig. 3.6 shows the evolution of the Fe K-edge XANES along the biomineralization process at energies below and above the absorption edge. Bfr spectrum has been also added as a feasible initial phase. The most relevant changes in spectra are observed in the three characteristic features distinguishable in the XANES region: the edge position ($E = E_0$), the pre-edge ($E < E_0$) and the post-edge ($E > E_0$).

The pre-edge region The pre-edge peak is observed $\sim$ 10 eV before the edge. At early stages of the biomineralization process, the Fe K-edge XANES spectra show a broad and low intensity pre-peak which transforms into a narrow and more intense peak as the process evolves (see 3.6.b). The width and intensity of the pre-edge peak depends on the symmetry around the absorbing atom. As mentioned earlier, the intensity of the pre-edge peak is smaller for octahedral compounds, with centrosymmetric sites, than for tetrahedral compounds[131–134]. Thus, this tendency suggests a increasingly tetrahedral environment when the biomineralization process evolves.

The edge position (E_0) The edge position defines the ionization threshold to the

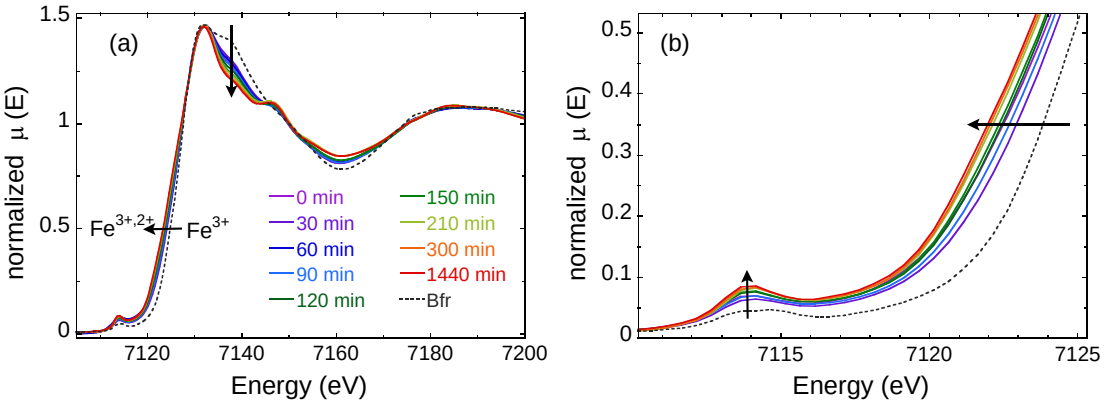

FIGURE 3.6: (a) Normalized XANES spectra at Fe *K*-edge obtained from the samples at specific times after the Fe incubation; (b) pre-edge region in a more-detailed depiction. Black arrows highlight the tendency of the spectra as the process evolves. Bfr spectrum is also presented as reference of initial-stages.

continuum state, being a clear-cut indication of the oxidation state of the absorbing atom. Two different methods are generally employed to assign the edge energy: i) the maximum in the derivative of the absorption coefficient and ii) the energy value at which the normalized absorption coefficient is 0.5. In the present thesis we have chosen this second procedure.

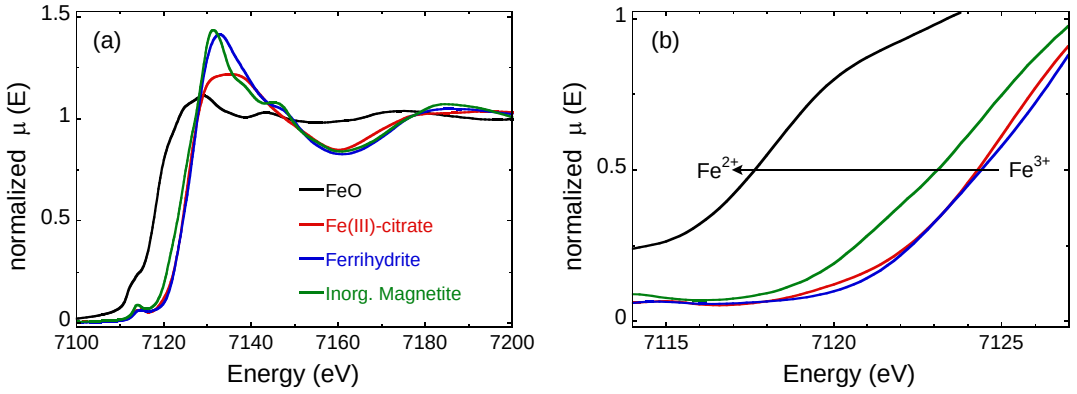

FIGURE 3.7: (a) Normalized XANES spectra of several Fe compounds: FeO (Fe^{2+}), Fe(III)-citrate (Fe^{3+}), ferrihydrite (Fe^{3+}) and magnetite (Fe^{2+},Fe^{3+}). (b) A detail that highlights the shift to lower energies of the absorption edge when reducing from Fe^{3+} to Fe^{2+}.

There is a linear relationship between E_0 and the oxidation state. The energy value shifts towards lower energy with decreasing oxidation state of the absorber. In fact, we have checked that the edge position displaces 7 eV to lower energies when the oxidation state decreases from Fe^{3+}, measured from Fe(III)-citrate and ferrihydrite, to Fe^{2+}, measured from the reference compound FeO (see Fig. 3.7).

The rightmost spectrum presented in Fig. 3.6 corresponds to Bfr, a pure Fe^{3+} compound (7124.9 eV) as previously indicated[113]. In this occasion, the spectra cor-

responding to the earlier stages of the biomineralization process are slightly shifted to lower energies compared to Bfr as a result of the presence of subsistent magnetosomes at earlier stages and a faster magnetosome formation in comparison to the reported by Fdez-Gubieda et al[113]. Nevertheless, there is a clear evolution when the biomineralization process evolves. For increasing times after the iron incubation, the energy of the absorption edge displaces ~ 2 eV to lower energies (24 h). It points out a partial reduction of Fe from Fe^{3+} to Fe^{3+}, Fe^{2+} oxidation states in a ratio 2/3 to 1/3 of the sample at 24 h after Fe incubation, in good agreement with the cation distribution of magnetite.

The post-edge region The post-edge region is dominated by multiple-scattering resonances of the photoelectrons ejected at low kinetic energy, providing information about the medium range order around the absorber atom[137–139].

In this region, it is worth noting the reduction of intensity in the shoulder observed at ~ 7137 eV when the process goes on. As mentioned above, this shoulder is related to the presence of phosphorous in the surroundings of the Fe absorbing atom[119,132,136]. Thus, it suggests a reduction of the phosphorous-rich phase as the process evolves.

Hence, according to the analysis presented above, the tendencies of the pre-peak, the edge and the post-edge region, evidence a evolution from the Bfr-core like phase to magnetite. Indeed, intermediate stages of the biomineralization process could be defined by the coexistence of both phases. Thus, in order to obtain quantitative information about the phase-ratio and its evolution with the time elapsed after the Fe incubation, the normalized spectra were fitted to a linear combination of two reference phases: Bfr and magnetite.

$$\mu(exp) = \alpha_{Bfr}\mu_{Bfr} + \alpha_{Fe_3O_4}\mu_{Fe_3O_4} \tag{3.2}$$

where α_{Bfr} and $\alpha_{Fe_3O_4}$ are the atomic fraction of Bfr and magnetite phases present in the sample, repectively.

Fig. 3.8 displays the linear combination fits of each individual spectrum together with the evolution of the atomic fraction of each reference phase as the biomineralization process evolves. From these data it can be readily seen that at the beginning of the biomineralization up to α_{Bfr}=0.5 is present in the cells. Then, the presence of magnetite with respect to Bfr rapidly increase.

In order to obtain representative information at the earlier stages of the biomineralization process, complementary samples were prepared. In this sense, a second and slower biomineralization process was carried out. From this new experiment, we considered two samples obtained at t=0 and 60 min after the iron incubation, which show a lower atomic fractions of magnetite: $\alpha_{Fe_3O_4}$=0.36 and 0.41, respectively (see empty markers in Fig. 3.8b). Thus, henceforth instead of represent our data as a

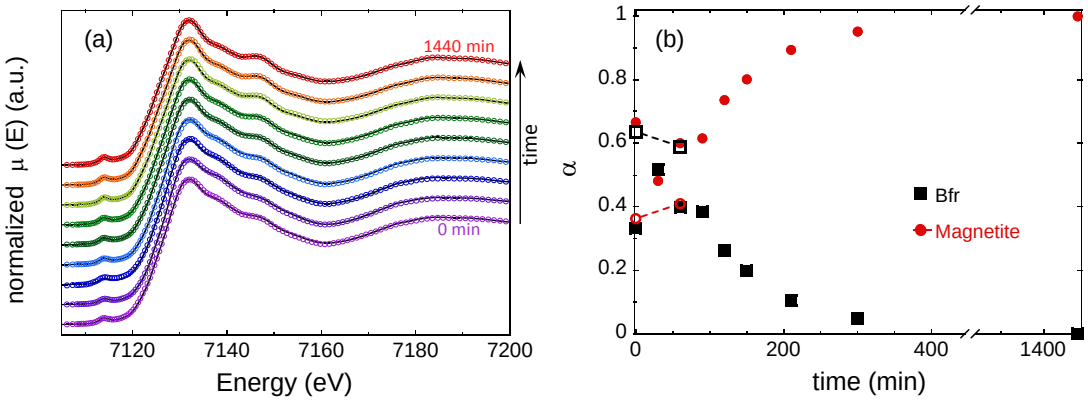

FIGURE 3.8: (a) Linear combination fits of normalized XANES spectra at the different times after Fe incubation considering Bfr and magnetite phases as references. (b) Evolution of the atomic fraction of Fe in Bfr and magnetite phases along the biomineralization process. Empty markers represent the atomic fraction of Fe obtained for a second and slower biomineralization process.

function of the incubation time, we will analyze the $\alpha_{Fe_3O_4}$ dependence.

3.4.2 Extended x-ray absorption fine structure (EXAFS)

In order to further evaluate the initial phase and the coexistence of both phases along the biomineralization process, we have carried out extended x-ray absorption fine structure (EXAFS) analysis.

EXAFS is the extended part of the absorption spectrum and extends from 50-100 eV above the edge position to 1-1.5 keV. This region is dominated by the single scattering-contributions and provides quantitative information about the local structure of the absorbing atom.

The EXAFS signal can be described as the consequence of the interference between the direct wave outgoing from the absorber and the waves scattered by the surrounding atoms. This phenomenon is schematically represented in Fig. 3.9. Hence, the amplitude and phase of the EXAFS oscillations are related to the number of neighbors, the type of scattering atom and the distances from the absorber.

Aiming to obtain this information, the oscillatory part of the absorption spectrum EXAFS signal, $\chi(k)$, was obtained by subtracting the free-atom absorption coefficient $\mu_0(k)$, calculated using a cubic spline in the k-range, to the absorption coefficient, $\mu(k)$, normalized by the absorption jump at the edge energy, $\Delta\mu_0(k)$:

$$\chi(k) = \frac{\mu(k) - \mu_0(k)}{\Delta\mu_0(k)} \tag{3.3}$$

In the case of an atomic Gaussian distribution around the absorbing atom, the local structure can be generally modeled as a sum of spherical shells j with average coordination number N_j at a mean distance R_j from the absorber. Since at a

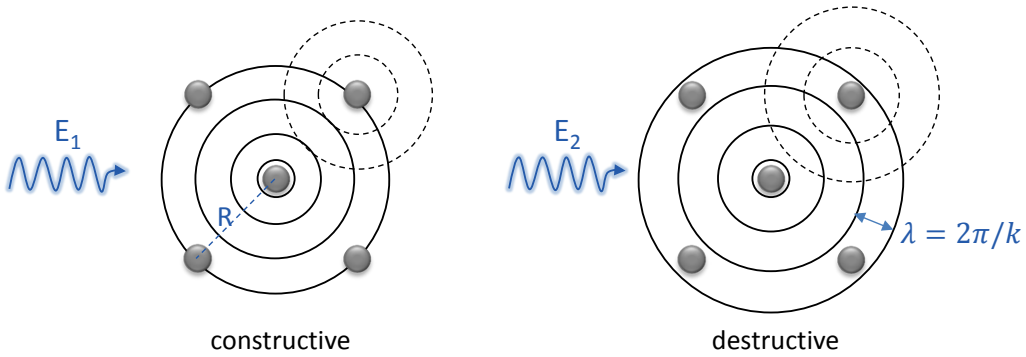

FIGURE 3.9: Schematic representation of the photoelectron wave. It represents the constructive and destructive interference of the outgoing and the backscattered waves. This phenomena gives rise to the oscillations in the absorption coefficient observed in Fig. 3.4.

given temperature, the atoms are vibrating around equilibrium positions, the effect of static and dynamic (thermal) disorder is considered by the Debye-Waller factor, σ^2, the mean square relative displacement. Thus, the model describing the EXAFS signal takes a relatively simple form, suitable for data refinement[140–142]:

$$k\chi(k) = S_0^2 \sum_j N_j f_j(k) \frac{e^{-2\sigma_j^2 k^2} e^{-2R_j/\lambda(k)}}{R_j^2} sin[2kR_j + \phi_j(k)] \tag{3.4}$$

This expression contains structural and electronic parameters. The structural parameters enclose N_j, R_j and σ_j^2. On the other hand, electronic parameters include the backscattering amplitude of the j_{th} neighboring atom $f_j(k)$; the electronic phase shift $\phi(k)$; the scale factor S_0^2, related to many body effects; and $\lambda(k)$, the mean free-path that takes into account the inelastic losses of the photoelectron.

The backscattering amplitude, f_j, and the phase sift, ϕ_j, can be theoretically calculated using the FEFF code version 8.1[143,144], allow distinguishing the different elements around the absorbing atom. Thus, the EXAFS is essentially a process to obtain structural parameters: N_j, R_j and σ^2, using the theoretical backscattering parameters f_j and ϕ_j.

Since the EXAFS function is the sum of different frequencies corresponding to the different distances of each coordination shell, the Fourier transform of the EXAFS data, $\Phi(R)$, can be used to isolate a contribution of a particular j_{th} shell around the absorber.

Fig. 3.10 shows the EXAFS spectra and the modulus of the Fourier transform at the Fe *K*-edge obtained for Bfr and *M. gryphiswaldense* as a function of $\alpha_{Fe_3O_4}$. The EXAFS spectra extends up to k=12 Å^{-1}, for Bfr and the biomineralization samples from t=0-150 min, and up to k=14 Å^{-1}, for the samples obtained from t=210 to 1440 min, with high signal-to-noise ratio. Even when the whole k-range was used in the EXAFS-fitting, for a straightforward qualitatively comparison, the Fourier transform

$\Phi(R)$ presented in 3.10b was performed over the k range 2.3 Å$^{-1} \leq k \leq$ 12.0 Å^{-1}, using a Hanning window and a k^2 weighting factor to compensate the amplitude decay at high k values. It is worth noting that R values presented in $\Phi(R)$-graph do not correspond directly to interatomic distances due to the shift introduced by the backscattering phase $\phi_j(k)$ in equation 3.11.

EXAFS spectrum $\chi(k)$ and $\Phi(R)$ of Bfr are displayed in Fig 3.10. $\Phi(R)$ presents just two major peaks, the one at R=1.5 Å, corresponding to the oxygen coordination shell (Fe-O), and a second one at R=2.6 Å related to the nearest iron atoms with octahedral symmetry (Fe-Fe). No further peaks are detected at higher distances, a sign of lack of long range order on the sample.

Biomineralization samples have been added in 3.10. EXAFS spectra evolve as $\alpha_{Fe_3O_4}$ increases. The observed tendency reflects the structural changes which take place along the process (see gray arrows in Fig. 3.10a). As already observed by XANES, the sample evolves from a Bfr-like spectrum to magnetite.

$\Phi(R)$ displayed in Fig. 3.10b presents two main features: one peak around R=1.5 Å, corresponding to the first oxygen coordination shell around the absorbing atom (Fe-O) and two further peaks between 2 and 3.5 Å mainly related to the nearest iron neighbors located in octahedral and tetrahedral sites, Fe_{Oh}-Fe_{Oh} ($\sim$ 2.5 Å) and Fe_{Th}-Fe_{Oh} ($\sim$ 3.1 Å), respectively. As the process evolves, the first Fe-O peak becomes less intense due to the increasing tetrahedral occupancy already observed by XANES in the pre-peak region. The scattering with the oxygen nearest neighbors is higher in octahedral sites (6 oxygen neighbors) than in tetrahedral ones (4 oxygen neighbors)[145]. On the contrary, the intensity of the Fe-Fe peaks increases with the elapse of time, particularly for Fe_{Th}-Fe_{Oh} peak due to the increasing tetrahedral occupancy of Fe ions as the process goes on.

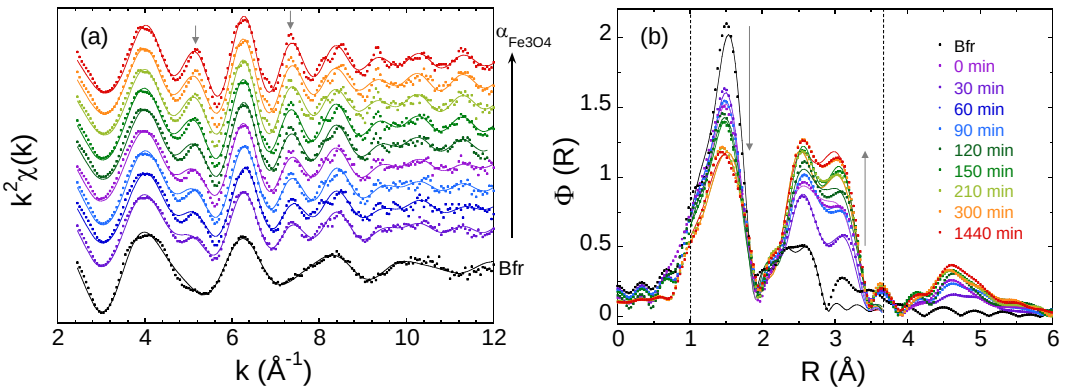

FIGURE 3.10: (a) EXAFS spectra at the Fe K-edge of Bfr and samples at the specific times after the iron incubation. (b) Fourier transform of $\chi(k)$ carried out over 2.3 Å$^{-1} \leq k \leq$ 12.0 Å^{-1}, using a k^2 weighting factor. Grey arrows emphasize the changing regions. The corresponding fits to the experimental data (continuous lines) are also plotted in both $k-$ and $R-$ spaces.

To acquire quantitative information about the local structure around the Fe atoms, the Fourier transform of the main peaks (1.0 Å^{-1} $\leq k \leq$ 3.66 Å^{-1}) was fitted to the EXAFS function (Equation 3.11). The fitting procedure consists on the minimization of the difference between the experimental data $\chi_{exp}(k)$ and the model function χ_{th}:

$$S^2 = \frac{\sum_{i=1}[k_i^2\chi_{exp}^F(k_i) - k_i^2\chi_{th}(k_i)]^2}{\sum_{i=1}^N[k_i^2\chi_{exp}^F(k_i)]^2} \tag{3.5}$$

As a first approximation, we have used a two-shell model for the Bfr, one for Fe-O and one Fe-Fe, but the fit improves with an additional Fe-P coordination shell, as suggested by XANES spectroscopy.

For the fitting of biomineralization samples, we initially considered a four-shell model, 4 different paths corresponding to Fe_{Th}-O (1.89 Å), Fe_{Oh}-O (2.02 Å), Fe_{Oh}-Fe_{Oh} (2.98 Å) and Fe_{Th}-Fe_{Oh} (3.48 Å). However, coordination shells differing less than $\pi/2\Delta k$ ($\Delta R \leq \pi/2\Delta k$) are hardly distinguished by EXAFS. Since the difference between Fe_{Th}-O and Fe_{Oh}-O coordination shells (ΔR=0.13Å) are within the resolution limit defined by the employed k-range, either $\Delta R \geq$ 0.16 Å (2.3 Å^{-1} $\leq k \leq$ 12.0 Å^{-1}) or 0.13 Å (2.3 Å^{-1} $\leq k \leq$ 14.0 Å^{-1}), just three paths could be distinguished: Fe-O at an average value of 1.99 Å, Fe_{Oh}-Fe_{Oh} (2.98 Å) and Fe_{Th}-Fe_{Oh} (3.48 Å). For the earlier stages of the biomineralization process, from t=0-150 min, the fit improves with an additional Fe-P coordination shell, as also occurs with Bfr.

EXAFS-fits were implemented with the ifeffit and Artemis softwares[146,147]. The overall scale factor, S_0^2=0.91 was determined by fitting t=1440 min sample, which corresponds to inorganic magnetite (see Fig. 3.5). For the fitting of $\Phi(R)$ (t=1440 min), the coordination numbers were fixed to the crystallographic ones of magnetite on the basis that EXAFS averages over all the Fe atoms in magnetite. Thus, we considered that only two-thirds of the Fe atoms occupy octahedral sites (coordination 6) and the remaining one-third occupies the tetrahedral ones (coordination 4) (see Fig. 1.5)[145].

The quality of the fits can be checked in Fig. 3.10 in both $k-$ and $R-$ spaces. The interatomic distances, R, and coordination numbers, N, obtained for each shell at the different times of the biomineralization process are displayed in Fig. 3.11 as function of $\alpha_{Fe_3O_4}$. Due to the strong correlation between the fit parameters, the Debye-Waller factors, σ^2, were restricted to physical values ($\sigma \in$(0.0075 Å^2-0.0100 Å^2)).

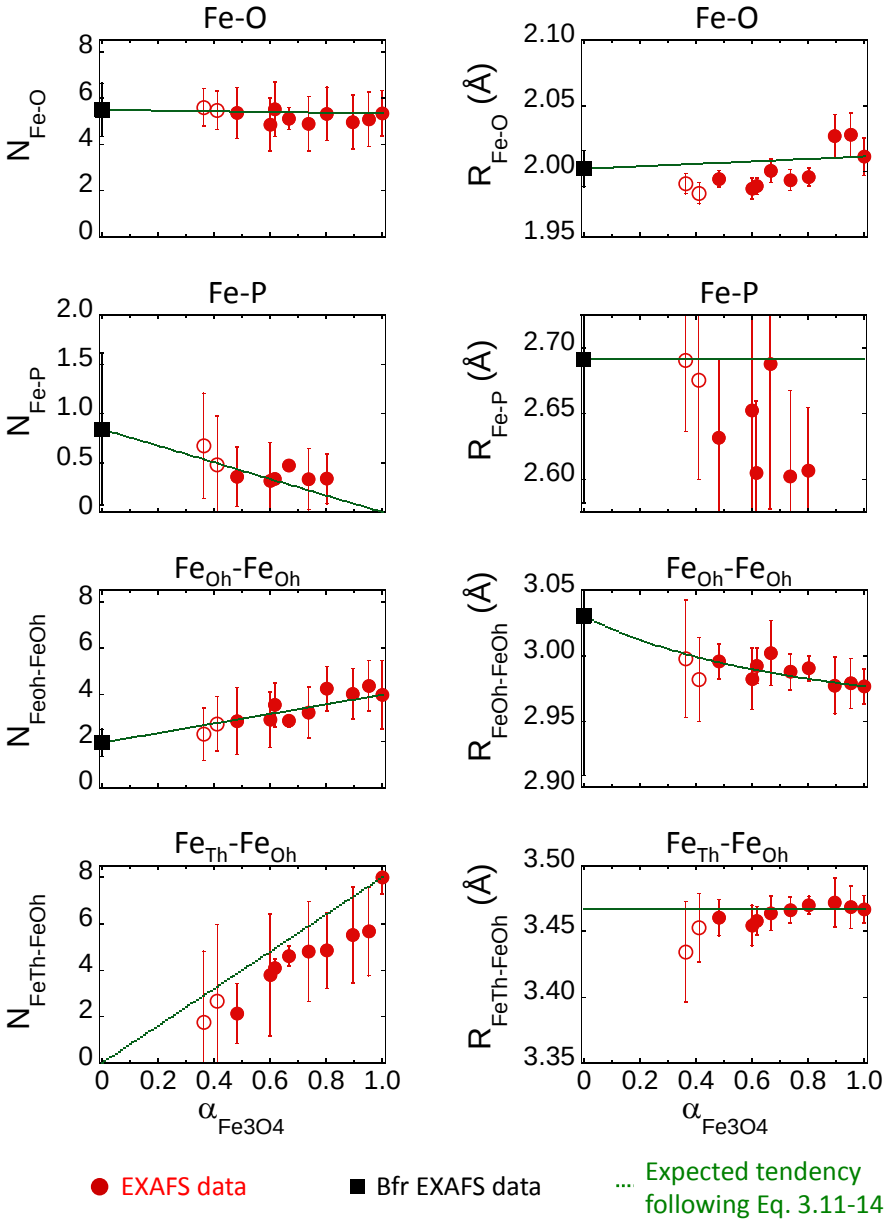

FIGURE 3.11: Coordination number, N, (left) and interatomic distance, R, (right) evolution as function of the atomic fraction of magnetite ($\alpha_{Fe_3O_4}$) for each individual path (red dots). Empty dots represent the values obtained for the complementary biomineralization samples. The EXAFS-fit values of Bfr (black squares) have been added at $\alpha_{Fe_3O_4}$=0. Green dashed lines display the tendency expected considering the coexistence of Bfr and magnetite (equations 3.6-3.9).

Aiming to further evaluate the coexistence of the two phases evidenced by XANES, we analyzed each individual path. From the atomic fraction, extracted by XANES, and the coordination numbers and average interatomic distances of Bfr and magnetite, we derive the tendency of the structural parameters (N and R) as a function of $\alpha_{Fe_3O_4}$. For that, we firstly take into account that the coordination shells which

involve Fe_{Th} belong exclusively to magnetite while the Fe-P coordination shell is proper of the Bfr phase. Thus, the coordination numbers are expected to evolve as follows:

Fe-P:

$$N^{Fe-P} = N^{Fe-P}_{Bfr} \cdot (1 - \alpha_{Fe_3O_4}) \tag{3.6}$$

Fe_{Oh}-Fe_{Th}:

$$N^{Fe_{Oh}-Fe_{Th}} = N^{Fe_{Oh}-Fe_{Th}}_{Fe_3O_4} \cdot \alpha_{Fe_3O_4} \tag{3.7}$$

The interatomic distances of the paths exclusive to Bfr and magnetite should remain constant regardless of the atomic fraction.

On the other hand, the tendency of the Fe-O and Fe_{Oh}-Fe_{Oh} paths involved in both phases, magnetite and Bfr, should follow:

$$N^{Fe-O} = N^{Fe-O}_{Fe_3O_4} \cdot \alpha_{Fe_3O_4} + N^{Fe-O}_{Bfr} \cdot (1 - \alpha_{Fe_3O_4}) \tag{3.8}$$

and,

$$R^{Fe-O} = \frac{N^{Fe-O}_{Fe_3O_4} \cdot R^{Fe-O}_{Fe_3O_4} \cdot \alpha_{Fe_3O_4} + N^{Fe-O}_{Bfr} \cdot R^{Fe-O}_{Bfr} \cdot (1 - \alpha_{Fe_3O_4})}{N^{Fe-O}_{Fe_3O_4} \alpha_{Fe_3O_4} + N^{Fe-O}_{Bfr} (1 - \alpha_{Fe_3O_4})} \tag{3.9}$$

with equivalent expressions for $N^{Fe_{Oh}-Fe_{Oh}}$ and $R^{Fe_{Oh}-Fe_{Oh}}$.

The expected tendencies obtained according to equations 3.6-3.9 are plotted in Fig. 3.11. The good match, within the error, between the expected evolutions and the EXAFS data confirms that the two phases, Bfr and magnetite, coexist in the whole biomineralization process. The presence of intermediate phases are not evidenced.

3.5 High resolution TEM (HRTEM)

XANES and EXAFS results evidence the coexistence of two phases: Bfr and magnetite. These techniques provide average information about the whole analyzed sample, being interesting to carry out a complementary analysis on specific areas of the bacteria. High resolution transmission electron microscopy (HRTEM) provides a precise spatial resolution of the different phases involved in the biomineralization process by means of electron diffraction. Thus, *E. coli* overexpressing Bfr and *M. gryphiswaldense* cells at t=60 min after Fe incubation were analyzed. According to the previous results, 60 min after iron incubation, *M. gryphiswaldense* cells still present a high atomic percentage of Bfr coexisting with magnetite ($\alpha_{Fe_3O_4}$=0.6). Since the magnetite biomineralization is initiated at multiple discrete sites distributed along the

cell, at this specific time we find particles at different stages of the biomineralization process that can be analyzed separately. Ultrathin sections of polymerized cells were studied. Details about sample preparation can be found in in page 75 of *Materials and Methods* section.

Fig. 3.12 shows HRTEM image of Bfr together with the Fourier transform of the marked core. In this sample, several particles show one or two sets of well-defined lattice fringes. As we have previously reported in García Prieto et al.[119], the Fourier transform of the selected areas reveals two systems of fringes at ∼2.9 Å (majority) and ∼2.6 Å (minority).

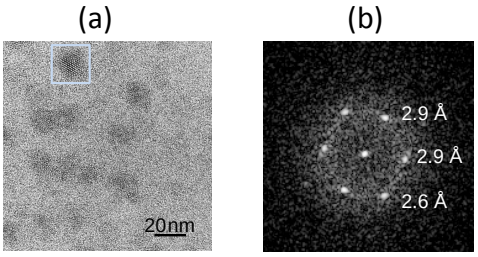

FIGURE 3.12: (a) HRTEM image of *E. coli* overexpressing bacterioferrtin (Bfr) and (b) Fourier transform of highlighted nanoparticle.

Fig. 3.13 displays HRTEM images obtained from different regions of the ultrathin section of *M. gryphiswaldense* cells harvested 60 min after the iron incubation. The earlier stages of the biomineralization process are presented in panel 1. These images evidence the presence of small nanoparticles of 3-4 nm in the cellular cytoplasm. Their Fourier transforms reveal patterns with diffuse intensity with a mean lattice spacing of $\sim$ 2.9 Å and $\sim$ 2.6 Å[119]. Both, the particle size and the system of fringes are coincident to the observed ones in Bfr. The diffuse patterns may suggest a more disordered phase than Bfr. This difference could be attributed to the comparison of protein of different species, *E. coli* and *M. gryphiswaldense*. Slight variations in protein coming from different specie could exist as a consequence of minor changes in the amino-acid sequence. Furthermore, the crystallinity of the iron mineral cores could be altered as a consequence of a different phosphorous content. This fact supports the idea that Fe is stored as a compound inside the cytoplasm before being introduced into the magnetosomes[106]. Nevertheless, it is worth noting that the observation of the lattice spacing $\sim$ 2.9 Å and $\sim$ 2.6 Å does not guarantee unequivocally the presence of Bfr. As observed further on, these lattice spacings often appear in different zone axis of magnetite. However, in the case of magnetite we would expect the presence of more spots in the Fourier transform.

The right image on panel 1 (Fig.3.13) displays a section of the magnetosome chain constituted by 4 well-formed magnetosomes (35-45 nm). On the bottom part of this chain a white circle is observed. This "hole" with the proper size (45 nm) is probably an empty magnetosome vesicle, which belong to a different bacterium, cut across

in the ultrathin analyzed sample. It is well-known that fully-formed magnetosome vesicles exist even in the absence of magnetite crystal[21,71]. Thus, it may be either a vesicle prior to the magnetosome formation or a vesicle which empties in the cutting process pulling out the allocated magnetosome. In this image, similar nanoparticles of 3-4 nm are located in the peripheries of this hypothetical empty vesicle forming a corona.This statement agrees with the high content of iron present close to the magnetosome membrane previous to the magnetosome formation, recently reported by Weckmann et al[148].

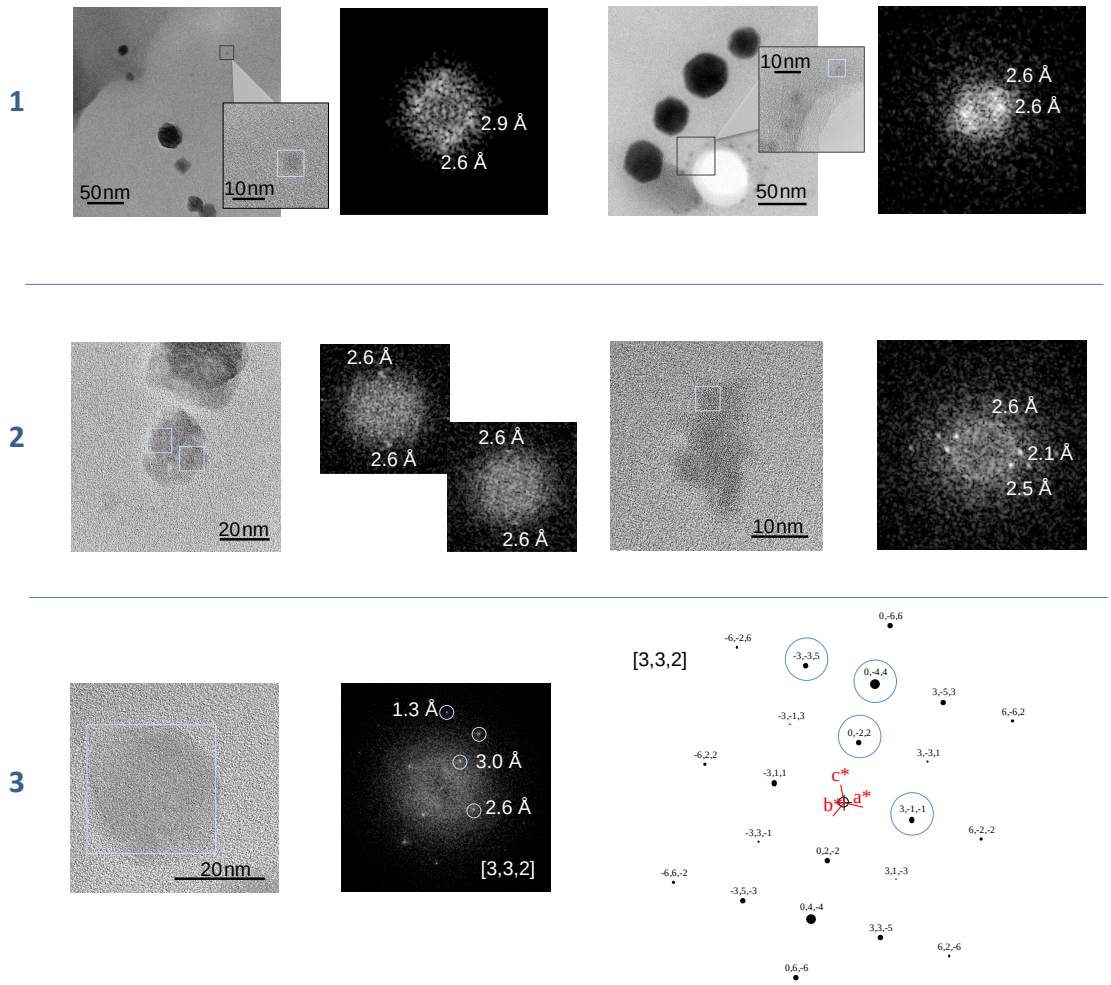

FIGURE 3.13: HRTEM images and Fourier transform of selected regions of ultrathin sections of *M. gryphiswaldense* at t=60 min (panel 1-3). Panel 3 presents the theoretical diffraction patterns for the magnetite, zone axis [3,3,2]. Blue circles highlight the spots identified in the FT.

Bigger particles are observed at more advanced stages (panel 2 in Fig. 3.13). Particles of tens of nanometers present irregular morphology. Indeed, we can distinguish clusters of smaller particles ranging from 5 to 10 nm. These sub-particles evidences lattice spacing ranging from $\sim$ 2.1 Å to $\sim$ 2.6 Å, which are slightly smaller

than the expected for Bfr. The decrease on the lattice spacing could suggest the presence of nanomineral ferrihydrite with a smaller content of phosphate than Bfr, as previously reported by the group[119]. On the other hand, the parallelism of lattice fringes proves that the crystallographic axes of these particles are parallel, interpreting these regions as aggregates of particles with the same three-dimensional (3D) orientation.

Similar aggregates have been observed in chemical preparation of magnetite nanoparticles in solution, where magnetite nucleates and grows from nanometric ferrihydrite-like aggregates[149]. Furthermore, it is said that phosphate may inhibit the formation of iron oxides including magnetite[150]. This fact could explain the phosphorous reduction suggested by HRTEM.

Finally, we have analyzed a bigger particle of 28 nm. The Fourier transform presented in panel 3 of Fig. 3.13 already reveals a magnetite phase. The crystal structure has been determined from the indexation of the spots which yields a magnetite structure oriented in the [3,3,2] zone axis. It is worth to highlight this zone axis presents a lattice spacing of ~ 2.6 Å.

HRTEM and electron diffraction prove again the coexistence of Bfr-like and magnetite along the biomineralization process. The presence of aggregates of small particles with the same 3D-orientation and smaller lattice spacing could suggest the existence of a ferrihydrite-like phase poorer in phosphorous, non detected by XAFS probably due to a low content and the similitude with Bfr. No evidence of any other phases was found.

3.6 Electron Energy Loss Spectroscopy (EELS)

Aiming to further investigate the different biomineralization stages in individual particles belonging to the same chain, we carried out energy loss spectroscopy (EELS). Thus, we have proved the oxidation state of iron in magnetosomes of different sizes by means of EELS. This spectroscopic technique measures the energy distribution of electrons that have interacted with the sample and lost energy as a consequence of the inelastic scattering. When the transferred energy is above the edge threshold, core electrons are promoted to a higher energy state giving rise to core-loss excitations. Because each ionization edge occurs at an energy loss that is characteristic of a particular element, EELS can be used to identify the elements and their oxidation state. Furthermore, combined with transmission imaging, it also provides spatial resolution. Thus, we have analyzed the Fe $L_{2,3}$-edge ($2p^6 3d^n \longrightarrow 2p^5 3d^{n+1}$ transitions) of individual magnetosomes at different stages of their biomineralization process within the cell. EELS measurements were carried out on Nanogune in collaboration with Dr. Andry Chuvilin. Details of sample preparation and EELS-conditions can be found in *Materials and Methods* section (page 76).

Fig. 3.14a displays the image of a *M. gryphiswaldense* bacterium 60 min after the iron incubation. As previously mentioned in the TEM section, at this biomineralization time, primitive chains constituted by small particles start to be observed. We have selected three particles of different sizes to analyze the oxidation state as the magnetosomes are formed. The first and smaller particle, (1), presents an irregular and diffuse shape with a mean diameter of 11 nm. According to what we have seen so far, we expect that this magnetosome is at the beginning of the biomineralization process. On the other hand, (2) and (3) are bigger (24 nm) and display a more homogeneous shape compared to the first one.

The spectra of the analyzed magnetosomes have been compared with three well-known standard samples: FeO (Fe^{2+}), Fe_2O_3 (Fe^{3+}) and a well-formed magnetosome of 45 nm measured at t=1440 min (pure magnetite: ($Fe^{2+,3+}$)). The Fe $L_{2,3}$-edges spectra of the standards display two characteristic white-lines, Fe L_3 and Fe L_2 (see Fig. 3.14b). Note that for divalent iron (FeO), the Fe L_3 white-line is dominated by a sharp peak at $\sim$ 707.5 eV, followed by a broader and less intense shoulder around 710 eV. On the other hand, the L_3-edge of Fe_2O_3 (trivalent ion) consists on a peak with its maximum at $\sim$ 708.9 eV, preceded by a less intense pre-peak at $\sim$ 707.5 eV. The EEL spectrum corresponding to a well-formed magnetosome of 45 nm measured at t=1440 mn (pure magnetite) presents an 'intermediate' shape, pointing out the coexistence of Fe^{2+} and Fe^{3+}. Remember that the relative concentration of Fe^{2+} and Fe^{3+} in magnetite is 1:2. Furthermore, the L_2-edge maximum is located around 11-12 eV above the L_3-edge maximum. The position of the maximum again seems to displace towards higher energy values as the predominant iron content changes from Fe^{2+} to Fe^{3+}.

As for Fe_2O_3 and 1440 min, magnetosomes measured at t=60 min display a mean peak at $\sim$ 708.9 eV, preceded by a less intense pre-peak at $\sim$ 707.5 eV. It suggests a valence states ranging from Fe^{3+} to $\frac{1}{3}Fe^{2+}$,$\frac{2}{3}Fe^{3+}$. Note that the three spectra obtained for the biomineralization samples are broader a nosier than the obtained for standards as consequence of the tiny size of the analyzed particles.

Aiming to obtain quantitative information about the oxidation state of the analyzed samples we have followed the method described by van Aken et al[151]. Basically, we have determined the integral Fe $L_{2,3}$-edge peak intensity ratios I(L_3)/I(L_2). For that, two integral windows of 2 eV width were applied to the $L_{2,3}$-edges. The first window includes the area enclosed from 707.9 eV to 709.9 eV, while the second one covers from 719.1 eV to 721.1 eV (see purple regions in Fig. 3.14b). Traditionally the way to obtain quantitative information about the Fe^{2+}/Fe^{3+} is calculating the total integral intensities of the L_3- and the L_2-white lines. However, the method presented here offers several advantages compared to the total integration. On the one hand, it leads to a more extended range of I(L_3)/I(L_2) values, which extends from about 2 (Fe^{2+}) to 9.5 (Fe^{3+}) compared to the intensity range delimited by 3.5 and 5.5 in the case of total integration. Furthermore, this method minimizes the influence of

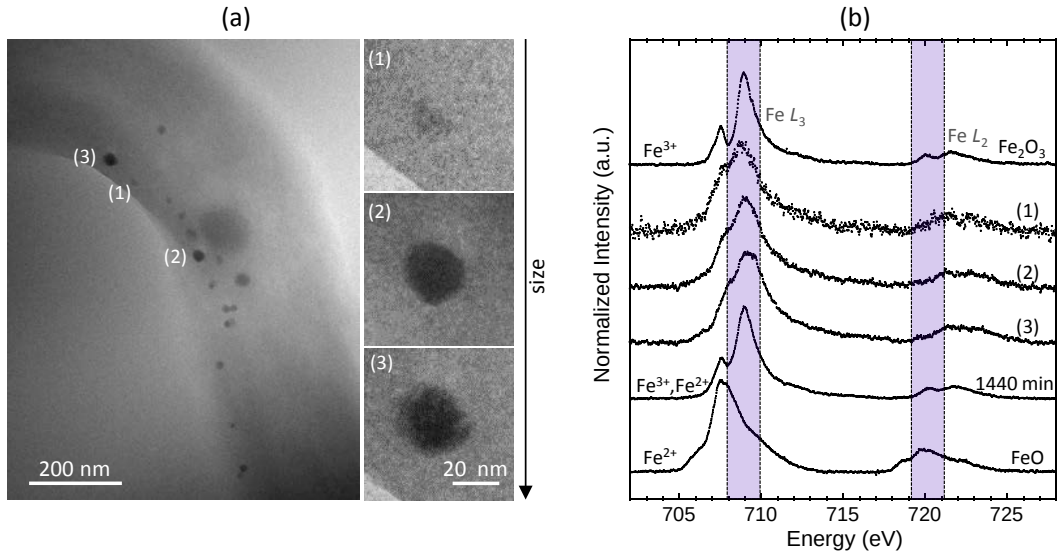

FIGURE 3.14: (a) TEM image of a *M. gryphiswaldense* cell at t=60 min after the iron incubation. Magnified images of the three analyzed magnetosomes, (1) size 11 nm and (2) and (3) of 24 nm, are presented on the right of the image. (b) Fe $L_{2,3}$-edge EEL spectra of the particles shown in (a) together with the spectra corresponding to a well-formed magnetosome at 1440 min and FeO (Fe^{2+}) and Fe_2O_3 (Fe^{3+}) standards. The data have been normalized to the maximum intensity of the L_3-edge. Spectra have been shifted vertically for clarity. Purple regions represent the two integrating windows of 2 eV width.

crystal field and multiple scattering effects[151].

Thus, following this method, we have calculated the integral peak intensity ratio I(L_3)/I(L_2) as summarized in table 3.1.

TABLE 3.1: Integral peak intensity ratio I(L_3)/I(L_2) obtained for the standard samples: FeO, 1440 min (Fe_3O_4) and Fe_2O_3; and the three analyzed magnetosomes presented in Fig. 3.14a. I(L_3)/I(L_2) was determined within the 10% of error.

Standard	I(L_3)/I(L_2)	$Fe^{3+}/\sum Fe$	Sample	I(L_3)/I(L_2)	$Fe^{3+}/\sum Fe$
FeO	2.7(3)	0	(1)	9.4(9)	1.0(3)
1440 min	7.7(8)	0.66	(2)	7.9(8)	0.7(1)
Fe_2O_3	9.2(9)	1.00	(3)	7.7(8)	0.7(1)

According to van Aken and coworkers, I(L_3)/I(L_2) as function of the Fe^{3+} iron concentration follows a second order hyperbolic function.

$$\frac{I(L_3)}{I(L_2)} = \frac{1}{a \cdot x^2 + b \cdot x + c} - 1 \tag{3.10}$$

By fitting the standard samples with this function, we have obtained a calibration curve the constants a=0.19(7), b=-0.36(4) and c=0.27(2). It allows us to determine the Fe^{3+} iron concentration, $Fe^{3+}/\sum Fe$, of the analyzed magnetosome samples (1), (2) and (3) presented in Fig. 3.14a. Thus, the obtained values are summarized in table

3.1 and in Fig. 3.15.

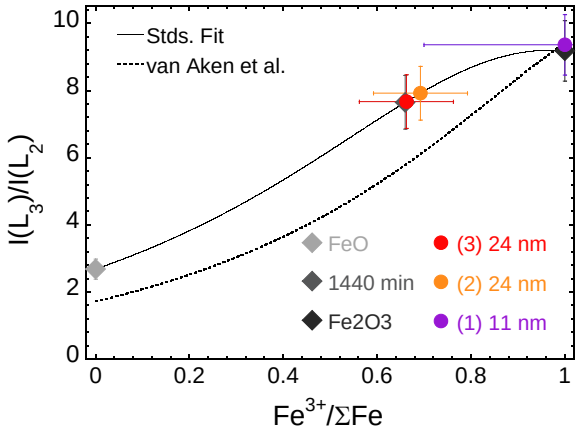

FIGURE 3.15: Integral peak intensity ratio I(L_3)/I(L_2) as function of the $Fe^{3+}/\sum Fe$ using two integrating windows 2 eV width. Grey rhombus point the I(L_3)/I(L_2) values obtained for the standards: FeO, 1440 min (Fe_3O_4) and Fe_2O_3. Color dots represents the three analyzed magnetosomes presented in Fig. 3.14a. The $Fe^{3+}/\sum Fe$ value of these data have been set according to the fit of standard samples. Continuous and dashed lines depict the second hyperbolic function-fit of the standard data and the curve reported by van Aken and co-workers[151] respectively.

Despite the large error of the analysis, a tendency is observed. The smaller and more irregular magnetosome, (1), with a mean size of 11 nm, matches with an Fe^{3+} compound, as expected for a ferrihydrite-like structure. This particle would correspond with the aggregates of nanoparticles presented in panel 2 of Fig. 3.13. As XANES analysis evidences, EELS supports the partial reduction from Fe^{3+} to Fe^{3+}, Fe^{2+} in a ratio 2:1 when the process evolves. This reduction seems to be a fast process, we are not able to distinguish intermediate phases. Particles as small as 24 nm already present an oxidation state similar to magnetite (magnetosomes (2) and (3)). These results agree with the HRTEM and electron diffraction findings and previous EELS results in *Magnetospirillum magneticum* strain AMB-1[152].

3.7 Proposal of biomineralization process

According to our findings by means of XANES, EXAFS, HRTEM and EELS and the results found in the bibliography, we propose the map presented in Fig. 3.16 for the biomineralization process:

i) A phosphate-rich ferric hydroxide phase with the spectroscopic signature of Bfr is formed in the cell cytoplasm. This phase is located around the magnetosome vesicle and plays the role of an iron source[148].

ii) The ionic iron provided by surrounding Bfr is transported into the magnetosome vesicle. Inside the vesicle, ferrihydrite-like precursor units, with a smaller phosphate content than Bfr, appear and aggregate via oriented attachment. Then,

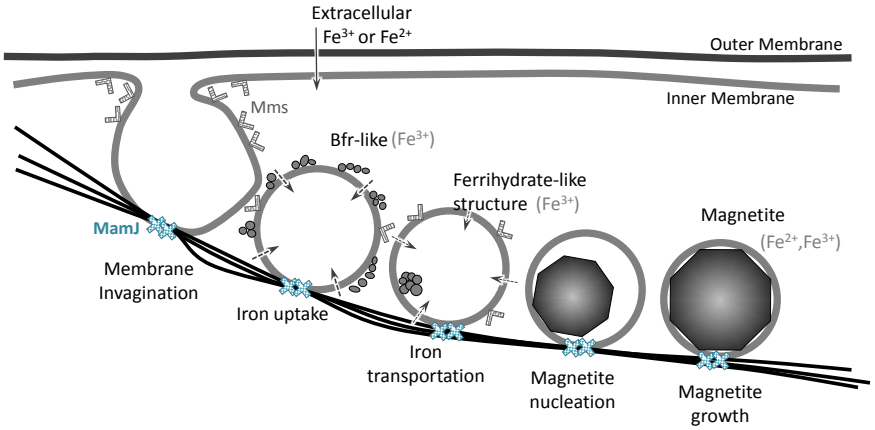

FIGURE 3.16: Schematic drawing of magnetosome biomineralization in *M. gryphiswaldense* bacterium according the presented results and bibliography. Modified from Arakaki et al[5].

the precursor is partially reduced to magnetite in a fast process.

iii) Finally, magnetite crystal grows into the magnetosome vesicle, which provides a confined space to guide the controlled growth into a crystal with genetically defined dimensions.

Materials and Methods

Light scattering measurements (C_{mag})

Light scattering measurements were performed with the experimental set-up shown in Fig. 3.17a. 1 mL of fixed *M. gryphiswaldense* cells suspended in the growth medium (10^8cell/mL) was poured into a cuvette at each biomineralization time. The optical density was measured at λ=565 nm in a spectrophotometer (Fig. 3.17a). A magnetic piece, conformed by two symmetric magnets, which give rise to an homogenous magnetic field ($\sim$ 20 mT), is placed either parallel or perpendicular to the light beam. Up to three measurements are carried out at each configuration. C_{mag} coefficient was calculated.

Transmission Electron Microscopy (TEM)

For the bacterioferritin imaging, *E. coli* cells were fixed overnight in 2% glutaraldehyde in 0.1 M Sörenson phosphate buffer and washed with isoosmolar phosphate/sucrose buffer. After repeating washing with distilled water, the sample were dehydrated through an aceton series and embedded in Epon Polarbed resin in beem capsules, which polymerized at 55°Cfor 48 h. Ultrathin sections were ontained using a Diatome diamond knife in Leica UCT ultramicrotome and deposited onto 300 mesh Holey Carbon Film. TEM images were obtained on a Philips CM120 electron microscope at an accelerating voltage of 120 kV.

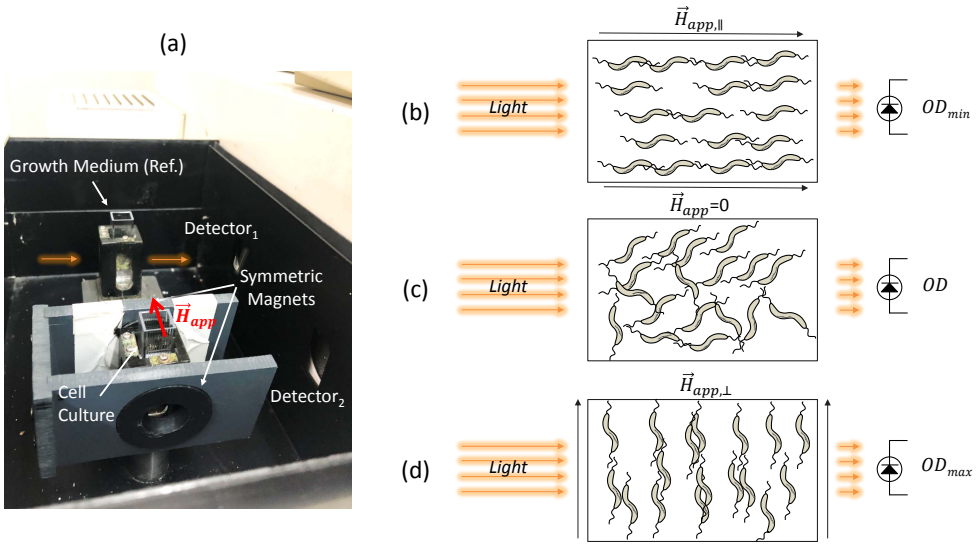

FIGURE 3.17: (a) Spectrophotometer and C_{mag} setup. According to magnet position in the image, magnetic field is applied perpendicular to the incoming light beam. Schematic representations of cell configuration: (b) parallel, (c) randomly and (d) perpendicular oriented to the incoming light beam.

On the other hand, TEM of *Magnetospirillum gryphiswaldense* at different stages of the biomineralization process was performed on unstained cells adsorbed onto 300 mesh carbon-coated copper grids. Images were obtained with a Philips CM120 electron microscope at an accelerating voltage of 100 kV.

X-ray absorption fine structure (XAFS)

In XAFS an x-ray beam hits the sample and photons are absorbed by the atom through the photoelectric effect. When E is equal or greater than the binding energy (E_0) of the core level electron, the x-ray photon is absorbed leading to a sharp increase of the absorption coefficient (μ), giving rise to the absorption edge.

$$I_t = I_0 \cdot e^{-\mu(E)t} \tag{3.11}$$

where I_t is the intensity transmitted through the sample, I_0 is the intensity of the incident x-ray and t is the thickness of the sample.

The created photoelectron propagates as a spherical wave with a wavelength given by the de Broglie relation. Its kinetic energy E_{kin} is then defined as:

$$E_{kin} = \hbar\omega - E_0 = \frac{p^2}{2m} = \frac{\hbar^2 k^2}{2m} \tag{3.12}$$

being $\hbar\omega = E$ the energy of the x-ray photon and E_0 the binding energy of the core-level electron, p the momentum of the photelectron, m the mass of the electron, $\hbar$ the Plank's constant divided by 2π and k the photoelectron wave vector. Thus, k

is defined as:

$$k = \sqrt{\frac{2m}{\hbar}(E - E_0)} = 0.512\sqrt{E - E_0} \tag{3.13}$$

where k is given in Å^{-1} and E and E_0 are expressed in eV.

Thus, according to the excess of energy acquired, the photoelectron may occupy a higher level of the atom or may reach the continuum states and propagate into the sample (see Fig. 3.18a). In condensed matter, the emitted photoelectron interacts strongly with the potentials of atoms surrounding the absorber. The scattering processes which take place give rise to fine structure oscillations that modulate the x-ray absorption coefficient (XAFS signal).

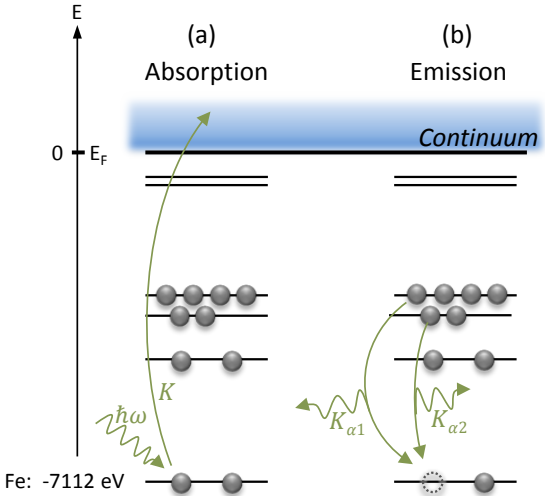

FIGURE 3.18: (a) Schematic representation of the x-ray absorption mechanism of an Fe 1*s* electron (*K*-edge). (b) Fluorescence emission mechanism is also presented.

The standard set up of a XAFS experiment is displayed in Fig. 3.19. The incoming x-rays arising from the synchrotron source pass to the optic hutch where the slits systems define the shape and size of the x-ray beam and the monochromator selects the exit beam energy. The intensity of the incident (I_0) and transmitted (I_t) x-rays through the sample are measured. For the subsequent energy calibration, a reference (Ref), in this case a Fe bcc foil, is placed after I_t and the transmitted intensity is recorded in a detector, I_r.

The transmission geometry presented in Fig. 3.19 ensures fast measurements with a high signal to noise ratio. However, in very diluted samples, such as the obtained at the first stages of the biomineralization process, where the Fe concentration is very low, this configuration presents some limitations. In these situations it is more convenient to measure μ(E) in an emission configuration, and particularly in fluorescence mode. Since after the absorption event the excited atom presents a core hole, a higher energy core level electron fills it by emitting an x-ray fluorescence ray

of well defined energy (Fig. 3.18b). In case of fluorescence mode $\mu(E)$ is estimated as the ratio between the fluorescence (I_f) and the incoming (I_0) intensity:

$$\mu(E) \propto \frac{I_f}{I_0} \tag{3.14}$$

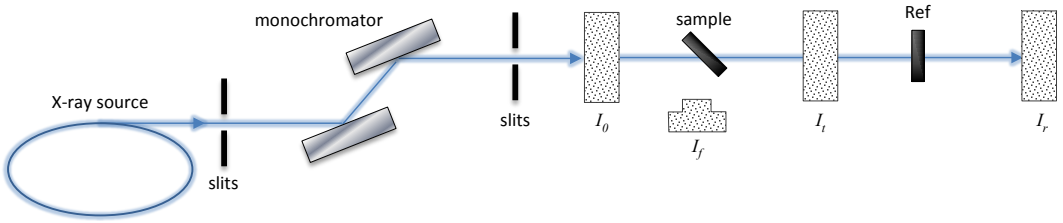

FIGURE 3.19: Standard set-up of XAFS beamline in transmission and fluorescence mode.

For the time-resolved structural analysis and Bfr, XAFS measurements were carried out on the whole cells. The sample was lyophilized and compacted into 5 mm diameter pills. XAFS experiment was performed at ESRF synchrotron facility (France) in the BM23 beamline. All the spectra were recorded at 60 K, with the storage ring working at a low intensity, $\sim$ 80 mA, in 16 bunch mode. The spectra were recorded simultaneously in transmission and fluorescence geometries with a solid state detector (13 elements) and using a double crystal Si(111) monochromator.

XAFS spectra of *M. gryphiswaldense* at specific times after Fe incubation were measured up to k=12 Å^{-1}, for samples belonging to t=0-150 min and Bfr, and up to k=14 Å^{-1}, for the samples obtained from t=210 to 1440 min. To improve the data reliability, between 5 and 8 spectra were recorded for each sample. Under these conditions, the edge position of the sample can be determined with an accuracy of 0.2 eV.

High resolution transmission electron microscopy (HRTEM)

E. coli and *M. gryphiswaldense* cells were fixed in 2% glutaraldehyde in 0.1 M Sörenson phosphate buffer and washed with isoosmolar phosphate/sucrose buffer. After repeated washing with distilled water, the samples were dehydrated through an acetone series and embedded in Epon Polarbed resin in beem capsules, which polymerized at 55 °C for 48 h. Ultrathin sections were obtained using a Diatome diamond knife in a Leica UCT ultramicrotome and deposited onto a 300 mesh Holey Carbon Film. HRTEM images of the samples at the selected biomineralization time and Bfr were obtained on a FEI TITAN^3 microscope at the Instituto de Nanociencia de Aragón (Spain), at a working voltage of 300 kV. The microscope is equipped with a SuperTwin objective lens and a CETCOR Cs-objective corrector from CEOS Company allowing a point to point resolution of 0.09 nm. Correction of the spherical aberration of the objective lens improves significatively the spatial resolution of the HRTEM images.

Electron Energy Loss Spectroscopy (EELS)

Measurements was performed on unstained *M. gryphiswaldense* cells collected at t=1440 min and 60 min after the Fe incubation, adsorbed onto 300 mesh carbon-coated copper grids. FeO and Fe_2O_3standard samples were also measured in powder as references of Fe^{2+} and Fe^{3+} compounds. The electron energy-loss spectra were obtained in a Titan 60-300 equipped with beam monochromator and Quantum GIF (965 model) imaging EELS spectrometer (from Gatan company). The spectra were acquiered at 80 kV accelerating voltage with monochromator on, in diffraction mode with acceptance angle of 2.8 mrad and dispersion of 0.025 eV/channel. Energy shift was achieved by applying drift tube potential of 690 V. Resolution achieved in these conditions was about 0.1eV measured as FWHM. For all the measured samples, the background was substracted by considering a spline function.

List of publications resulting from this Chapter

1. A. García-Prieto, J. Alonso, D. Muñoz, L. Marcano, A. Abad Díaz de Cerio, R. Fernández de Luis, I. Orue, O. Mathon, A. Muela, and M. L. Fdez-Gubieda, "On the mineral core of ferritin-like proteins: structural and magnetic characterization", *Nanoscale*, vol. 8, no. 2, pp. 1088-1099, 2016.

2. L. Marcano, A. García-Prieto, D. Muñoz, L. Fernández Barquín, I. Orue, J. Alonso, A. Muela, and M. Fdez-Gubieda, "Influence of the bacterial growth phase on the magnetic properties of magnetosomes synthesized by *Magnetospirillum gryphiswaldense*", *Biochimica et Biophysica Acta (BBA) - General Subjects*, vol. 1861, no. 6, pp. 1507-1514, 2017.

3. L. Marcano, A. García-Prieto, D. Muñoz, L. Fernández Barquín, I. Orue, J. Alonso, A. Muela, and M. Fdez-Gubieda, "The early stages of the biomineralization process of magnetosomes in *Magnetospirillum gryphiswaldense*", Under preparation.

Chapter 4

Transition metal doping of magnetosomes

4.1 Introduction

The high genetical control characteristic of the synthesis process yields to magnetic nanoparticles with specific composition, size and shape for a given bacterial strain[3,17]. However, being able to tune the properties of magnetosomes in the laboratory can be of great advantage for expand the applications.

In the last years, several groups have proposed different strategies, either focused on *in vivo* processes[38,53–55,153], or *in vitro* approaches[40,60,154,155], to tune the morphology, size and composition of the magnetosomes in order to overcome the natural limitations imposed by the genetic control of the magnetosome synthesis in different bacterial strains. One of the most promising approaches consists in modifying the composition of the magnetosomes by doping them with different elements. The substitution of iron cations by transition metal dopants in magnetite serves as a proven method to change the magnetic properties of the magnetic nanoparticles[156]. For example, regarding to biomedical applications, the incorporation of Co within the magnetite structure increases the coercivity and hence the hysteresis losses and the specific absorption rate (SAR) of the nanoparticles, which is directly related with the efficiency of nanoparticles in hyperthermia treatment[6,157,158].

Although reports addressing the possibility of doping magnetosomes with different metals dates from early 90's[159,160], the first laboratory-controlled doping of magnetosomes *in vivo* was performed on 2008 by Staniland et al.[53]. Since then, several groups have been able to dope magnetosomes with transition elements like Mn[54,153,161,162], Co[38,54,55,163] and Cu[54].

This Chapter reports the role of Mn, Co, Ni, Cu and Zn in the transition metal-doped magnetosomes chains synthesized by *Magnetospirillum gryphiswaldense* bacterium. With this aim, we make use of characterization techniques such as transmission electron microscopy (TEM), energy-dispersive x-ray spectroscopy (EDS) and

x-ray absorption near edge structure (XANES). These techniques evidence that out of the five tested metals, only manganese and cobalt were incorporated into magnetosome structure. DC magnetic measurements reveal that the incorporation of these elements introduces important changes in the magnetic behavior of magnetosomes. The presence of Mn notably reduced the magnetic coercivity. On the contrary, Co enhances the coercive field of magnetosomes and the remanent magnetization.

A deeper insight of the role of Co in the magnetic properties of Co-doped magnetosome chains is addressed at the last section of the Chapter. X-ray magnetic circular dichroism (XMCD) proves the presence of a single magnetic phase while verifies the cation distribution obtained by XANES. Furthermore, modeling of hysteresis loops with a modified Stoner-Wohlfarth approach sheds light on the different anisotropy contributions and their dependence on temperature for control magnetosomes and Co-doped magnetosome chains.

4.2 Magnetotactic bacteria cultures

4.2.1 Minimum Inhibitory Concentration (MIC) assays

Transition metal-doping was performed by replacing various quantities of iron citrate with the different M-citrates/sulfates into the growth media (M=Mn, Co, Ni, Cu and Zn). These elements are, to a greater or lesser degree, essential elements for life serving as micronutrients[164], being components of metalloproteins and metalloenzymes[165] or intervening in redox processes[166], among other roles[167]. Thereby, these elements are naturally acquired by the cell from the growth media mainly as inorganic ions. However, at too high concentration even essential metals becomes toxic and can adversely affect the cellular physiology resulting in growth inhibition or, in the extreme case, in cell death[166,167]. Thus, optimizing the metal concentration in the culture media is a key point to ensure the bacterial growth and magnetosome formation. With that aim, we have determined experimentally the critical concentration where cellular damage is detected by loss of cell viability in minimum inhibitory concentration (MIC) assays. Experimental details of MIC assays are reported in page 102 at *Materials and Methods* section.

Figure 4.1 displays the optical density as a function of the increasing metal ion concentrations, MIC profiles, of magnetotactic bacterium *M. gryphiswaldense*. Two alternative scenarios have been tested considering two different growth media to which the increasing metal concentration had been added. The first one, labelled as *FSM*, consists in flask standard medium[63] enriched with 100 μM of Fe^{3+}; while the second one, *LIM*, represents a Low Iron Medium, similar to the previous one in the absence of additional iron.

In presence of iron (FSM curves), MIC profiles evidence cell growths negatively affected by the increased concentrations of transition metals except for Mn^{2+}, which

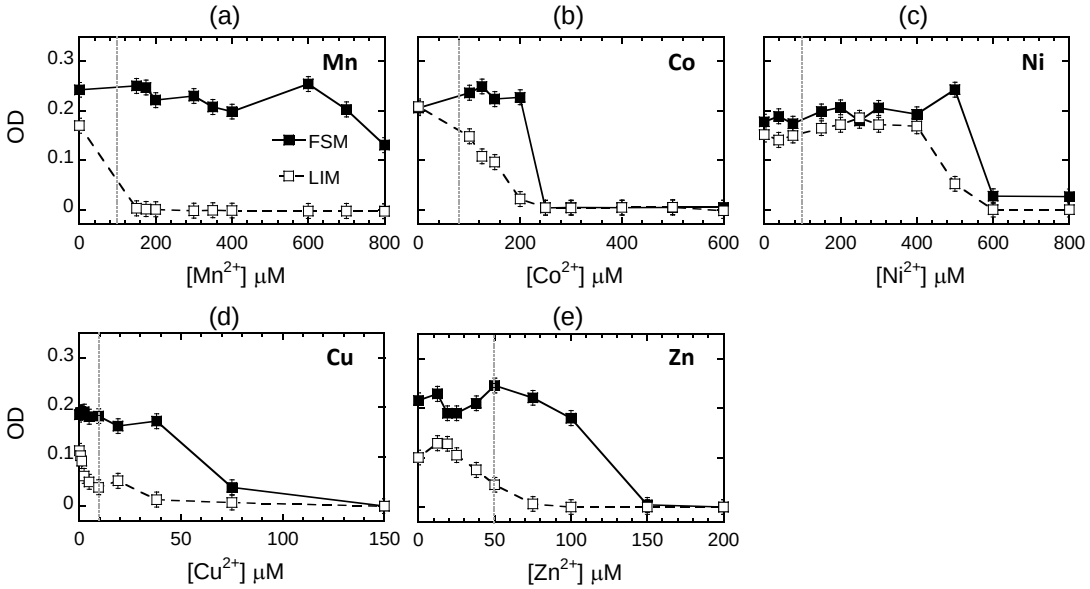

FIGURE 4.1: Optical density (OD) measured at 565 nm as a function of (from (a) to (e)) Mn^{2+}, Co^{2+}, Ni^{2+}, Cu^{2+} and Zn^{2+} concentrations either in addition of 100 μM of Fe^{3+}, FSM (■, continuous line) or in absence of iron, LIM (□ , dashed line). Error bars shows SDs. Grey lines correspond to the concentration chosen for each metal.

seems to be harmless for the strain in the whole range of concentrations. For Co^{2+}, Ni^{2+}, Cu^{2+} and Zn^{2+} cell growth decreases steeply at [Co^{2+}]=200 μM, [Ni^{2+}]=500 μM, [Cu^{2+}]=40 μM and [Zn^{2+}]=75 μM, evidencing a dramatic decrease of growth tolerance and even a completely inhibition at too high concentrations. Thus, in order to ensure the bacterial growth in presence of the different transition metals without exceeding the iron concentration employed thus far for the culture of control magnetosomes, we have chosen the following metal concentrations: [Mn^{2+}]=100 μM, [Ni^{2+}]=100 μM, [Ni^{2+}]=100 μM,[Cu^{2+}]=10 μM and [Zn^{2+}]=50 μM, marked with dashed grey lines in Fig. 4.1.

In the case of using LIM, the growth inhibition is clearly magnified (see Fig 4.1). It suggests that magnetosomes operate like detoxifiers of transition metal ions[17]. The absence of iron impedes the magnetosomes formation, withstanding significantly lower concentrations of those metals.

On the other hand, it is well known that microorganisms exposed to hostile environments develop a variety of resistance to deal with the existing challenges and adapt[166,167]. Inspired by this fact, we reduced the iron concentration to lead bacteria to their stress zone. To this end and aim at continuing ensuring cell-viability, we have fixed the metal concentrations to those ones stated above and have carried out MIC assays varying the Fe concentration from 0 to 150 μM (see Fig. 4.2). Based on these findings, we have observed that the metal tolerance drops when the concentration of iron falls below 10 μM, considering that the optimum concentration to carry out the metal doping of magnetosomes.

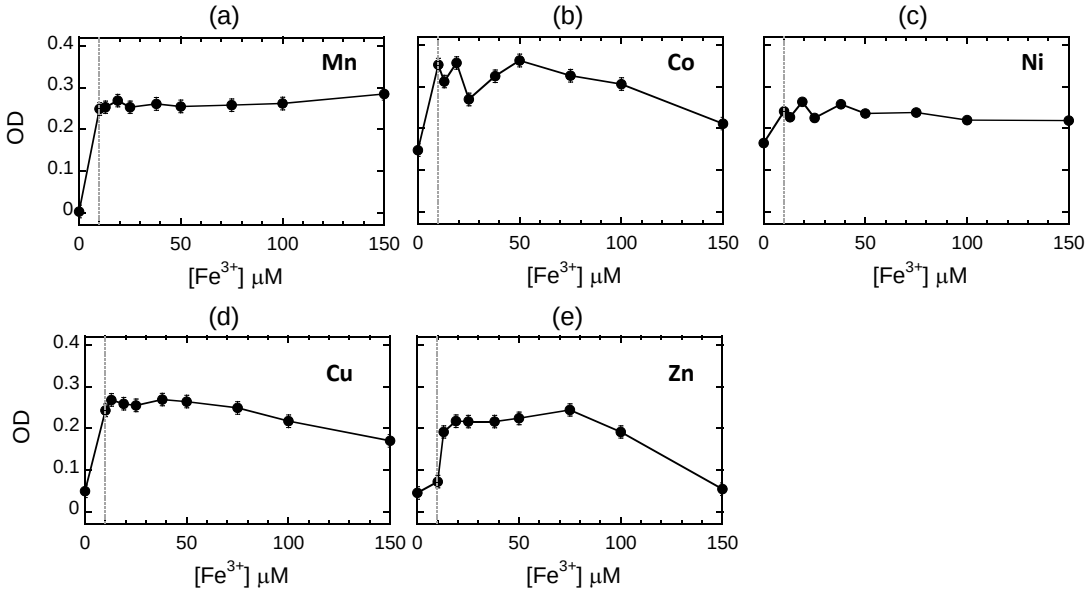

FIGURE 4.2: Optical density (OD) measured at 565 nm as a function of Fe^{3+} concentration for set metal concentrations: (a) $[Mn^{2+}]$=100 μM, (b) $[Co^{2+}]$=100 μM, (c) $[Ni^{2+}]$=100 μM, (d) $[Cu^{2+}]$=10 μM and (e) $[Zn^{2+}]$=50 μM. Error bars shows SDs. Grey lines correspond to the concentration chosen for each metal.

In summary, the metal concentrations considered for the sample preparation are set out in Table 4.1.

TABLE 4.1: Metal concentration values [μM] added to the growth media derived from MIC assays presented in Fig.4.1 and 4.2

Sample	$[Mn^{2+}]$	$[Fe^{3+}]$	$[Co^{2+}]$	$[Ni^{2+}]$	$[Cu^{2+}]$	$[Zn^{2+}]$
Control	-	100	-	-	-	-
Mn-doped	100	10	-	-	-	-
Co-doped	-	10	100	-	-	-
Ni-doped	-	10	-	100	-	-
Cu-doped	-	10	-	-	10	-
Zn-doped	-	10	-	-	-	50

4.2.2 Growth Conditions

Magnetospirillum gryphiswaldense was cultured in the iron rich medium (10 μ M) supplemented with the different metal concentrations according to Table 4.1. The ion concentration of the prepared growth media were checked by inductively coupled plasma atomic emission spectroscopy (ICP-AES). This technique is one of the principal methods used for the detection of chemical elements, providing multi-element analysis, monitoring up to 50 elements simultaneously, over a wide range of operating concentrations, covering minor- and trace-elements with a resolution up to 1

μM.

Table 4.2 shows the ion metal concentrations available in the prepared growth media obtained by ICP-AES. Each value has been calculated by averaging the results measured three times at every of the three studied wavelengths for each element. These values largely agree with the values set by MIC assays (see Table 4.1). The observed discrepancies could be attributed to experimental error and/or the presence of traces of transition metals in some of the components of the growth media. This last point explains the presence of low contents of Zn even when they have not been explicitly added.

TABLE 4.2: Metal concentration values [μM] registered in the growth media by ICP-AES. The numbers in parentheses indicate the error of measurement.

Sample	$[Mn^{2+}]$	$[Fe^{3+}]$	$[Co^{2+}]$	$[Ni^{2+}]$	$[Cu^{2+}]$	$[Zn^{2+}]$
Control	-	113(1)	-	-	-	4.0(3)
Mn-doped	125(3)	17.0(4)	-	-	-	3.5(4)
Co-doped	-	17.0(4)	112.8(7)	-	-	2.5(2)
Ni-doped	-	15.9(7)	-	140(3)	-	3.2(4)
Cu-doped	-	13.3(3)	-	-	6.0(4)	2.3(2)
Zn-doped	-	17.2(5)	-	-	-	72(2)

Cultures were carried out in three-fourths 1L-bottles, loosely capped at 28 °C without shaking using a magnetic inoculum, with cells at early stationary phase. Cells were cultivated for 120 h to assure the presence of well-formed magnetosomes.

4.3 Structural Characterization

4.3.1 Transmission Electron Microscopy (TEM)

Electron microscopy was performed on unstained cells adsorbed onto 300 mesh carbon-coated copper grids. TEM images were obtained with a JEOL JEM-1400 Plus electron microscope at an accelerating voltage of 120 kV. The particle size distribution was analyzed using a standard software for digital electron microscope image processing, ImageJ[125].

Fig. 4.3 displays representative TEM images and size distributions of control magnetosomes and M-doped magnetosome chains. In all conditions, TEM-micrographs evidence a comparable cell-morphology and the presence of a single magnetosomes chain.

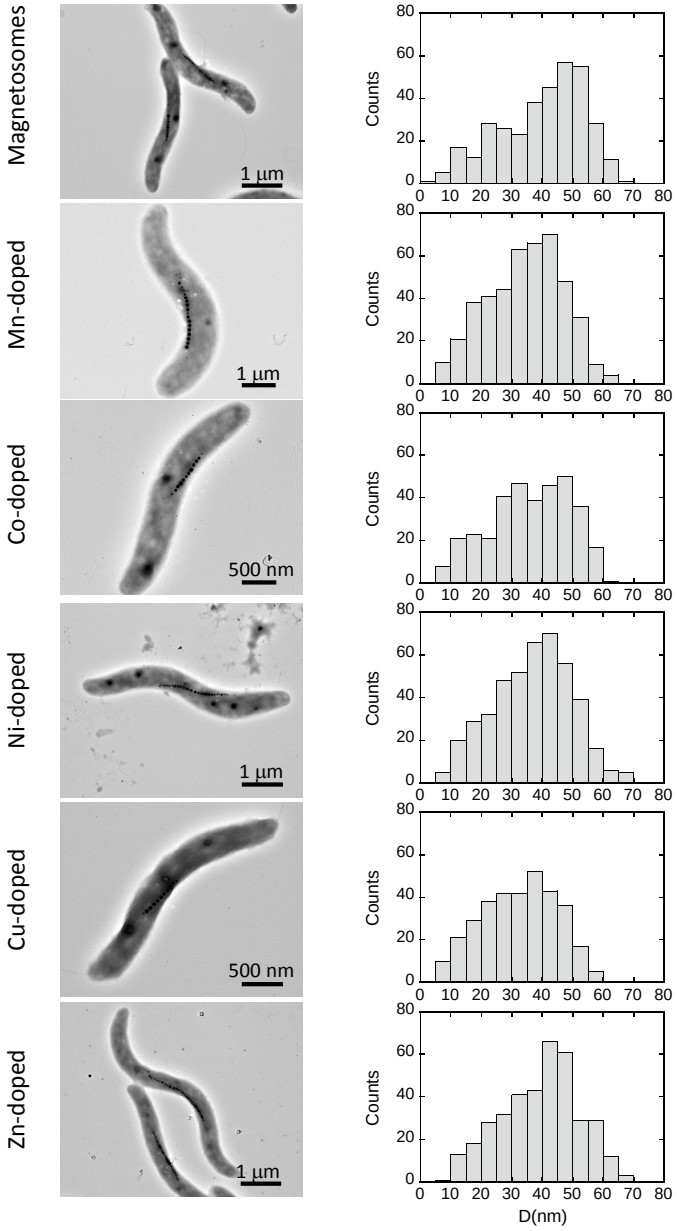

FIGURE 4.3: Representative TEM images and size distributions for control and M-doped magnetosomes. Statistic analysis have been performed considering population of magnetosomes higher than 300.

Regarding the magnetosome size distribution, control bacteria present uniformly sized magnetosomes except for those located at both ends of the chains, which are slightly smaller. This double size distribution is reflected in the histogram where one of the distributions is centered at $\langle D \rangle = 47$ nm with a standard deviation $\sigma = 8$ nm, with a majority of magnetosomes, while that corresponding to a lower fraction of magnetosomes is centered at $\langle D \rangle = 22$ nm ($\sigma = 8$ nm).

Mn and Co-doped magnetosomes do also present the double size-distribution,

but it is slightly shifted to lower values compared to the control magnetosomes. For Mn-doped magnetosomes, the size distributions peak in $\langle D \rangle = 39$ nm ($\sigma = 10$ nm) and $\langle D \rangle = 18$ nm ($\sigma = 6$ nm), respectively, while Co-doped magnetosomes distributions are centered in $\langle D \rangle = 40$ nm ($\sigma = 10$ nm) and $\langle D \rangle = 15$ nm ($\sigma = 6$ nm).

For the rest of metals (Ni, Cu and Zn), this double distribution is not as clear as before. In these cases, particle distribution behaves like a single distribution centered at $\langle D \rangle = 37$ nm ($\sigma = 13$ nm) for Ni-doped bacteria, at $\langle D \rangle = 33$ nm ($\sigma = 12$ nm) for Cu-doped bacteria, at $\langle D \rangle = 39$ nm ($\sigma = 13$ nm) for Zn-doped bacteria.

On the other hand, the number of magnetosomes per cell depends on the growth conditions and might vary[168]. Thus, Fig.4.4 compares the number of magnetosomes per chain in the different samples. It is worth noting the presence of short chains formed by just two or three magnetosomes in M-doped magnetosomes compared to control magnetosomes, where all chains are over 10 magnetosomes (see vertical lines displayed in Fig.4.4). Nevertheless, the average number of magnetosomes belongs to the range 15-25 in M-doped magnetosomes, comparable to the length observed in control magnetosomes.

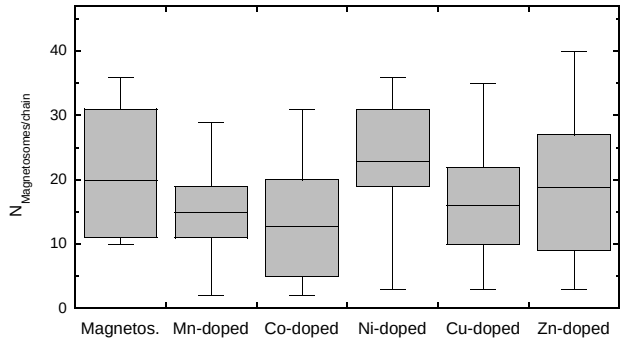

FIGURE 4.4: Comparison of the number of particle per chain in the different samples. Each box encloses 50% of the data where the continuous line represents the mean value. Vertical extended lines displays the minimum and maximum values of particles per chain found in each sample.

4.3.2 Energy-Dispersive X-ray Spectroscopy (EDS)

To estimate quantitatively the amount of M incorporated into the magnetosomes we have carried out a chemical analysis on magnetosomes extracted from bacteria by means of energy-dispersive x-ray spectroscopy (EDS) in TEM mode.

EDS was performed on extracted magnetosomes adsorbed either onto 300 mesh carbon-coated copper grids (for Mn, Co and Ni doped-magnetosomes) or onto 300 mesh lacey-carbon molybdenum grids (for Cu and Zn doped-magnetosomes), to avoid the superposition of the grid absorption lines with the energies correspond-

ing to the metal of interest. Images were obtained with a Philips CM200 electron microscope at an accelerating voltage of 200 kV which includes EDS detector. EDS spectra were acquired with a counting time of 5 min to optimize a good signal to noise ratio and to minimize the induced irradiation damage. The employed beam size was $\sim$ 65 nm, allowing the microanalysis of small clusters of several magnetosomes. Thus, EDS was performed on selected areas, represented by white squares in TEM-micrographs displayed in Fig. 4.5. Every area was chosen from different regions of the same sample to prevent deterioration of the specimen from radiation.

Fig. 4.5 displays EDS spectra obtained from different regions of M-doped magnetosome samples. All spectra show two main peaks. The one at lower energies ($\sim$ 6400 eV) corresponds to the Fe-K_α emission line, and the one at higher energies ($\sim$ 7060 eV) to the Fe-K_β. Mn, Co and Ni samples present also two large peaks at 8038 and 8905 eV, which correspond to Cu emission energies, arising from the copper grid employed for the sample preparation. The position of the M-K_α emission lines have been marked with a dashed line in the experimental spectra.

We have fitted each spectrum to three Gaussian functions centered at the positions of the Fe-K$_\alpha$, Fe-K$_\beta$ and M-K$_\alpha$ emission lines and we have estimated the atomic percent of M in the magnetosomes from the ratio of the integrated areas of the Fe-K_α and M-K_α peaks (M/(M+Fe)). The contribution of M-elements are imperceptible by EDS except for Co in Co-doped magnetosomes. Co-K_α emission line (at $\sim$ 6920 eV) introduces in the spectra a slight asymmetry in the low energy region close to Fe-K_β peak which leads to values of 0.9 at.% Co. However, the obtained percentage is in the same order as the EDS resolution which ranges from 1 to 2%.

In order to determine the atomic % Co more accurately we moved to Instituto de Nanociencia de Aragón. EDS analysis was carried out in a FEI Tecnai F30 electron microscope at an accelerating voltage of 200 kV. This microscope allows us to analyze single magnetosomes inside the bacterium because of its reduced beam sized and increasing the counting time to 10 min without compromising the preservation of the sample. Thus, EDS was performed either on purified magnetosomes or on unstained cells adsorbed onto 300 mesh carbon-coated copper grids.

Fig. 4.6 presents EDS measurements carried out on single extracted Co-doped magnetosomes. Fig. 4.6a-e displays the analyzed regions enclosed by a white square. Five different magnetosomes increasing in size, from 25 (a) to 48 nm (e), have been studied. The resulting EDS spectra are shown in 4.6f, where the obtaining percentages for each particle have been added. Similar spectra were obtained. EDS spectra have been fitted considering a three Gaussian functions centered at the positions of the Fe-K_α, Fe-K_β and Co-K_α emission lines, as explained above. An example of the fit to the three Gaussian functions has been added in the blue spectrum of Fig. 4.6f corresponding to a 28-nm sized particle, which presents the higher percentage of Co found. Thus, EDS analysis reveals that % Co varies from particle to particle ranging

between 1.1 to 2.0% (error ± 0.5%) -mean value 1.6 at% Co-.

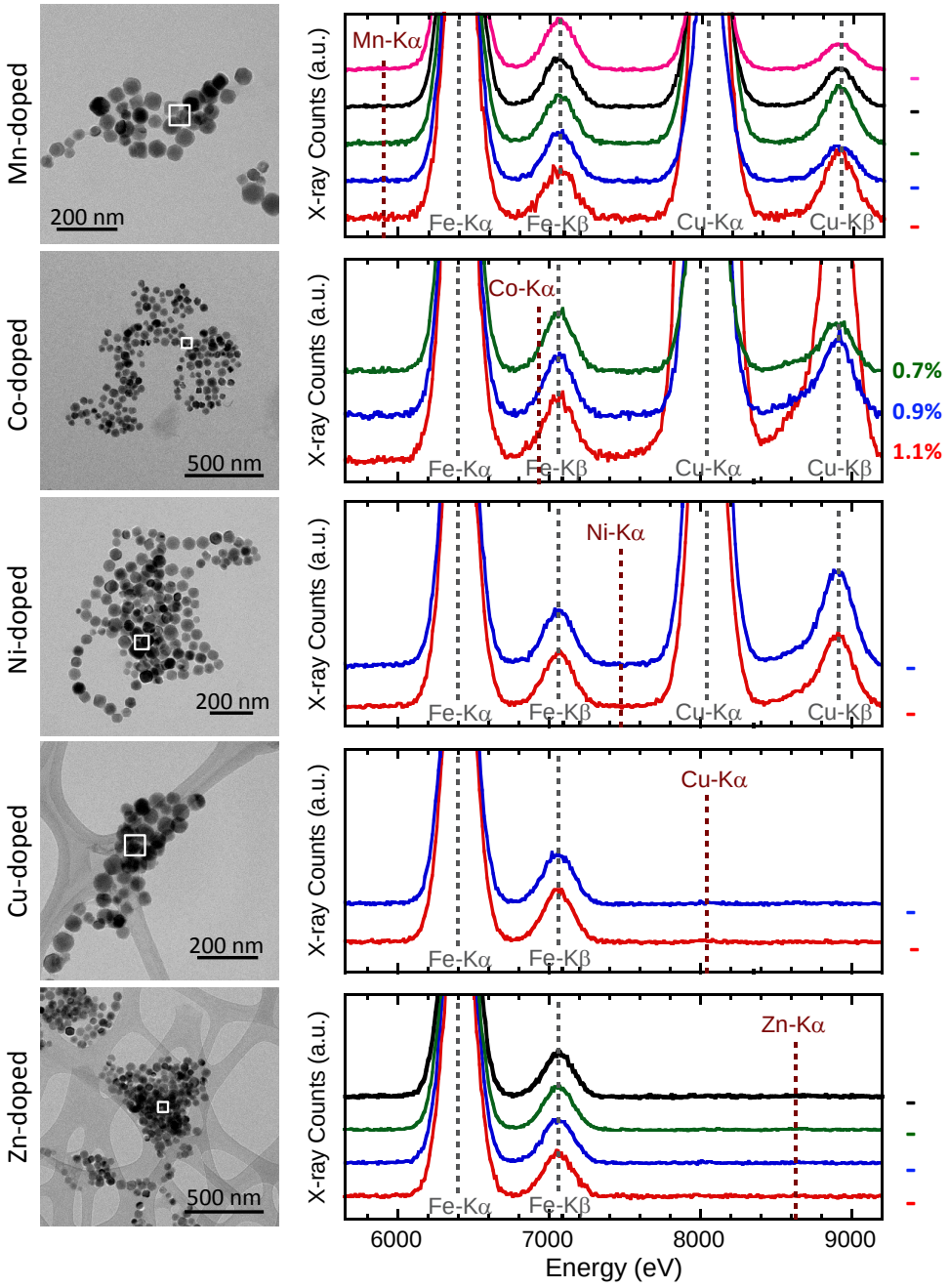

FIGURE 4.5: EDS analysis carried out on small clusters of M-doped extracted magnetosomes. Left panel presents TEM micrographs of M-doped extracted magnetosomes. White squares delimit some of the EDS analyzed regions (beam size 65 nm). Right panel displays EDS spectra acquired on the selected regions. Dashed lines indicate the position of M-K_α emission lines.

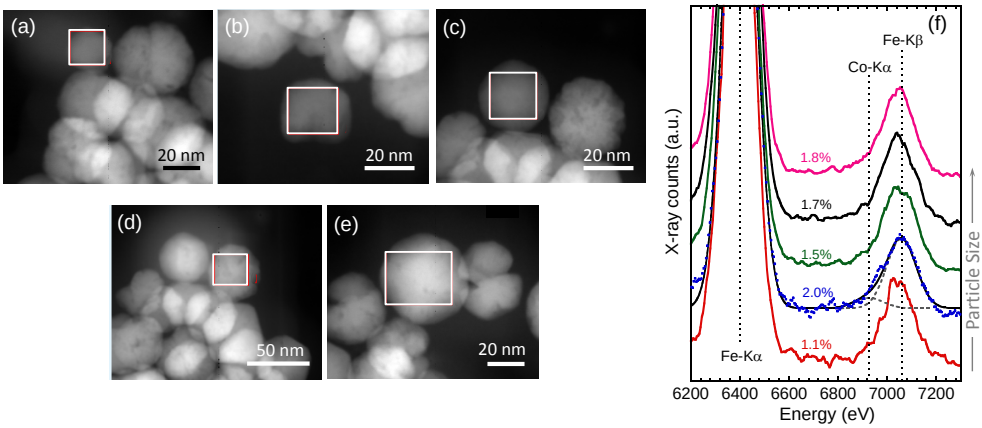

FIGURE 4.6: TEM images of individual Co-doped magnetosomes with increasing particle size: (a) 25, (b) 28, (c) 40, (d) 43 and (e) 45 nm. White squares represent the EDS analyzed region. (f) EDS spectra of the five individual Co-doped magnetosomes. Values linked to each spectrum point out the Co percentages resulting from the EDS-fitting. 28 nm-sized nanoparticle spectrum has been fitted considering a three Gaussian function centered at the positions of the Fe-K_α, Fe-K_β and Co-K_α emission lines. Dashed lines points the position of the x-ray emission lines of Fe and Co.

Finally, we have carried out a chemical analysis on the individual magnetosomes inside bacterium by means of EDS in TEM mode. As shown in Fig. 4.7a, 13 magnetosomes randomly selected out of the 19 forming the chain have been analyzed, and their corresponding EDS spectra are shown in Fig. 4.7b. Fig. 4.7c displays EDS spectrum obtained to particle (1) fitted by the three Gaussian functions. The analysis reveals that the atomic % Co ranges between 0.9 to 1.5 % from one particle to another (error fit: $\pm$ 0.5%). Thus, the Co content varies from particle to particle following a Gaussian distribution (Fig. 4.7d).

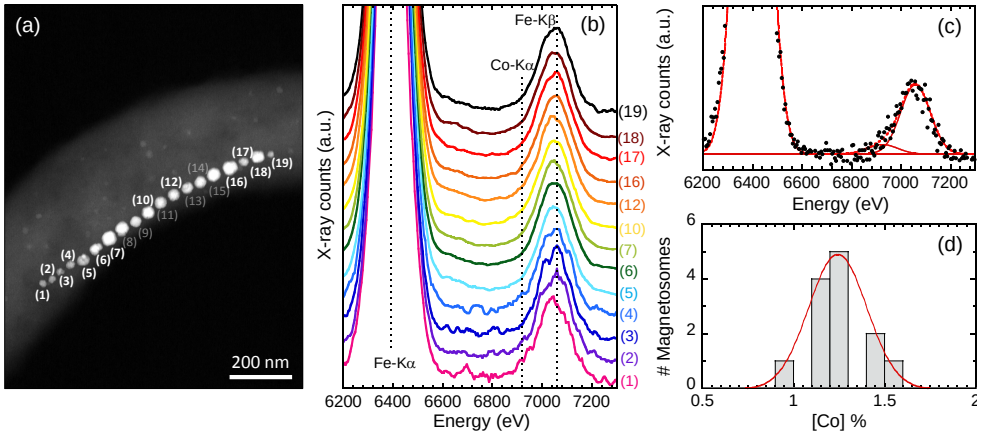

FIGURE 4.7: (a) TEM image of the analyzed magnetosomes chain within the cell. (b) EDS spectra of the thirteen individual Co-doped magnetosomes. Dashed lines mark the position of the x-ray emission lines of Fe and Co. (c) An example of the fit to three Gaussian functions. d) Distribution of the atomic % Co fitted with a Gaussian function.

Unlike previous results on AMB-1[55], we have not found any relationships between atomic % Co and the magnetosome size or position of the particle in the chain.

In summary, EDS analysis reveals the presence of variable content of Co with a mean concentration of 1.2 at.% Co in the Co-doped magnetosome. However, the technique is not sensitive enough to determine the presence of the rest of the elements, where the only conclusion one can draw is that any contribution is below 1 at.%.

These results agree with the values found in bibliography about magnetosome doping in *M. gryphiswaldense*. Namely, Perez-Gonzalez et al.[162] and Prozorov et al.[153] report a ∼1% Mn in Mn-doped magnetosomes, while Staniland et al.[53] estimate a 1.4% Co in Co-doped magnetosomes.

4.3.3 X-ray Absorption Near Edge Structure (XANES)

The arrangement of the M ions in the magnetite structure has been investigated by using x-ray absorption near edge structure (XANES). XANES is a very powerful technique that allows us to accurately determine the site occupancy of the M cations in the spinel structure of the magnetite. Note that magnetite is an inverse spinel where the Fe ions occupy three different sites: 8 Fe^{2+} in octahedral sites (O_h), 8 Fe^{3+} in tetrahedral (T_h) sites, and 8 Fe^{3+} in octahedral (O_h) ones (see crystal structure of magnetite in Fig. 1.5). Thus, the M-doping of magnetite magnetosomes arise from the substitution of iron according to the octahedral or tetrahedral preference of the incorporated element[29,30]. In order to maximize the signal-to-noise ratio, XANES measurements were performed on isolated magnetosomes. Measurements were carried out at the branch A of BM25-Spline of the ESRF synchrotron facility (France).[169]Sample preparation and experimental details are specified in *Materials and Methods* section (see page 103).

The changes derived from the M-doping of magnetite magnetosomes will be reflected in the three characteristic features distinguished in the XANES region: the edge position, the pre-edge and the post-edge (as further explained in Chapter 3).

The edge position is a clear-cut indication of the oxidation state of the absorbing atom. Indeed, there is a linear relationship between the edge position and the oxidation state, the pre-edge position shifts towards higher energy with increasing oxidation state of the absorber. Thus, from the comparison with well-known standards is relatively simple to determine the oxidation state of the studied compound[131].

The pre-edge peak is observed up to ∼15-20 eV before the edge. The width and intensity of this peak depends on the symmetry of the absorber atom. Thus, in the present analysis, a broad and low in intensity pre-edge peak are related to centrosymmetric sites, pointing an octahedral preference, while a narrow and more intense pre-edge peak evidence a noncentrosymmetric environment, proving the tetrahedral occupation of the absorber[131,132,134,170].

Lastly, the post-edge region gives information about the medium-range order of the absorber[137–139].

Fig. 4.8a shows the Fe *K*-edge XANES spectra of control and M-doped magnetosomes. As demonstrated previously in Chapter 3[113,129], the control sample follows accurately the spectrum expected for a high quality magnetite standard. All M-doped magnetosomes display a very similar spectrum, consistent with the low M content observed before by EDS ($\approx$ 1.2 % of Co and below 1 % for the rest of metals). Therefore, the local environment around the Fe atoms is practically unperturbed.

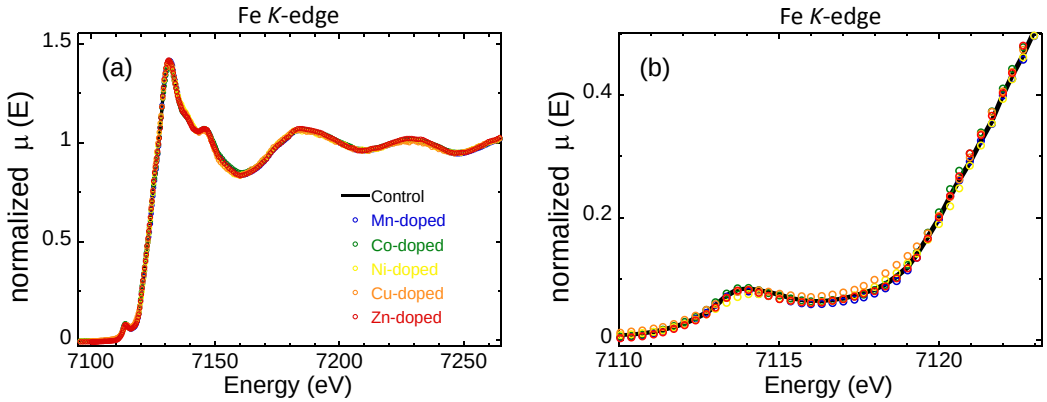

FIGURE 4.8: (a) Normalized Fe-*K*-edge XANES spectra of control magnetosomes (pure magnetite) and M-doped magnetosomes; (b) pre-edge region in more-detailed depiction.

On the other hand, Fig. 4.9 presents the XANES spectra of M-doped magnetosomes in M *K*-edges, probing the local environment of M atoms in doped magnetosomes. Each absorption-element is analyzed separately in the following.

- **Mn *K*-edge**

  Figs. 4.9a,b compare Mn-magnetosomes with different commercial Mn-oxides (reference oxides) and with $MnFe_2O_4$ provided by Mazarío et al.[171]. At a first glance, we observe the similarity between Mn-doped magnetosomes and $MnFe_2O_4$, evidencing a comparable environment. First signs of the existence of a crystal structure correspond to manganese ferrite (jacobsite) in Mn-doped magnetosomomes were already suggested by Perez-Gonzalez et al. by means of Raman analysis[162].

  From the comparison of the edge position of MnO, Mn_2O_3, MnO_2 and MnO_2, we have determined the oxidation state of Mn in Mn-doped magnetosomes. MnO is a pure Mn^{2+} compound (6542.4 eV), while Mn_2O_3 (6546.0 eV) and MnO_2 (6549.5 eV) correspond to Mn^{3+} and Mn^{4+} compounds, respectively. As shown in Fig. 4.9b, the edge position of Mn-magnetosomes (6543.3 eV) appears between the edge position of Mn^{2+} and Mn^{3+}. Since a total displacement of

3.6 eV is expected from Mn^{2+} to Mn^{3+}, a 1 eV-shift indicates the coexistence of 75% Mn^{2+} and 25% Mn^{3+} ($\pm$10%). According to the strong preference of Mn^{2+} cation to tetrahedral sites and Mn^{3+} to octahedral ones, this results is in good agreement with the inversion degree of $MnFe_2O_4$ reported in the bibliography (20-30%)[29,171–173].

In the same way, the presence of the pronounced pre-peak (6537.8 eV) (see Fig. 4.9b) confirms the higher occupancy of non-centrosymetric sites (tetrahedral) in Mn-doped magnetosomes.

In summary, XANES analysis confirms the incorporation of Mn into the magnetosome structure by showing a similar environment to $MnFe_2O_4$. The dopant is mostly incorporated as Mn^{2+} (75%), preferentially placed at tetrahedral sites by substituting Fe^{3+}, while a minor contribution of Mn^{3+} (25%) favors the occupation of octahedral places.

- **Co *K*-edge** As shown in Fig.4.9c, the spectrum is comparable to that of $CoFe_2O_4$ [163], probing the incorporation into the magnetite structure. The edge position is the same in both cases revealing that the oxidation state of the Co atoms in the Co doped magnetosomes is Co^{2+}, and the absence of a pre-edge peak strongly suggests a predominant octahedral coordination for these Co^{2+} ions.

- **Ni *K*-edge**

  Fig.4.9d confirms the absence of Ni in or associated with magnetosomes by the lack of a well-defined spectrum in the analyzed energy range, just a cloud of points is distinguishable.

- **Cu *K*-edge**

  A well-defined spectrum is presented at the Cu *K*-edge (see Fig. 4.9e). However, in this case XANES spectrum is not comparable to the expected one for $CuFe_2O_4$, pointing the absence of the Cu into the magnetosome structure. In fact, the obtained spectrum appears more like a $CuSO_4$-like structure with less intense oscillations in the post-edge region. It is worth noting that $CuSO_4$ was employed in the Cu-rich culture medium, which may result in some traces of this compound after the magnetosome extraction.

- **Zn *K*-edge**

  Fig. 4.9f compares Zn-doped magnetosomes with $ZnFe_2O_4$ and ZnO spectra at the Zn K-edge. Zn-ferrite is a normal spinel in which Zn^{+2} substitutes the Fe^{+2} ions at tetrahedral sites[29,30]. On the other hand, ZnO presents an hexagonal wurtzite structure described as a group of alternating planes composed of oxygen tetrahedrally coordinated and Zn^{2+} cations[174].

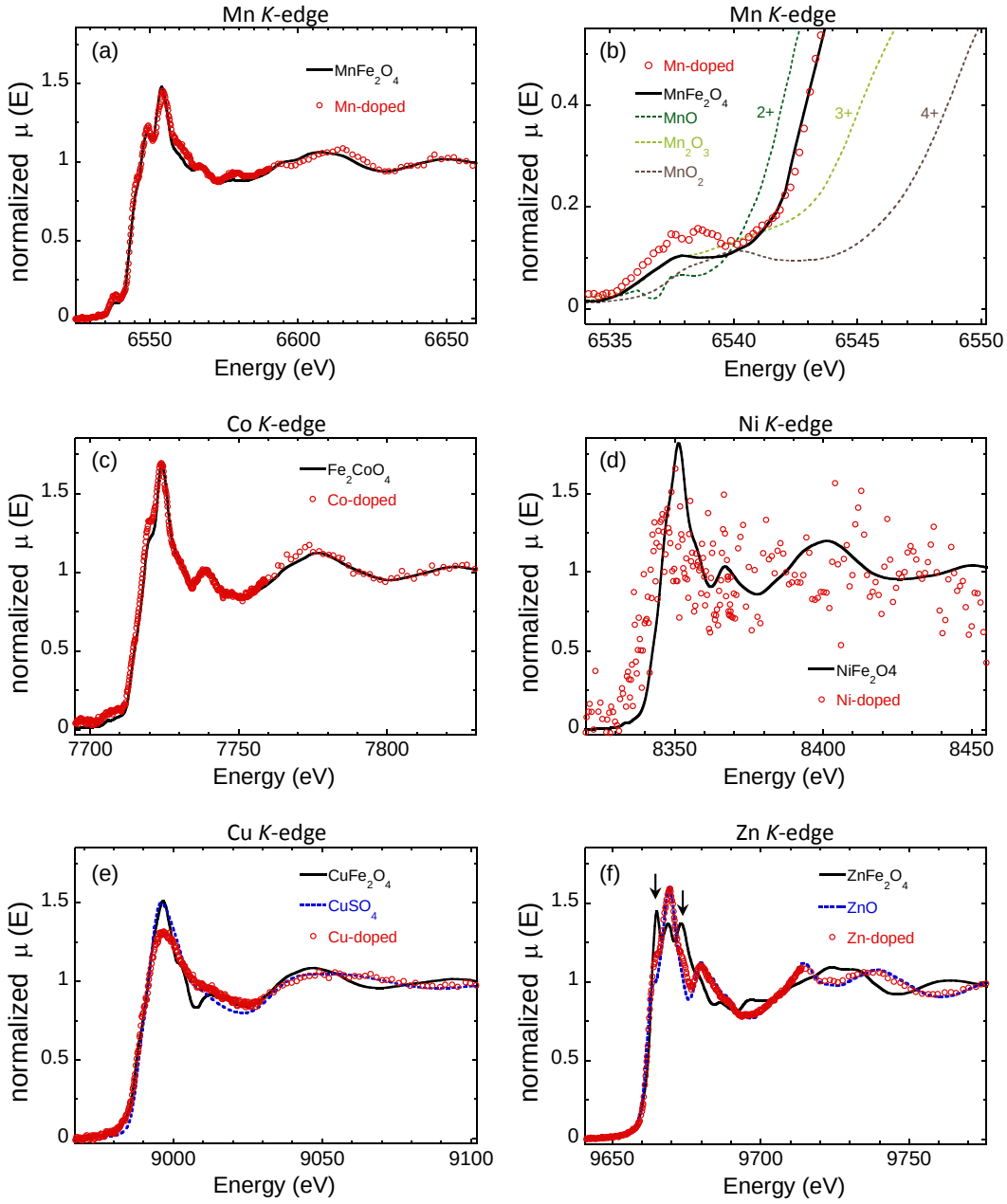

FIGURE 4.9: Normalized XANES spectra at the different M *K*-edges. (a) Mn *K*-edge: Mn-doped magnetosomes together with $MnFe_2O_4$. (b) Mn pre-edge region in more-detailed depiction compared to commercial oxides: MnO (Mn^{2+}), Mn_2O_3 (Mn^{3+}) and MnO_2 (Mn^{4+}). (c) Co *K*-edge: Co-doped magnetosomes compared to Fe_2CoO_4. (d) Ni *K*-edge: Ni-doped magnetosomes and Fe_2NiO_4. (e) Cu *K*-edge: Cu-doped magnetosomes compared to Fe_2CoO_4 and $CuSO_4$. (f) Zn *K*-edge: Zn-doped magnetosomes together with Fe_2ZnO_4 and ZnO.

It should be noted the similitude of Zn-doped magnetosomes spectrum with ZnO rather than $ZnFe_2O_4$. However, even when both spectra are pretty comparable, Zn-doped magnetosomes spectrum presents two shoulders at 9665

and 9674 eV (highlighted by two black arrows in Fig. 4.9f) absent in ZnO but characteristic of $ZnFe_2O_4$. Thus, the spectrum of the Zn-doped magnetosomes were then fitted to a linear combination of both references, ZnO and $ZnFe_2O_4$. As a result of these fits we have been able to quantify the presence of each phase: 71% ZnO and 29% of $ZnFe_2O_4$ (see Fig.4.10).

This result suggests that a minimal percentage is immersed into the magnetite structure of magnetosomes, just 29% of the absorbed Zn presents ferrite environment in Zn-doped magnetosomes. Considering that the total content of Zn is below the resolution limit of EDS (<1%), we can conclude that the presence of Zn in the magnetosome structure, even detected by XANES spectroscopy, is insignificant.

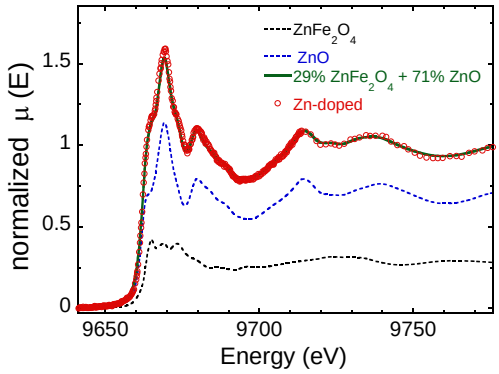

FIGURE 4.10: Linear combination fitting of Zn-doped magnetosomes XANES spectrum by considering 71% ZnO and 29% $ZnFe_2O$.

To sum up, XANES analysis showed that out of the five tested metals, only Mn and Co were incorporated into the magnetosome structure. Hence, hereinafter we will only focus on these elements to carry out the magnetic characterization.

4.4 Magnetic Characterization

The incorporation of Mn and Co into the magnetosome structure is expected to modify the magnetic properties of magnetosomes. Henceforth, in this section we will proceed to analyze these changes.

4.4.1 Magnetization vs temperature, M(T)

M(T) measurements were carried out on the whole cells. The samples were freeze-dried and encapsulated in gelatin capsules. The zero-field-cooling/field-cooling (ZFC/FC) magnetization curves were measured in a superconducting quantum interference device magnetometer (Quantum Design MPMS-3): samples were cooled in absence of any external field from 300 K down to 5 K. At 5 K a fixed magnetic field of 5 mT was applied and the magnetization was measured upon warming to 300 K (ZFC). With the field still on, the sample was cooled down to 5 K and the magnetization was measured upon warming to 300 K (FC).

Fig. 4.11 shows the zero-field cooling/field cooling (ZFC/FC) curves of the control, Mn-doped and Co-doped magnetosome chains.

Control. Control magnetosome chains present a marked irreversibility in the whole studied temperature range, the blocking temperature being above 300 K as expected due to the large size of the magnetosomes. The ZFC curve displays a sharp transition at $T_V = 107$ K corresponding to the well-known Verwey transition, a cubic-to-monoclinic crystallographic phase transition characteristic of magnetite. The Verwey transition occurs at lower temperatures in magnetosomes than in bulk magnetite (about 120 K) as observed previously[28,129,175]. The fact that the Verwey transition is so abrupt reflects the homogenous stoichiometry of the biomineralized magnetite. At 30 K the ZFC presents a shoulder attributed to the ordering of electron spins in magnetite at low temperature[176–178]. The Verwey transition is also observed in the FC curve, and in its derivative (see inset Fig. 4.11), but in this case the magnetization decreases only slightly below T_V and remains constant down to 5 K. In the FC curve the low-temperature transition is absent.

Mn-doped. ZFC/FC curves of Mn-doped magnetosome chains present a similar shape to the control sample with no noticeable changes. As in the control, the ZFC/FC curves of Mn-doped magnetosome chains show clear irreversibility in this temperature range. A slightly smoother Verwey transition is clearly present in Mn-doped magnetosome chains slightly shifted to 103 K, probably attributed to the presence of Mn[54,153,162]. The low-temperature transition observed at 30 K is comparable to the observed in the control sample. The FC curve reproduces the Verwey transition (see inset Fig. 4.11). Below T_V, the magnetization slightly falls and remains constant to 5 K, as in control sample.

Co-doped. The ZFC/FC curves of Co-doped magnetosome chains show clear irreversibility, but the shape of the curves is markedly different. In the ZFC curve stands out a wide maximum at about 150 K. The Verwey transition is only barely discerned at 100 K, and the low temperature transition is almost vanished. On the other hand, the FC magnetization increases monotonically as the temperature decreases, until it reaches a plateau below the Verwey transition (100 K), identified as the point at which the derivative of the FC curve becomes null (see inset in Fig. 4.11).

4.4.2 Magnetization vs magnetic field M(H)

M(H) measurements were performed on the whole cells as well, using similar samples as in M(T) measurements. Isothermal magnetization loops were measured at magnetic fields between 4 and -4 T at different temperatures, with no applied magnetic field in the cooling process either on a superconducting quantum interference device magnetometer (Quantum Design MPMS-3) -Mn-doped sample- or on a cryogen-free vibrating sample magnetometer from Cryogenic Ltd -Co-doped sample-.

The M(H) loops of the control, Mn and Co-doped magnetosome chains performed at 300, 110, and 30 K are shown in Figs. 4.12a,b and c. At 300 K the M(H)

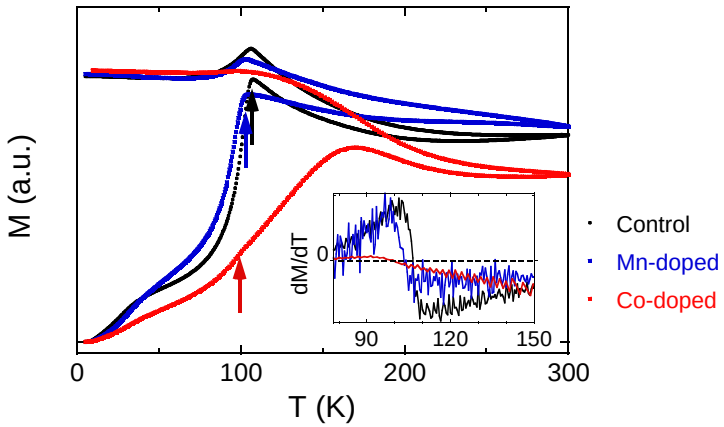

FIGURE 4.11: Magnetization curves measured at 50 mT for the control, Mn and Co-doped magnetosome chains. The inset displays the derivative of FC for the three samples. Black, blue and red arrows highlight the Verwey transition in control, Mn and Co-doped magnetosomes, respectively.

loops of control and Co-doped magnetosomes chains overlap, while the hysteresis loop of Mn-doped magnetosomes is slightly narrower. As the temperature decreases clear differences in the shape of the loops arise. These differences between the control, Mn and Co-doped magnetosome chains can be easily tracked in the plots of the coercive field ($\mu_0 H_c$) and reduced remanence (M_r/M_s) versus temperature shown in Figs. 4.12d,e.

Control. In the control magnetosome chains, the coercivity is nearly constant from 300 K down to T_V with $\mu_0 H_c \approx 22$ mT. Below T_V, the coercivity increases steeply up to 50 mT at 30 K, when the low-temperature transition takes place. After that, $\mu_0 H_c$ raises again up to 73 mT at 5 K. Conversely, the M_r/M_s value remains fairly constant between 0.44 and 0.49 throughout the whole temperature range.

Mn-doped. Despite the low Mn content, the magnetic response of the Mn-doped magnetosome chains changes significantly. The coercivity is nearly constant from 300 K down to T_V with $\mu_0 H_c \approx 15$ mT, representing a decrease of $\sim 30\%$ with respect to control magnetosome chains. Below T_V, a mild increase up to 50 K takes place reaching values of 23 mT. Then, below low-temperature transition (30 K), $\mu_0 H_c$ increases sharply up to 52 mT at 5K The M_r/M_s value remains fairly constant around 0.39 up to T_V. Below T_V, remanence rises gradually reaching values of 0.49 at 50 K, overlapping control values.

Co-doped. The incorporation of 1.2 at % Co into the magnetosome structure leads also to changes in the magnetic response of the Co-doped magnetosome chains. Regarding $\mu_0 H_c$, instead of two well-defined kinks as those found in the control sample, here a progressive increase takes place as the temperature decreases, moderately down to ~ 150 K, and steeply after that point down to 5 K. The coercive field at 300 K (20 mT) is coincident with the value found for the control magnetosomes, but at lower temperatures it becomes consistently higher, up to 60% higher than the coercive field of the control sample (110 K). The reduced remanence is nearly constant

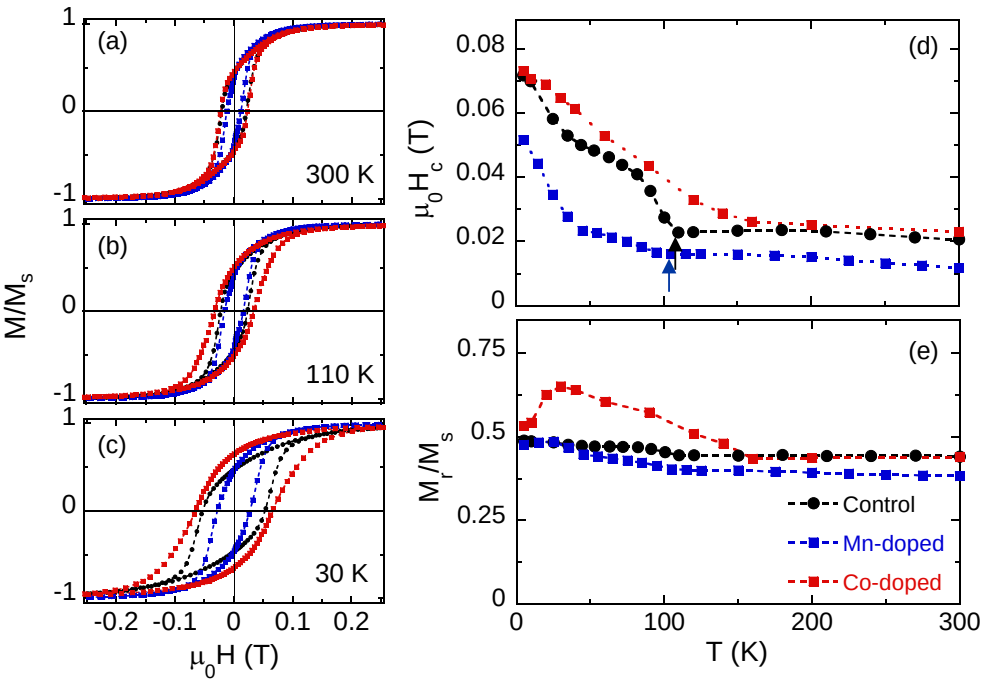

FIGURE 4.12: Hysteresis loops of the control, Mn and Co-doped magnetosome chains measured at (a) 300 K, (b) 110 K and (c) 30 K. d) Coercive field ($\mu_0 H_c$) and e) reduced remanence magnetization (M_r/M_s) comparison as a function of temperature. The black and blue arrows in (d) marks the Verwey transition (T_V) of the control and Mn-doped magnetosomes, respectively.

from 300 K down to 150 K at $\approx$ 0.45, similarly to the control magnetosomes, but increases notably up to $M_r/M_s = 0.65$ at 30 K and drops steeply afterward, down to 0.53 at 5 K.

After confirming the tunning of the magnetic properties due to the Mn and Co doping, and in order to reach a deeper understanding, hereinafter we will focus exclusively on the changes derived from the Co incorporation. With this aim we carried out X-ray magnetic circular dichroism (XMCD) experiments on Co-doped magnetosome chains and developed a theoretical modelling of the magnetic measurements. On the other hand, the interpretation of the magnetic changes derived from Mn-doping remains open as a future work.

4.4.3 X-ray Magnetic Circular Dichroism (XMCD) on Co-doped magnetosomes

X-ray magnetic circular dichroism (XMCD) at the $L_{2,3}$-edges is a powerful element-specific tool for studying the magnetic moment of each element, as dipole transition is from the $2p$ level to the $3d$. In this section, we present X-ray absorption spectroscopy (XAS) and XMCD spectra obtained in both, Fe and Co L-edges. In addition, to further evaluate the Co^{2+} substitution and its effect in the magnetic properties, we have measured element-specific hysteresis loops by XMCD at the Fe and Co L_3-edge.

XMCD experiments were performed on extracted magnetosomes using the ALICE station[179,180] at the PM3 beamline of BESSY II in Berlin, Germany. Sample preparation and experimental details are found at page 103 in *Materials and Methods* section.

XAS and XMCD spectra

Figs. 4.13a,b show the normalized absorption spectra at magnetic remanence after positive (I^+) and negative (I^-) magnetic fields at the Fe $L_{2,3}$-edges of the control and Co-doped magnetosomes measured in total electron yield (TEY) at room temperature. As shown in Fig. 4.13c, the resulting L_3 XMCD spectrum, I^+-I^-, of the control magnetosomes consists of three main components related to the three different iron occupations of magnetite. As we have also indicated in Chapter 2 (see Fig. 2.11b), the sign of the magnetic dichroism for each component is defined by the direction of its magnetic moment. Since Fe^{2+} and Fe^{3+} in octahedral places are aligned ferromagnetically, negative intensities are obtained for both, while for Fe^{3+} placed in tetrahedral sites, coupled antiferromagnetically with the Fe^{3+} in octahedral sites, the peak shows a positive intensity.

By comparing XMCD data with theoretical spectra for each individual component[181,182], the site occupancies of the Fe cations have been estimated. Simulated spectra have been calculated using crystal multiplet calculations implemented within the CTM4XAS code developed by de Groot and co-workers[183]. For that, we have reproduced tetrahedral and octahedral environments for Fe^{2+} and Fe^{3+} considering the parameters described by Pearce et al[184]. The best linear combination fits obtained from the three theoretical components already mentioned between 706.0 and 711.3 eV have been superimposed in Fig 4.13c. For the control magnetosomes, the fit results give a ratio of Fe^{2+}_{Oh}:Fe^{3+}_{Th}:Fe^{3+}_{Oh} of $0.98(4) : 1.00(5) : 1.07(5)$, close to the expected ratio for stoichiometric magnetite (1:1:1). In contrast, for Co-doped magnetosomes the fit gives a ratio of $0.85(4) : 1.00(5) : 1.19(6)$.

The significant decrease of 4% in the Fe^{2+}_{Oh} peak intensity, even evident at a first glance, indicates that the Co^{2+} ions are substituting the octahedral Fe^{2+} ions. The percentage of Co estimated by XMCD (4%) is significantly higher than the one obtained from the EDS analysis ($\sim$ 1 at. %). This discrepancy is attributed to the short probing depth (3-5 nm) of the XMCD measurements, performed in total electron yield mode, and suggests a higher cobalt concentration in the surface of magnetosomes than in the core.

On the other hand, Figs. 4.13d,e present the XAS and XMCD spectra measured at Co L_3-edge in transmission mode at 5 K. The resulting L_3 XMCD theoretical spectrum calculated considering Co^{2+} in an octahedral environment reproduces the experimental (see Fig. 4.13e)[55].

Thus, XMCD at Fe and Co $L_{2,3}$-edges confirms once again the octahedral occupancy of Co^{2+} cations in the magnetite spinel structure.

Element-specific hysteresis loops

To further evaluate the effect of Co^{2+} in the magnetic properties of Co-doped magnetosome chains, we have measured Fe and Co-specific hysteresis loops using XMCD as a magnetic contrast mechanism. For that, the energy of the monochromator was set either to the Fe L_3 (708.3 eV) or Co L_3 (779.4 eV) resonances. At set energy, the magnetic field switches between $\pm$0.74 T while collecting the transmit-

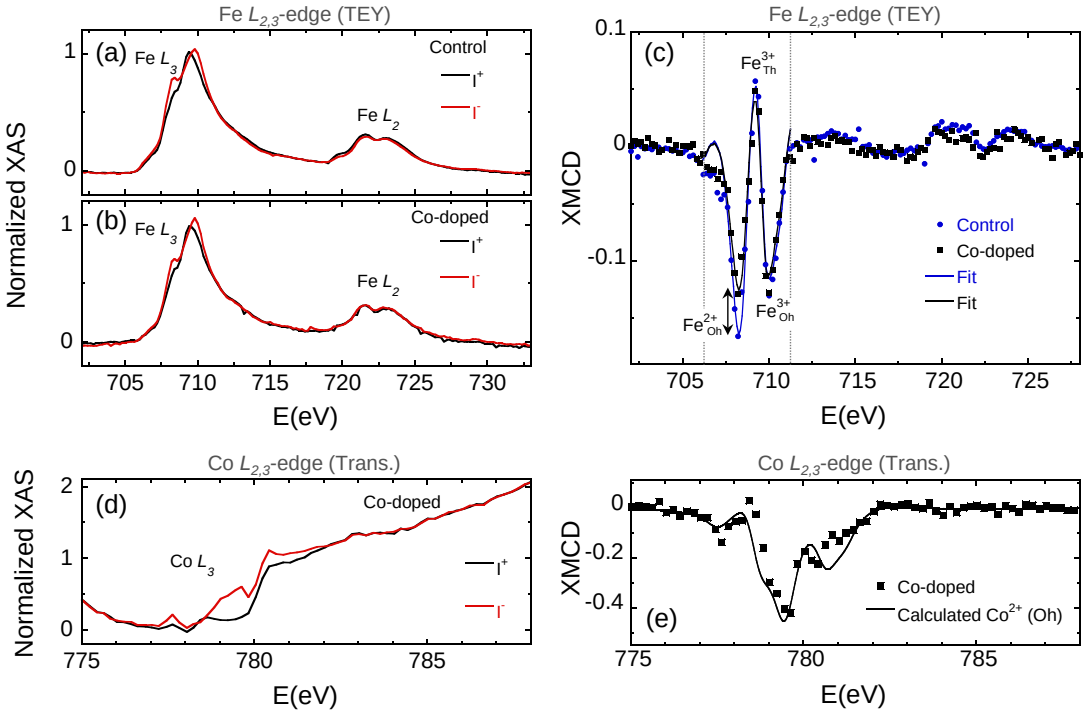

FIGURE 4.13: TEY X-ray absorption spectra (XAS) at Fe $L_{2,3}$-edges of (a) control magnetosomes and (b) Co-doped magnetosomes acquired at magnetic remanence after positive (I^+) and negative (I^-) magnetic fields. Magnetic contribution, $I^+ - I^-$, gives the XMCD signal presented in (c), where the best linear combination fits have been superimposed. (d) XAS spectra at Co L_3-edge of Co-doped magnetosomes taken at ± 0.74 T ($I^{\pm}$). The XMCD signal ($I^+ - I^-$) is presented in (e).

ted intensity (see *Materials and Methods* section for a more detailed description).

Fig. 4.14 displays the obtained hysteresis loops at Fe and Co L_3-edge for control (Fig. 4.14a) and Co-doped magnetosomes (Fig. 4.14b) measured at 5 K . From the comparison of hysteresis loops at Fe L_3-edge of both samples, we observe again the notable increase of the coercive field and reduced remanence magnetization as a consequence of Co incorporation, previously manifested in M(H) measurements (Fig. 4.12).

On the other hand, the similitude between hysteresis loops measured for Co-doped magnetosomes at Fe and Co L_3-edge (Fig. 4.14b) evidences the presence of a unique magnetic phase. The differences observed between both curves are attributed to an inhomogeneous distribution of the Co^{2+} within the magnetosome. This fact, agrees with the large atomic percentage of cobalt deduced from XMCD spectrum measured in TEY (4 %) compared to EDS results (∼1 %), pointing out a slightly higher concentration of Co close to the surface of particle compared to the core[55].

4.4.4 Magnetic model of Co-doped magnetosome chains

In order to understand the observed features in the magnetic measurements caused by the Co^{2+} incorporation into the magnetosomes structure and, in particular, its

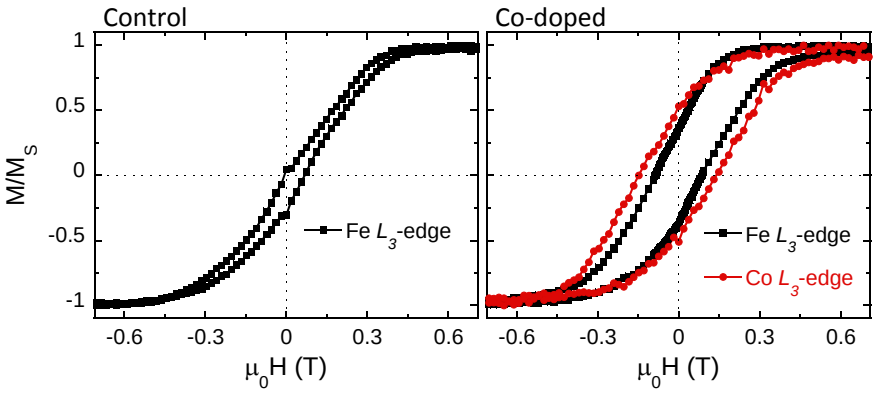

FIGURE 4.14: Element-specific hysteresis loops measured at 5K by XMCD at Fe (black line) and Co $L_{2,3}$-edge (red line) of (a) control and (b) Co-doped magnetosomes.

role in the effective anisotropy, we have carried out numerical simulations of the magnetization dynamics of the magnetosomes at different temperatures by using an approach based on the Stoner-Wohlfarth model as described in Chapter 2 page 30[84,85,163,185]. For the sake of simplicity, all the data analysis has been performed considering a unique magnetic phase, omitting the expected inhomogeneities of Co^{2+} evidenced by XMCD and from the element specific-hysteresis loops.

As explained in Chapter 2, magnetosome chains have been considered as a collection of independent magnetic dipoles, where the equilibrium orientation of each magnetic dipole is calculated by minimizing the single dipole energy density E which is calculated as the sum of three contributions[86,186–188]: i) the magnetocrystalline anisotropy energy (E_c); ii) an effective uniaxial anisotropy term arising from the competition between the magnetosome shape anisotropy and the dipolar interactions between magnetosomes in the chain, (E_{uni}); iii) the Zeeman energy term (E_{Zeeman}).

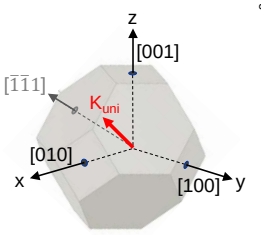

FIGURE 4.15: Schematic representation of an individual magnetosome where x, y and z conform the coordinate axes selected in the simulations coincident to $\langle 100 \rangle$ directions. Uniaxial axis (red direction) forms 25 ° with the $\langle 111 \rangle$ direction.

In spherical coordinates, considering the $\langle 100 \rangle$ crystallographic directions as the reference system (Fig. 4.15), the first term of the single dipole energy density is the cubic magnetocrystalline energy given by:

$$E_c(\theta, \varphi) = K_c \frac{[sin^4(\theta)sin^2(2\varphi) + sin^2(2\theta)]}{4} \tag{4.1}$$

being K_c the cubic anisotropy constant and θ and φ the polar and azimuthal angles,

respectively, of the magnetic moment (whose direction is given by the unit vector $\hat{u}_m$).

The second term is an effective uniaxial anisotropy contribution along the $\hat{u}_{uni}$ axis that results from the competition of the shape anisotropy of the magnetosomes and the inter-particle dipolar interactions between nearest neighbors in the chain:

$$E_{uni}(\theta, \varphi) = K_{uni}[1 - (\hat{u}_{uni} \cdot \hat{u}_m)^2] \tag{4.2}$$

where K_{uni} is the uniaxial anisotropy constant. As indicated in the previous Chapter, the direction of the uniaxial axis $\hat{u}_{uni}$ points 25° out of the chain axis towards the $\langle 110 \rangle$ directions, see Fig. 4.15[188].

The third term is the Zeeman energy in an external magnetic field $\mu_0 \vec{H}$:

$$E_{Zeeman}(\theta, \varphi) = -\mu_0 MH(\hat{u}_H \cdot \hat{u}_m) \tag{4.3}$$

where $\hat{u}_H$ represents the external magnetic field unit vector.

The single dipole energy density E is thus given by:

$$E(\theta, \varphi) = E_c(\theta, \varphi) + E_{uni}(\theta, \varphi) + E_{Zeeman}(\theta, \varphi) \tag{4.4}$$

Hysteresis loops have then been calculated following the dynamical approach described in Chapter 2. In each simulation, K_c and K_{uni} have been adjusted at each temperature in order to achieve the best match between experiment and theory. As shown in Fig. 4.16a-c, the proposed model accurately reproduces the experimental hysteresis loops and the thermal evolution of the coercivity and reduced remanence (Fig. 4.16d,e) for both the control and the Co-doped magnetosomes.

The thermal evolution obtained for K_c and K_{uni} for the control magnetosomes is shown in Fig. 4.17a. From 300 K down to the Verwey temperature T_V, the evolution of K_c reproduces the values and trend reported for bulk monocrystalline magnetite (at 300 K, $K_c = -11$ kJ/m^3)[189]. On the other hand, K_{uni} remains constant (11-12 kJ/m^3) down to T_V, as expected, since shape anisotropy and the strength of magnetic interactions depend only slightly on temperature in this range of temperatures. Below T_V, the magnetocrystalline anisotropy changes from cubic to essentially uniaxial along the $\langle 100 \rangle$ directions of the original cubic spinel structure. Therefore, below T_V, the effective anisotropy is purely uniaxial (eq. 4.2) and results from the competition between the magnetocrystalline uniaxial anisotropy and the shape and interaction contribution. The resulting uniaxial anisotropy constant K_{uni} increases substantially from 11-12 kJ/m^3 at T_V to 37 kJ/m^3 at 5 K, as observed previously[190].

In the Co-doped magnetosomes, a large positive contribution to the cubic magnetocrystalline energy is observed as expected from previous works in Co-substituted magnetite[189,190]. In these calculations, a Gaussian distribution of the cubic anisotropy constant K_c has been introduced to account for the EDS results, from which the atomic % Co rounds 1% and varies from particle to particle following a Gaussian distribution (Fig. 4.7d). The mean magnetocrystalline anisotropy constant $\langle K_c \rangle$ changes substantially, appearing strongly dependent on temperature. Both, the observed temperature dependence and the obtained anisotropy values of K_c agree with the results found in the bibliography considering a concentration of 1% Co[189,191,192]: K_c is positive in all the temperature range, meaning that unlike in magnetite, the magnetocrystalline easy axes are the $\langle 100 \rangle$, and K_c increases considerably from a value of

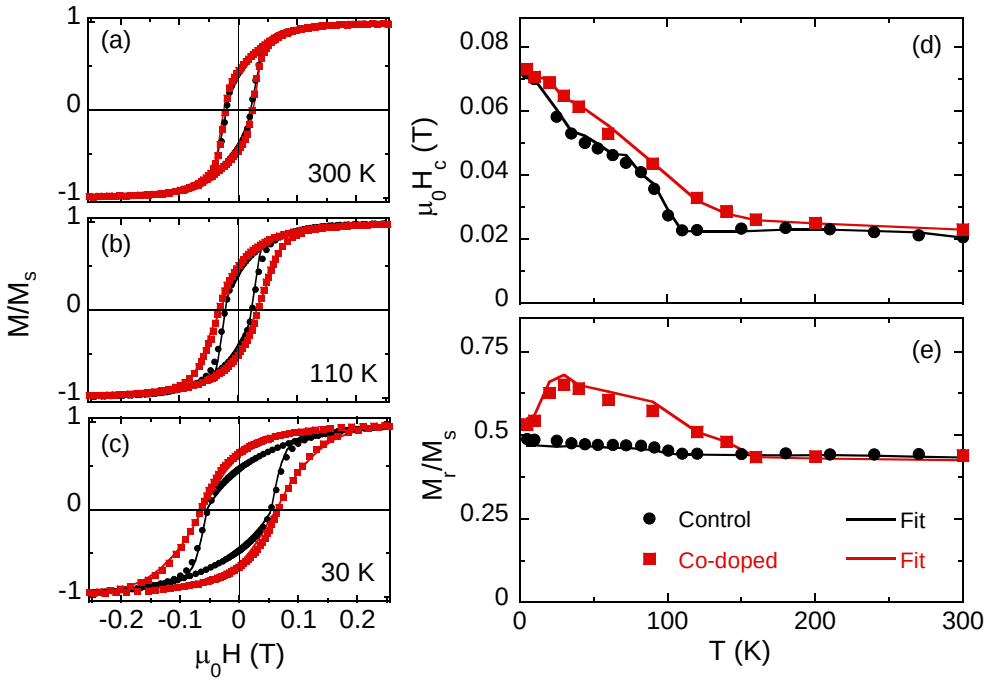

FIGURE 4.16: Hysteresis loops of the control and Co-doped magnetosome chains measured at (a) 300 K, (b) 110 K and (c) 30 K. Continuous lines correspond to the simulated loops considering the anisotropy constants shown in Fig. 4.17. d) Coercive field ($\mu_0 H_c$) and e) reduced remanence magnetization (M_r/M_s) comparison as a function of temperature. Continuous lines correspond to the values obtained from the simulation considering the anisotropy constants shown in Fig. 4.17.

8 kJ/m^3 at 300 K to 78 kJ/m^3 at 30 K. On the other hand, K_{uni} shows a similar trend as the one observed for the control magnetosomes. This is not surprising given the origin of this uniaxial anisotropy contribution, since Co doping does not introduce any change in the magnetosome shape and arrangement in the chains, as revealed by TEM.

The implications of the anisotropy constant values in the effective easy axes are reflected in the zero-field energy surfaces plotted in Fig. 4.18 at selected temperatures. For the control magnetosomes, at 300 K (see Fig. 4.18a) the energy surface shows one single minimum, meaning that the effective anisotropy is uniaxial. The position of this minimum defines the direction of the corresponding easy axis, which in this case is ($\theta = 74°, \varphi = 45°$). Thus, even though the cubic magnetocrystalline contribution (E_c) corresponding to a negative K_c ($\langle 111 \rangle$ easy axes) is well distinguished in the shape of the energy surface at 300 K, it definitely plays a minor role in the overall energy, and its main contribution is to tilt slightly the direction of the uniaxial term set at ($\theta = 80°, \varphi = 45°$).

At 110 K (Fig. 4.18b), when $K_c \approx 0$, the energy surface resembles a toroid which is flattened along the [001] direction. It is thus nearly a pure uniaxial anisotropy and the corresponding effective easy axis is coincident with the uniaxial easy axis set for the uniaxial term in eq. 4.2 ($\theta = 80°$, $\varphi = 45°$). This term dominates the overall energy down to 30 K (Fig. 4.18c), where an almost perfect uniaxial symmetry is observed.

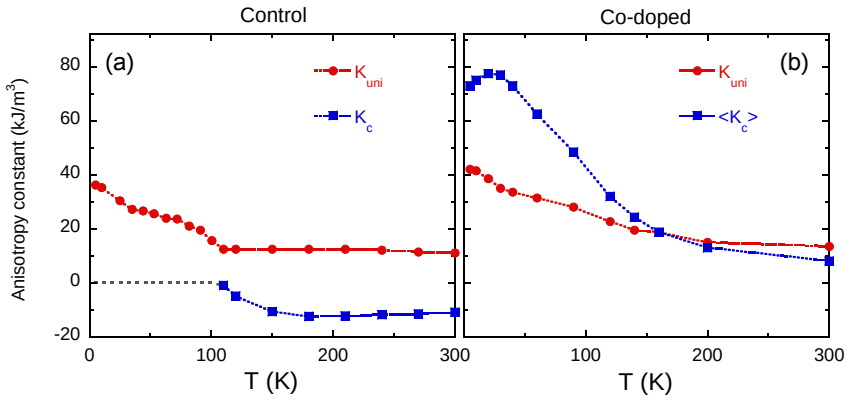

FIGURE 4.17: Temperature evolution of the anisotropy constants for (a) control magnetosomes and (b) Co-doped magnetosomes. Red dots correspond to the uniaxial anisotropy constant (K_{uni}) and blue ones represent the cubic magnetocrystalline anisotropy constant (K_c).

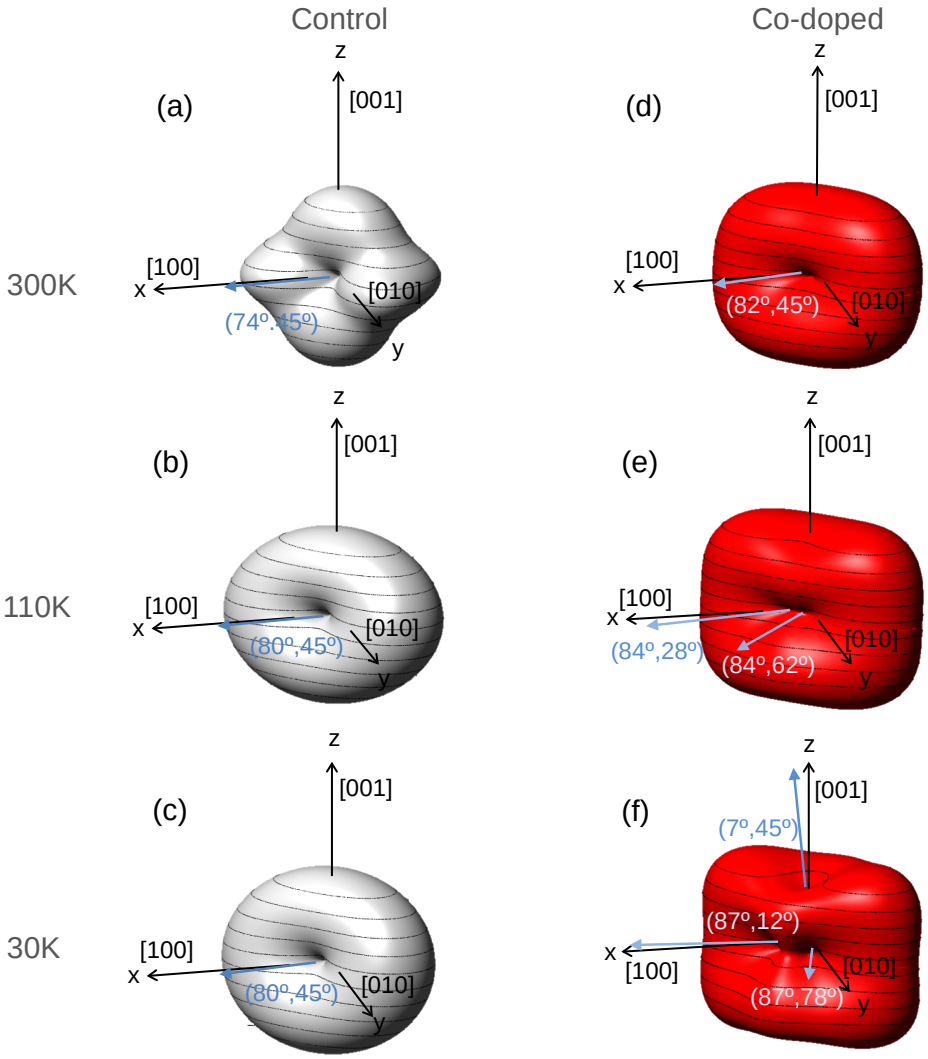

FIGURE 4.18: Zero-field energy landscapes at 300, 110 and 30 K of the control (a,b,c) and Co-doped magnetosomes (d,e,f) obtained from the simulations as explained in the text. The blue arrows represent the effective easy axes, whose directions are given by (θ, φ), where θ is the polar angle and φ the azimuthal angle.

The effective uniaxial anisotropy observed in the control magnetosomes during the whole temperature range studied is in agreement with the observed reduced remanence values close to $\approx$ 0.5 (Fig. 4.12e), as expected for randomly oriented uniaxial magnetic domains in the framework of the Stoner-Wohlfarth model[83].

On the other hand, a different scenario is observed in the Co-doped magnetosomes, as shown in Fig. 4.18d-f. At 300 K the energy shows a single minimum, corresponding to an effective easy axis along the direction (θ = 82°, φ = 45°), only slightly tilted with respect to the uniaxial term set at (θ = 80°, φ= 45°). The cubic magnetocrystalline contribution to the energy is only reflected as a slight flattening of the energy surface at the [001] axis. As the temperature decreases, the ratio of $\langle K_c \rangle / K_u$ increases and as a consequence the contribution of the magnetocrystalline cubic anisotropy to the total energy acquires an increasingly more important role, and the system evolves from showing one (300 K) to two (110 K) to finally three (30 K) effective easy axes. For $0 \leq \langle K_c \rangle / K_u \leq 1$ there is a single easy axis, though with a non-toroidal symmetry. For $1 < \langle K_c \rangle / K_u \leq 1.63$ there are two equivalent easy axes close to axes [100] and [010], and above 1.63 there are three easy axes, two of them equivalent (now even closer to [100] and [010]), and the third nearly coincident with [001]. Crossing points are located approximately at 150 K (from uniaxial to biaxial) and at 100 K (from biaxial to triaxial). This is consistent with the reduced remanence increasing above 0.5 below 150 K, since below this point the anisotropy is no longer uniaxial.

Finally, below 30 K the reduced remanent magnetization decreases remarkably from 0.65 at 30 K to near 0.5 at 5 K, as observed in Fig. 4.12e, and the hysteresis loops are no longer well reproduced following the same model as sketched in Fig. 4.15, where uniaxial anisotropy has been assumed to keep an angle of 25° with the $\langle 111 \rangle$ towards $\langle 110 \rangle$. Below 30 K the experimental loops can be accurately reproduced only if the uniaxial contribution undergoes a reorientation of about 15° towards directions [001] or [100] in the sketch of Fig. 4.15. This reorientation is accompanied by a slight decrease of the cubic anisotropy constant, as shown in Fig. 4.17b. The underlying physical mechanism behind this effect remains unclear for us. A definite fact, however, is that the reorientation cannot be related neither to shape anisotropy nor to dipolar interaction effects, but instead should be linked to the Co-doped magnetite phase itself. Additional insight provided by electronic transfer properties measurements or more precise structural determination could shed light on this matter.

4.5 Summary

From the combination of structural and magnetic techniques we have proven the incorporation of low amounts of Mn (<1 at.%) and Co ($\sim$1 at.%) into the magnetite structure. The incorporation of these elements drastically modifies the magnetic features of the doped magnetosomes opening up the possibility of obtaining magnetosomes with tunable magnetic properties.

Mn cations are mostly incorporated as Mn^{2+} (75%) by substituting Fe^{3+} in tetrahedral sites while a minority Mn^{3+} (25%) prefers tetrahedral sites. Mn-doping leads to an important decrease of the magnetic coercivity.

On the other hand, Co is as Co^{2+} substituting Fe^{2+} located in octahedral places.

The presence of Co^{2+} substituting Fe^{2+} into the magnetosome structure, adds a large positive contribution to the magnetocrystalline anisotropy of magnetosomes. This magnetocrystalline anisotropy is strongly dependent on temperature and competes with a uniaxial anisotropy that results from the shape anisotropy of the magnetosome and the dipolar interactions between them in the chain.

Further investigations on magnetic behavior of Co-doped magnetosomes have been performed. Based on the Stoner-Wohlfarth model slightly modified and considering the different anisotropy contributions, we have been able to accurately reproduce the magnetic behavior of the control and Co-doped magnetosome chains, and have determined the direction of the easy axes of the magnetization as a function of the temperature. In contrast to the control magnetosome chains, whose effective anisotropy is uniaxial in the whole temperature range, the effective anisotropy of Co-doped magnetosome chains changes appreciably with temperature, from uniaxial from 300 to 150 K, to biaxial down to 100 K, and triaxial below 100 K. Further research effort should focus on the electronic state of the Co-doped magnetosomes at very low temperatures.

The magnetic modeling of the magnetization dynamics of Mn-doped magnetosomes remains open as a future work.

Materials and Methods

Minimum Inhibitory Concentration (MIC) assays

The sterile growth media with increasing metal-concentrations were poured into sterile microplates. Each microplate presents 96 wells distributed in 12 columns, in which different metal concentration were tested, and 8 rows, where 8 replicates were carried out (see Fig.4.19.a,b). Each well were inoculated with 10^6 cell/mL of *M. gryphiswaldense*. Microplates were incubated at 28 °C for 120 h. The cell growth was analyzed by studying the optical density at 565 nm (OD) based on the amount of light scattered by the culture of each single well on a Synergy HTX Multi-Mode Microplate Reader (BioTek) (see Fig.4.19.c). Finally, the MIC value is determined as the cut-off point of cell-growth.

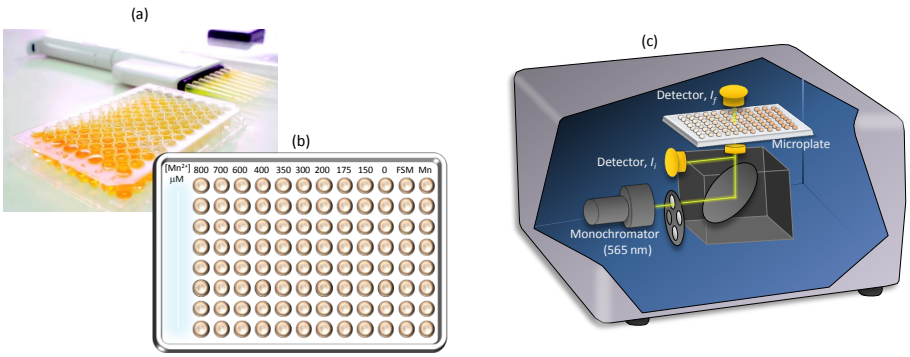

FIGURE 4.19: (a) Image of a microplate with the employed multi-channel pipete, (b) schematic representation of microplate with the increasing metal concentrations - corresponding to Mn (see Fig. 4.1a)- MIC assay and (c) schematic drawing of the microplate reader.

The employed metal compounds for MIC assays and successive bacterial cultures were: Manganese(II) citrate decahydrate ($C_{12}H_{10}Mn_3O_{14} \cdot 10\,H_2O$, purchase from Carbosynth (10024-66-5)), Co(II) citrate dihydrate ($C_{12}H_{10}Co_3O_{14} \cdot 2\,H_2O$, from Alfa Aesar (6424-15-3), Nickel(II) sulfate ($NiSO_4 \cdot 7\,H_2O$, from Sigma-Aldrich (10101-98-1)), Copper(II) sulfate ($CuSO_4$, from Sigma-Aldrich (7758-98-7)) and Zn(II) sulfate ($ZnSO_4 \cdot 7\,H_2O$, from Sigma-Aldrich (7446-20-0)). The dissociation of these compounds in aqueous solution give rise to transition metal ions (M^{2+}) solved in the growth medium and other inorganic ions harmless to the bacterial growth.

X-ray Absorption Near Edge Structure (XANES)

XANES measurements were performed on isolated magnetosomes. For these measurements, extracted magnetosomes were freeze-dried and thoroughly mixed with sugar. Sugar matrix presents a low absorption coefficient and it is water-soluble, allowing magnetosome recovery by magnetic separation after XANES measurements. The resultant mixture was compacted into 5 mm diameter pills.

The experiment was performed at room temperature and atmospheric conditions at the branch A of BM25-Spline of the ESRF synchrotron facility (France)[169].The monochromator used in the experiments was a double crystal of Si(111). Fe, Mn, Co, Ni, Cu and Zn foils were measured simultaneous to data acquisition for the subsequent energy calibration. In these conditions, the edge position of the sample can be determined with an accuracy of 0.3 eV. Measurements of control magnetosomes (Fe_3O_4), and a commercial M-references were measured in transmission mode at the Mn (6539 eV), Fe (7112 eV), Co (7709 eV), Ni (8333 eV), Cu (8979 eV) and Zn (9659 eV) *K*-edge, respectively. Control and M-doped magnetosome sample was acquired in transmission mode at the Fe *K*-edge and in fluorescence yield mode at the M *K*-edge. From three to five spectra were acquired for each edge and merged to improve the signal-to-noise ratio. All the data were treated by the Athena software from the Iffefit package[147].

X-ray Magnetic Circular Dichroism (XMCD)

XAS and XMCD spectra

XMCD experiments were carried out on extracted magnetosomes using the ALICE station[179,180] at the PM3 beam line of BESSY II in Berlin, Germany.

Fe $L_{2,3}$ XAS spectra were collected at room temperature. A drop of 5 μL of purified magnetosomes in aqueous solution (20 μg/mL of Fe_3O_4) was deposited onto silicon substrates. Data acquisition was done in total electron yield mode (TEY) with the incoming circularly polarized (right helicity) x-rays impinging at normal incidence with respect to the sample surface. A magnetic field of ± 0.27 T was applied along the beam propagation direction. X-ray absorption spectra (I) were obtained across the Fe $L_{2,3}$ with a step size of 0.2 eV. At each photon energy data was acquired at magnetic remanence after positive (I^+) and negative (I^-) magnetic fields to yield the XMCD signal given by $I^+ - I^-$.

On the other hand, Co L_3 XAS spectra were acquired at 5K. This time, more concentrated samples were employed to ensure the Co-absorption resolution. Thus, a drop of 5 μL of purified magnetosomes in aqueous solution (10 mg/mL of Fe_3O_4) were deposited onto 300 mesh carbon-coated copper grids. Data acquisition was

done in transmission mode with the incoming circularly polarized (right helicity) x-rays impinging at normal incidence with respect to the sample surface. A magnetic field of ± 0.74 T was applied along the beam propagation direction. X-ray absorption spectra (I) were obtained across the Co L_3 with a step size of 0.2 eV. At each photon energy data was acquired at positive (I^+) and negative (I^-) magnetic fields five times to optimize the signal-to-noise ratio. XMCD is defined as I^+-I^-.

A second-degree polynomial background was subtracted from the experimental XMCD curves to account for a preexisting time-dependent background.

Element-specific hysteresis loops

Element-specific hysteresis loops were carried out at 5 K in the high concentrated sample (10 mg/mL of Fe_3O_4) deposited onto 300 mesh carbon-coated copper grids described above. Data acquisition was done in transmission mode with the incoming light circularly polarized (right helicity). The energy of the monochromator was set either to the Fe L_3 (708.3 eV) or Co L_3 (779.4 eV) resonances. At set energy, the magnetic field switches between ± 0.74 T while collecting the transmitted intensity. Hysteresis loops were obtained by plotting the dichroic signal as a function of the applied magnetic field. From ten to thirty hysteresis loops were acquired for each edge and merged to improve the signal-to-noise ratio.

List of publications resulting from this Chapter

1. L. Marcano, D. Muñoz, R. Martín Rodríguez, I. Orue, J. Alonso, A. García-Prieto, A. Serrano, S. Valencia, R. Abrudan, L. Fernández Barquín, A. García-Arribas, A. Muela, and M. Fdez-Gubieda,, "Magnetic Study of Co-Doped Magnetosome Chains", *The Journal of Physical Chemistry C*, vol. 122, no. 13, pp. 1541-7550, 2018.

2. L. Marcano, D. Muñoz, R. Martín Rodríguez, I. Orue, J. Alonso, A. García-Prieto, A. Serrano, S. Valencia, R. Abrudan, L. Fernández Barquín, A. García-Arribas, A. Muela, and M. Fdez-Gubieda, "On the magnetic behavior of Mn-doped magnetosomes", Under preparation.

Conclusions

The present Thesis provides a detailed experimental and theoretical findings concerning to magnetosome chains and magnetotactic bacteria.

On the basis of the slightly modified Stoner-Wohlfarth model and considering the different anisotropy contributions, we have been able to accurately reproduce the magnetic behavior of magnetosome chains. The proposed model applies both for undoped and Co-doped magnetosomes.

The main conclusions obtained are summarized below, organized along the three blocks that constitute this work.

With respect to the study of the magnetic configuration of magnetosome chains, the main conclusions are:

1. Equilibrium magnetic moment of magnetosomes is tilted 20°with respect to the chain [111] axis due to compromise effects of shape anisotropy and dipolar iterations between magnetosomes.

2. The chain shape can be reproduced by considering an interplay between the magnetic dipolar interactions between magnetosomes, ruled by the orientation of the magnetosome magnetic moment, and a lipid/protein-based mechanism caused by the interaction of the magnetosomes with a cytoskeletal filament that traverses the cell, modeled as an elastic recovery force exerted on the magnetosomes.

Concerning the research of the biomineralization process, the main conclusions are:

1. The early stages of the biomineralization process confirm the existence of a precursor of magnetite with the spectroscopic signature of Bfr. Bfr would play the role of Fe source for the magnetosome formation.

2. Along the process, there is a coexistence of two phases: Bfr and magnetite. As the process evolves, the presence of magnetite is increasingly common due to the magnetosome formation. No evidence of other phases was observed.

3. The experimental results combined with the data found in bibliography have allowed us to model the biomineralization process. Thus,

    (a) The Bfr-phase locates around the magnetosome vesicle forming a corona, playing the role of an Fe source.

(b) Iron cations from the corona are transported into the magnetosome vesicle. Inside the vesicle, precursor units of ferrihydite-like phase are formed and aggregate via oriented attachment.

(c) Then, the aggregate is partially reduced to magnetite in a fast process which grows until reaching the final size of magnetosomes.

Finally, in regard to the study of transition metal-doping of magnetosomes:

1. Among the different transition metals tested for the doping of magnetosomes, just small amounts of Mn ($\langle$ 1%) and Co ($\sim$ 1 %) were detected into the magnetosome structure. No evidences of the incorporation of Ni, Cu or Zn were found.

2. Mn cations are mostly incorporated as Mn^{2+} (75%) by substituting Fe^{3+} in tetrahedral sites while a minority Mn^{3+} (25%) prefers tetrahedral sites. Mn-doping leads to an important decrease of the magnetic coercivity.

3. Co is as Co^{2+} substituting Fe^{2+} located in octahedral places. The presence of Co^{2+} substituting Fe^{2+} into the magnetosome structure adds a large positive contribution to the magnetocrystalline anisotropy of magnetosomes. This magnetocrystalline anisotropy is strongly dependent on temperature and competes with a uniaxial anisotropy that results from the shape anisotropy of the magnetosome and the dipolar interactions between them in the chain.

Bibliography

[1] D. A. Bazylinski and R. B. Frankel, "Magnetosome formation in prokaryotes," *Nature Reviews Microbiology*, vol. 2, no. 3, pp. 217–230, 2004.

[2] D. Faivre and D. Schüler, "Magnetotactic Bacteria and Magnetosomes," *Chemical Reviews*, vol. 108, no. 11, pp. 4875–4898, 2008.

[3] D. A. Bazylinski, C. T. Lefèvre, and D. Schüler, "Magnetotactic Bacteria," in *The Prokaryotes* (E. Rosenberg, E. F. DeLong, S. Lory, E. Stackebrandt, and F. Thompson, eds.), pp. 453–494, Berlin, Heidelberg: Springer Berlin Heidelberg, 2013. DOI: 10.1007/978-3-642-30141-4_74.

[4] D. A. Bazylinski, C. T. Lefèvre, and B. H. Lower, "Magnetotactic Bacteria, Magnetosomes, and Nanotechnology," in *Nanomicrobiology* (L. L. Barton, D. A. Bazylinski, and H. Xu, eds.), ch. 3, pp. 39–74, New York, NY: Springer New York, 2014.

[5] A. Arakaki, H. Nakazawa, M. Nemoto, T. Mori, and T. Matsunaga, "Formation of magnetite by bacteria and its application," *Journal of The Royal Society Interface*, vol. 5, no. 26, pp. 977–999, 2008.

[6] E. Alphandéry, "Applications of Magnetosomes Synthesized by Magnetotactic Bacteria in Medicine," *Frontiers in Bioengineering and Biotechnology*, vol. 2, 2014.

[7] E. Alphandéry, A. Idbaih, C. Adam, J.-Y. Delattre, C. Schmitt, F. Guyot, and I. Chebbi, "Chains of magnetosomes with controlled endotoxin release and partial tumor occupation induce full destruction of intracranial U87-Luc glioma in mice under the application of an alternating magnetic field," *Journal of Controlled Release*, vol. 262.

[8] A. Araujo, F. Abreu, K. Silva, D. Bazylinski, and U. Lins, "Magnetotactic Bacteria as Potential Sources of Bioproducts," *Marine Drugs*, vol. 13, no. 12, pp. 389–430, 2015.

[9] S. Taherkhani, M. Mohammadi, J. Daoud, S. Martel, and M. Tabrizian, "Covalent Binding of Nanoliposomes to the Surface of Magnetotactic Bacteria for the Synthesis of Self-Propelled Therapeutic Agents," *ACS Nano*, vol. 8, no. 5, pp. 5049–5060, 2014.

[10] S. Martel, "Swimming microorganisms acting as nanorobots versus artificial nanorobotic agents: A perspective view from an historical retrospective on the

future of medical nanorobotics in the largest known three-dimensional biomicrofluidic networks," *Biomicrofluidics*, vol. 10, no. 2, p. 021301, 2016.

[11] S. Bellini, "Su di un particolare comportamento di batteri d'acqua dolce," *Instituto di Microbiologia dell'Universita di Pavia*, 1963.

[12] R. Blakemore, "Magnetotactic bacteria," *Science*, vol. 190, no. 4212, pp. 377–379, 1975.

[13] C. T. Lefèvre and D. A. Bazylinski, "Ecology, Diversity, and Evolution of Magnetotactic Bacteria," *Microbiology and Molecular Biology Reviews*, vol. 77, no. 3, pp. 497–526, 2013.

[14] F. F. Guo, W. Yang, W. Jiang, S. Geng, T. Peng, and J. L. Li, "Magnetosomes eliminate intracellular reactive oxygen species in *Magnetospirillum gryphiswaldense* MSR-1: Magnetosomes eliminate ROS in MSR-1," *Environmental Microbiology*, vol. 14, no. 7, pp. 1722–1729, 2012.

[15] A. Komeili, "Molecular mechanisms of compartmentalization and biomineralization in magnetotactic bacteria," *FEMS Microbiology Reviews*, vol. 36, pp. 232–255, 2012.

[16] F. Abreu, J. L. Martins, T. S. Silveira, C. N. Keim, H. G. P. L. de Barros, F. J. G. Filho, and U. Lins, "'Candidatus Magnetoglobus multicellularis', a multicellular, magnetotactic prokaryote from a hypersaline environment," *International Journal of Systematic and Evolutionary Microbiology*, vol. 57, no. 6, pp. 1318–1322, 2007.

[17] R. Uebe and D. Schüler, "Magnetosome biogenesis in magnetotactic bacteria," *Nature Reviews Microbiology*, vol. 14, no. 10, pp. 621–637, 2016.

[18] R. B. Frankel, "Magnetic Guidance of Organisms," *Annual Review of Biophysics and Bioengineering*, vol. 13, no. 1, pp. 85–103, 1984.

[19] B. Lower and D. Bazylinski, "The Bacterial Magnetosome: A Unique Prokaryotic Organelle," *Journal of Molecular Microbiology and Biotechnology*, vol. 23, no. 1-2, pp. 63–80, 2013.

[20] D. Schüler, "Genetics and cell biology of magnetosome formation in magnetotactic bacteria," *FEMS Microbiology Reviews*, vol. 32, no. 4, pp. 654–672, 2008.

[21] A. Komeili, H. Vali, T. J. Beveridge, and D. K. Newman, "Magnetosome vesicles are present before magnetite formation, and MamA is required for their activation," *Proceedings of the National Academy of Sciences of the United States of America*, vol. 101, no. 11, pp. 3839–3844, 2004.

[22] A. Komeili, Z. Li, and D. K. Newman, "Magnetosomes Are Cell Membrane Invaginations Organized by the Actin-Like Protein MamK," *Science*, vol. 311, no. 5758, pp. 242–245, 2006.

[23] K. Grünberg, E. C. Müller, A. Otto, R. Reszka, D. Linder, M. Kube, R. Reinhardt, and D. Schüler, "Biochemical and Proteomic Analysis of the Magnetosome Membrane in *Magnetospirillum gryphiswaldense*," *Applied and Environmental Microbiology*, vol. 70, no. 2, pp. 1040–1050, 2004.

[24] R. B. Frankel and R. P. Blakemore, "Navigational compass in magnetic bacteria," *Journal of Magnetism and Magnetic Materials*, vol. 15, pp. 1562–1564, 1980.

[25] E. Katzmann, A. Scheffel, M. Gruska, J. M. Plitzko, and D. Schüler, "Loss of the actin-like protein MamK has pleiotropic effects on magnetosome formation and chain assembly in *Magnetospirillum gryphiswaldense*: MamK function in M. gryphiswaldense," *Molecular Microbiology*, vol. 77, no. 1, pp. 208–224, 2010.

[26] T. Matsunaga, T. Sakaguchi, and F. Tadakoro, "Magnetite formation by a magnetic bacterium capable of growing aerobically," *Applied Microbiology and Biotechnology*, vol. 35, no. 5, pp. 651–655, 1991.

[27] K. H. Schleifer, D. Schüler, S. Spring, M. Weizenegger, R. Amann, W. Ludwig, and M. Köhler, "The genus *Magnetospirillum* gen. nov. description of *Magnetospirillum gryphiswaldense* sp. nov. and transfer of *Aquaspirillum magneticum* to *Magnetospirillum magnetotacticum* comb. nov.," *Systematic and Applied Microbiology*, vol. 14, no. 4, pp. 379 – 385, 1991.

[28] R. Prozorov, T. Prozorov, S. Mallapragada, B. Narasimhan, T. Williams, and D. A. Bazylinski, "Magnetic irreversibility and the Verwey transition in nanocrystalline bacterial magnetite," *Physical Review B*, vol. 76, no. 5, pp. 1–10, 2007.

[29] R. O'Handley, *Modern Magnetic Materials: Principles and Applications*. Wiley, 1999.

[30] B. D. Cullity and C. D. Graham, *Introduction to magnetic materials*. Hoboken, N.J: IEEE/Wiley, 2nd ed ed., 2009.

[31] R. Hergt, R. Hiergeist, M. Zeisberger, D. Schüler, U. Heyen, I. Hilger, and W. a. Kaiser, "Magnetic properties of bacterial magnetosomes as potential diagnostic and therapeutic tools," *Journal of Magnetism and Magnetic Materials*, vol. 293, no. 1, pp. 80–86, 2005.

[32] A. Muela, D. Muñoz, R. Martín-Rodríguez, I. Orue, E. Garaio, A. Abad Díaz de Cerio, J. Alonso, J. Á. García, and M. L. Fdez-Gubieda, "Optimal Parameters for Hyperthermia Treatment Using Biomineralized Magnetite Nanoparticles: Theoretical and Experimental Approach," *The Journal of Physical Chemistry C*, vol. 120, no. 42, pp. 24437–24448, 2016.

[33] T. Orlando, S. Mannucci, E. Fantechi, G. Conti, S. Tambalo, A. Busato, C. Innocenti, L. Ghin, R. Bassi, P. Arosio, F. Orsini, C. Sangregorio, M. Corti, M. F. Casula, P. Marzola, A. Lascialfari, and A. Sbarbati, "Characterization of magnetic nanoparticles from *Magnetospirillum gryphiswaldense* as potential theranostics tools," *Contrast Media and Molecular Imaging*, vol. 11, no. 2, pp. 139–145, 2015.

[34] E. Alphandéry, I. Chebbi, F. Guyot, and M. Durand-Dubief, "Use of bacterial magnetosomes in the magnetic hyperthermia treatment of tumours: A review.," *International journal of hyperthermia : the official journal of European Society for Hyperthermic Oncology, North American Hyperthermia Group*, vol. 6736, pp. 1–9, 2013.

[35] M. Timko, A. Dzarova, J. Kovac, A. Skumiel, A. Józefczak, T. Hornowski, H. Gojžewski, V. Zavisova, M. Koneracka, A. Sprincova, O. Strbak, P. Kopcansky, and N. Tomasovicova, "Magnetic properties and heating effect in bacterial magnetic nanoparticles," *Journal of Magnetism and Magnetic Materials*, vol. 321, no. 10, pp. 1521 – 1524, 2009. Proceedings of the Seventh International Conference on the Scientific and Clinical Applications of Magnetic Carriers.

[36] S. Dutz and R. Hergt, "Magnetic nanoparticle heating and heat transfer on a microscale: Basic principles, realities and physical limitations of hyperthermia for tumour therapy.," *International journal of hyperthermia : the official journal of European Society for Hyperthermic Oncology, North American Hyperthermia Group*, vol. 29, no. 8, pp. 790–800, 2013.

[37] C. Martinez-Boubeta, K. Simeonidis, A. Makridis, M. Angelakeris, O. Iglesias, P. Guardia, A. Cabot, L. Yedra, S. Estradé, F. Peiró, Z. Saghi, P. a. Midgley, I. Conde-Leborán, D. Serantes, and D. Baldomir, "Learning from nature to improve the heat generation of iron-oxide nanoparticles for magnetic hyperthermia applications.," *Scientific reports*, vol. 3, p. 1652, 2013.

[38] E. Alphandéry, S. Faure, O. Seksek, F. Guyot, and I. Chebbi, "Chains of Magnetosomes Extracted from AMB-1 Magnetotactic Bacteria for Application in Alternative Magnetic Field Cancer Therapy.," *ACS nano*, vol. 5, no. 8, pp. 6279–6296, 2011.

[39] K. D. Bakoglidis, K. Simeonidis, D. Sakellari, G. Stefanou, and M. Angelakeris, "Size-dependent mechanisms in AC magnetic hyperthermia response of iron-oxide nanoparticles," *IEEE Transactions on Magnetics*, vol. 48, no. 4, pp. 1320–1323, 2012.

[40] C. Lang, D. Schüler, and D. Faivre, "Synthesis of magnetite nanoparticles for bio- and nanotechnology: Genetic engineering and biomimetics of bacterial magnetosomes," *Macromolecular Bioscience*, vol. 7, no. 2, pp. 144–151, 2007.

[41] N. Ginet, R. Pardoux, G. Adryanczyk, D. Garcia, C. Brutesco, and D. Pignol, "Single-step production of a recyclable nanobiocatalyst for organophosphate pesticides biodegradation using functionalized bacterial magnetosomes.," *PloS one*, vol. 6, no. 6, p. e21442, 2011.

[42] J. B. Sun, J. H. Duan, S. L. Dai, J. Ren, L. Guo, W. Jiang, and Y. Li, "Preparation and anti-tumor efficiency evaluation of doxorubicin-loaded bacterial magnetosomes: Magnetic nanoparticles as drug carriers isolated from *Magnetospirillum gryphiswaldense*," *Biotechnology and Bioengineering*, vol. 101, no. 6, pp. 1313–1320, 2008.

[43] Q. Deng, Y. Liu, S. Wang, M. Xie, S. Wu, A. Chen, and W. Wu, "Construction of a novel magnetic targeting anti-tumor drug delivery system: Cytosine arabinoside-loaded bacterial magnetosome," *Materials*, vol. 6, no. 9, pp. 3755–3763, 2013.

[44] M. R. Benoit, D. Mayer, Y. Barak, I. Y. Chen, W. Hu, Z. Cheng, S. X. Wang, D. M. Spielman, S. S. Gambhir, and A. Matin, "Visualizing implanted tumors in mice with magnetic resonance imaging using magnetotactic bacteria," *Clinical Cancer Research*, vol. 15, no. 16, pp. 5170–5177, 2009.

[45] O. Felfoul, M. Mohammadi, S. Taherkhani, D. de Lanauze, Y. Zhong Xu, D. Loghin, S. Essa, S. Jancik, D. Houle, M. Lafleur, L. Gaboury, M. Tabrizian, N. Kaou, M. Atkin, T. Vuong, G. Batist, N. Beauchemin, D. Radzioch, and S. Martel, "Magneto-aerotactic bacteria deliver drug-containing nanoliposomes to tumour hypoxic regions.," *Nature nanotechnology*, vol. 11, no. August, pp. 941–949, 2016.

[46] S. Mériaux, M. Boucher, B. Marty, Y. Lalatonne, S. Prévéral, L. Motte, C. T. Lefèvre, F. Geffroy, F. Lethimonnier, M. Péan, D. Garcia, G. Adryanczyk-Perrier, D. Pignol, and N. Ginet, "Magnetosomes, Biogenic Magnetic Nanomaterials for Brain Molecular Imaging with 17.2 T MRI Scanner," *Advanced Healthcare Materials*, vol. 4, no. 7, pp. 1076–1083, 2015.

[47] Z. Xiang, X. Yang, J. Xu, W. Lai, Z. Wang, Z. Hu, J. Tian, L. Geng, and Q. Fang, "Tumor detection using magnetosome nanoparticles functionalized with a newly screened egfr/her2 targeting peptide," *Biomaterials*, vol. 115, no. Supplement C, pp. 53 – 64, 2017.

[48] M. Boucher, F. Geffroy, S. Prévéral, L. Bellanger, E. Selingue, G. Adryanczyk-Perrier, M. Péan, C. Lefèvre, D. Pignol, N. Ginet, and S. Mériaux, "Genetically tailored magnetosomes used as MRI probe for molecular imaging of brain tumor," *Biomaterials*, vol. 121, pp. 167 – 178, 2017.

[49] L. Xiang, J. Wei, S. Jianbo, W. Guili, G. Feng, and L. Ying, "Purified and sterilized magnetosomes from *Magnetospirillum gryphiswaldense* MSR-1 were not toxic to mouse fibroblasts in vitro," *Letters in Applied Microbiology*, vol. 45, no. 1, pp. 75–81, 2007.

[50] R. ting Liu, J. Liu, J. qiong Tong, T. Tang, W.-C. Kong, X. wen Wang, Y. Li, and J. tian Tang, "Heating effect and biocompatibility of bacterial magnetosomes as potential materials used in magnetic fluid hyperthermia," *Progress in Natural Science: Materials International*, vol. 22, no. 1, pp. 31 – 39, 2012.

[51] L. Qi, X. Lv, T. Zhang, P. Jia, R. Yan, S. Li, R. Zou, Y. Xue, and L. Dai, "Cytotoxicity and genotoxicity of bacterial magnetosomes against human retinal pigment epithelium cells," *Scientific Reports*, vol. 6, no. December 2015, p. 26961, 2016.

[52] T. Revathy, M. A. Jayasri, and K. Suthindhiran, "Toxicity assessment of magnetosomes in different models," *3 Biotech*, vol. 7, p. 126, 2017.

[53] S. S. Staniland, W. Williams, N. Telling, G. Van Der Laan, A. Harrison, and B. Ward, "Controlled cobalt doping of magnetosomes in vivo.," *Nature nanotechnology*, vol. 3, no. 3, pp. 158–62, 2008.

[54] M. Tanaka, R. Brown, N. Hondow, A. Arakaki, T. Matsunaga, and S. Staniland, "Highest levels of Cu, Mn and Co doped into nanomagnetic magnetosomes through optimized biomineralisation," *Journal of Materials Chemistry*, vol. 22, no. 24, p. 11919, 2012.

[55] J. Li, N. Menguy, M.-A. Arrio, P. Sainctavit, A. Juhin, Y. Wang, H. Chen, O. Bunau, E. Otero, P. Ohresser, and Y. Pan, "Controlled cobalt doping in the spinel structure of magnetosome magnetite: new evidences from element- and site-specific X-ray magnetic circular dichroism analyses," *Journal of The Royal Society Interface*, vol. 13, no. 121, p. Article No. 20160355, 2016.

[56] D. Pignol, M. Sabaty, P. Arnoux, and J. Abbe, "Modified magnetotactic bacteria expressing a metallophore specific for cobalt and/or nickel," 2017.

[57] W. Zhou, Y. Zhang, X. Ding, Y. Liu, F. Shen, X. Zhang, S. Deng, H. Xiao, G. Yang, and H. Peng, "Magnetotactic bacteria: Promising biosorbents for heavy metals," *Applied Microbiology and Biotechnology*, vol. 95, no. 5, pp. 1097–1104, 2012.

[58] M. Tanaka, W. Knowles, R. Brown, N. Hondow, A. Arakaki, S. Baldwin, S. Staniland, and T. Matsunaga, "Biomagnetic Recovery and Bioaccumulation of Selenium Granules in Magnetotactic Bacteria," *Applied and Environmental Microbiology*, vol. 82, no. 13, pp. 3886–3891, 2016.

[59] A. M. Huízar-Félix, D. Muñoz, I. Orue, C. Magén, A. Ibarra, J. M. Barandiarán, A. Muela, and M. L. Fdez-Gubieda, "Assemblies of magnetite nanoparticles extracted from magnetotactic bacteria: A magnetic study," *Applied Physics Letters*, vol. 108, no. 6, 2016.

[60] Y. Amemiya, A. Arakaki, S. S. Staniland, T. Tanaka, and T. Matsunaga, "Controlled formation of magnetite crystal by partial oxidation of ferrous hydroxide in the presence of recombinant magnetotactic bacterial protein mms6," *Biomaterials*, vol. 28, no. 35, pp. 5381 – 5389, 2007.

[61] S. M. Bird, O. El-Zubir, A. E. Rawlings, G. J. Leggett, and S. S. Staniland, "A novel design strategy for nanoparticles on nanopatterns: interferometric lithographic patterning of Mms6 biotemplated magnetic nanoparticles," *Journal of Materials Chemistry C*, vol. 4, p. 3948, 2016.

[62] X. Jiang, J. Feng, L. Huang, Y. Wu, B. Su, W. Yang, L. Mai, and L. Jiang, "Bioinspired 1D Superparamagnetic Magnetite Arrays with Magnetic Field Perception," *Advanced Materials*, vol. 2016, pp. 1–7, 2016.

[63] U. Heyen and D. Schüler, "Growth and magnetosome formation by microaerophilic *Magnetospirillum* strains in an oxygen-controlled fermentor.," *Applied microbiology and biotechnology*, vol. 61, no. 5-6, pp. 536–44, 2003.

[64] K. T. Silva, P. E. Leão, F. Abreu, J. A. López, M. L. Gutarra, M. Farina, D. A. Bazylinski, D. M. G. Freire, and U. Lins, "Optimization of magnetosome production and growth by the magnetotactic vibrio *Magnetovibrio blakemorei* strain MV-1 through a statistics-based experimental design," *Applied and Environmental Microbiology*, vol. 79, no. 8, pp. 2823–2827, 2013.

[65] I. Kolinko, A. Lohße, S. Borg, O. Raschdorf, C. Jogler, Q. Tu, M. Pósfai, E. Tompa, J. M. Plitzko, A. Brachmann, G. Wanner, R. Müller, Y. Zhang, and D. Schüler, "Biosynthesis of magnetic nanostructures in a foreign organism by transfer of bacterial magnetosome gene clusters.," *Nature nanotechnology*, vol. 9, no. 3, pp. 193–7, 2014.

[66] S. Staniland, "Nanoparticle biosynthesis: An accommodating host.," *Nature nanotechnology*, vol. 9, no. 3, pp. 163–4, 2014.

[67] D. Serantes, K. Simeonidis, M. Angelakeris, O. Chubykalo-Fesenko, M. Marciello, M. Morales, D. Baldomir, and C. Martínez-Boubeta, "Multiplying Magnetic Hyperthermia Response by Nanoparticle Assembling," *J. Phys. Chem. C*, vol. 118, no. March, pp. 5927–5934, 2014.

[68] D. Ghosh, Y. Lee, S. Thomas, A. G. Kohli, D. S. Yun, A. M. Belcher, and K. A. Kelly, "M13-templated magnetic nanoparticles for targeted in vivo imaging of prostate cancer," *Nat. Nanotechnol.*, vol. 7, no. 10, pp. 677–682, 2012.

[69] S. R. Mishra, M. D. Dickey, O. D. Velev, and J. B. Tracy, "Selective and directional actuation of elastomer films using chained magnetic nanoparticles," *Nanoscale*, vol. 8, pp. 1309–1313, 2016.

[70] X. Kou, X. Fan, R. K. Dumas, Q. Lu, Y. Zhang, H. Zhu, X. Zhang, K. Liu, and J. Q. Xiao, "Memory effect in magnetic nanowire arrays," *Adv. Mater.*, vol. 23, no. 11, pp. 1393–1397, 2011.

[71] A. Scheffel, M. Gruska, D. Faivre, A. Linaroudis, J. M. Plitzko, and D. Schüler, "An acidic protein aligns magnetosomes along a filamentous structure in magnetotactic bacteria," *Nature*, vol. 440, no. 7080, pp. 110–114, 2006.

[72] K. Grünberg, C. Wawer, and B. M. Tebo, "A Large Gene Cluster Encoding Several Magnetosome Proteins Is Conserved in Different Species of Magnetotactic Bacteria," *Appl. Environ. Microbiol.*, vol. 67, no. 10, pp. 4573–4582, 2001.

[73] S. Mann, "Structure, Morphology, and Crystal Growth of Bacterial Magnetite," in *Magnetite Biomineralization and Magnetoreception in Organisms: A New Biomagnetism* (J. L. Kirschvink, D. S. Jones, and B. J. MacFadden, eds.), pp. 311–332, Boston, MA: Springer US, 1985.

[74] A. Körnig, M. Winklhofer, J. Baumgartner, T. P. González, P. Fratzl, and D. Faivre, "Magnetite crystal orientation in magnetosome chains," *Adv. Funct. Mater.*, vol. 24, no. 25, pp. 3926–3932, 2014.

[75] O. Glatter, "A new method for the evaluation of small-angle scattering data," *J. Appl. Crystallogr.*, vol. 10, no. 5, pp. 415–421, 1977.

[76] O. Glatter, "The interpretation of real-space information from small-angle scattering experiments," *J. Appl. Crystallogr.*, vol. 12, no. 2, pp. 166–175, 1979.

[77] B. Vestergaard and S. Hansen, "Application of Bayesian analysis to indirect Fourier transformation in small-angle scattering," *J. Appl. Crystallogr.*, vol. 39, no. 6, pp. 797–804, 2006.

[78] P. Bender, L. Bogart, O. Posth, W. Szczerba, S. Rogers, A. Castro, L. Nilsson, L. Zeng, A. Sugunan, J. Sommertune, *et al.*, "Structural and magnetic properties of multi-core nanoparticles analysed using a generalised numerical inversion method," *Sci. Rep.*, vol. 7, p. 45990, 2017.

[79] A. Hoell, A. Wiedenmann, U. Heyen, and D. Schüler ler, "Nanostructure and field-induced arrangement of magnetosomes studied by SANSPOL," *Physica B*, vol. 350, no. 1-3, pp. 309–E313, 2004.

[80] C. D. Dewhurst, I. Grillo, D. Honecker, M. Bonnaud, M. Jacques, C. Amrouni, A. Perillo-Marcone, G. Manzin, and R. Cubitt, "The small-angle neutron scattering instrument D33 at the Institut Laue–Langevin," *J. Appl. Crystallogr.*, vol. 49, pp. 1–14, 2016.

[81] P. Bender, L. Fernández Barquín, M. Fdez-Gubieda, D. González-Alonso, D. Honecker, L. Marcano, and W. Szczerba, "Spin correlation in clusters of magnetic nanoparticles. Institut Laue-Langevin (ILL). doi: 10.5291/ILL-DATA.5-53-267," 2017.

[82] D. Honecker, A. Ferdinand, F. Döbrich, C. Dewhurst, A. Wiedenmann, C. Gómez-Polo, K. Suzuki, and A. Michels, "Longitudinal polarization analysis in small-angle neutron scattering," *Eur. Phys. J. B*, vol. 76, no. 2, pp. 209–213, 2010.

[83] E. C. Stoner and E. P. Wohlfarth, "A Mechanism of Magnetic Hysteresis in Heterogeneous Alloys," *Philos. Trans. R. Soc. London, Ser. A*, vol. 240, no. 826, pp. 599–642, 1948.

[84] L. J. Geoghegan, W. T. Coffey, and B. Mulligan, "Differential Recurrence Relations for Non-Axially Symmetric Rotational Fokker-Planck Equations," *Adv. Chem. Phys.*, vol. 100, pp. 475 – 641, 1997.

[85] J. Carrey, B. Mehdaoui, and M. Respaud, "Simple models for dynamic hysteresis loop calculations of magnetic single-domain nanoparticles: Application to magnetic hyperthermia optimization," *J. Appl. Phys.*, vol. 109, p. 083921, 2011.

[86] M. Charilaou, M. Winklhofer, and A. U. Gehring, "Simulation of ferromagnetic resonance spectra of linear chains of magnetite nanocrystals," *J. Appl. Phys.*, vol. 109, no. 9, pp. 1–6, 2011.

[87] M. Charilaou, K. K. Sahu, D. Faivre, A. Fischer, I. García-Rubio, and A. U. Gehring, "Evolution of magnetic anisotropy and thermal stability during nanocrystal-chain growth," *Appl. Phys. Lett.*, vol. 99, no. 18, pp. 9–11, 2011.

[88] J. M. Thomas, E. T. Simpson, T. Kasama, and R. E. Dunin-Borkowski, "Electron holography for the study of magnetic nanomaterials," *Accounts of chemical research*, vol. 41, no. 5, pp. 665–74, 2008.

[89] F. Kronast and S. Valencia, "SPEEM : The photoemission microscope at the dedicated microfocus PGM beamline UE49-PGMa at BESSY II," *JLSRF*, vol. A90, pp. 1–6, 2016.

[90] B. Kiani, D. Faivre, and S. Klumpp, "Elastic properties of magnetosome chains," *New Journal of Physics*, vol. 17, no. 4, p. 43007, 2015.

[91] V. P. Shcherbakov, M. Winklhofer, M. Hanzlik, and N. Petersen, "Elastic stability of chains of magnetosomes in magnetotactic bacteria," *Eur. Biophys. J.*, vol. 26, no. 4, pp. 319–326, 1997.

[92] R. E. Dunin-Borkowski, M. R. McCartney, R. B. Frankel, D. A. Bazylinski, M. Posfai, and P. R. Buseck, "Magnetic microstructure of magnetotactic bacteria by electron holography," *Science*, vol. 282, p. 1868, 1998.

[93] M. J. Footer, J. W. J. Kerssemakers, J. A. Theriot, and M. Dogterom, "Direct measurement of force generation by actin filament polymerization using an optical trap," *PNAS*, vol. 104, no. 7, pp. 2181–6, 2007.

[94] A. Körnig, J. Dong, M. Bennet, M. Widdrat, J. Andert, F. D. Müller, D. Schüler, S. Klumpp, and D. Faivre, "Probing the mechanical properties of magnetosome chains in living magnetotactic bacteria," *Nano Lett.*, vol. 14, no. 8, pp. 4653–4659, 2014.

[95] J. Li, Y. Pan, Q. Liu, K. Yu-Zhang, N. Menguy, R. Che, H. Qin, W. Lin, W. Wu, N. Petersen, and X. Yang, "Biomineralization, crystallography and magnetic properties of bullet-shaped magnetite magnetosomes in giant rod magnetotactic bacteria," *Earth Planet. Sci. Lett.*, vol. 293, no. 3-4, pp. 368–376, 2010.

[96] D. N. Mastronarde, "Automated electron microscope tomography using robust prediction of specimen movements," *J. Struct. Biol.*, vol. 152, no. 1, pp. 36 – 51, 2005.

[97] J. R. Kremer, D. N. Mastronarde, and J. McIntosh, "Computer Visualization of Three-Dimensional Image Data Using IMOD," *J. Struct. Biol.*, vol. 116, no. 1, pp. 71 – 76, 1996.

[98] J. Schindelin, C. T. Rueden, M. C. Hiner, and K. W. Eliceiri, "The imageJ ecosystem: An open platform for biomedical image analysis," *Mol. Reprod. Dev.*, vol. 82, no. 7-8, pp. 518–529, 2015.

[99] E. F. Pettersen, T. D. Goddard, C. C. Huang, G. S. Couch, D. M. Greenblatt, E. C. Meng, and T. E. Ferrin, "UCSF Chimera – A visualization system for exploratory research and analysis," *J. Comput. Chem.*, vol. 25, no. 13, pp. 1605–1612, 2004.

[100] H. Gojzewski, M. Makowski, A. Hashim, P. Kopcansky, Z. Tomori, and M. Timko, "Magnetosomes on surface: An imaging study approach," *Scanning*, vol. 34, no. 3, pp. 159–169, 2012.

[101] F. Kronast, J. Schlichting, F. Radu, S. Mishra, T. Noll, and H. Dürr, "Spin-resolved photoemission microscopy and magnetic imaging in applied magnetic fields," *Surf. Interface Anal.*, vol. 42, no. 10-11, pp. 1532–1536, 2010.

[102] C. Jogler and D. Schüler, "Genomics, Genetics, and Cell Biology of Magnetosome Formation," *Annual Review of Microbiology*, vol. 63, no. 1, pp. 501–521, 2009.

[103] S. Barber-Zucker and R. Zarivach, "A look into the biochemistry of Magnetosome biosynthesis in magnetotactic bacteria," *ACS Chemical Biology*, vol. 12, no. 1, pp. 13–22, 2017.

[104] E. Cornejo, P. Subramanian, Z. Li, G. J. Jensen, and A. Komeili, "Dynamic remodeling of the magnetosome membrane is triggered by the initiation of biomineralization," *mBio*, vol. 7, no. 1, pp. 1–9, 2016.

[105] D. Murat, A. Quinlan, H. Vali, and A. Komeili, "Comprehensive genetic dissection of the magnetosome gene island reveals the step-wise assembly of a prokaryotic organelle," *Proceedings of the National Academy of Sciences*, vol. 107, no. 12, pp. 5593–5598, 2010.

[106] J. Baumgartner, A. Dey, P. H. H. Bomans, C. Le Coadou, P. Fratzl, N. a. J. M. Sommerdijk, and D. Faivre, "Nucleation and growth of magnetite from solution.," *Nature materials*, vol. 12, no. 4, pp. 310–4, 2013.

[107] J. Baumgartner and D. Faivre, "Magnetite Biomineralization in Bacteria," in *Molecular Biomineralization* (W. E. G. Müller, ed.), vol. 52 of *Progress in Molecular and Subcellular Biology*, ch. 1, pp. 3–27, Springer Berlin Heidelberg, 2011.

[108] R. B. Frankel, G. C. Papaefthymiou, R. P. Blakemore, and W. O'Brien, "Fe_3O_4 precipitation in magnetotactic bacteria," *Biochimica et Biophysica Acta (BBA) - Molecular Cell Research*, vol. 763, no. 2, pp. 147–159, 1983.

[109] D. Faivre, L. H. Böttger, B. F. Matzanke, and D. Schüler, "Intracellular magnetite biomineralization in bacteria proceeds by a distinct pathway involving membrane-bound ferritin and an iron(II) species.," *Angewandte Chemie (International ed. in English)*, vol. 46, no. 44, pp. 8495–9, 2007.

[110] A. Arakaki, J. Webb, and T. Matsunaga, "A Novel Protein Tightly Bound to Bacterial Magnetic Particles in *Magnetospirillum magneticum* Strain AMB-1," *Journal of Biological Chemistry*, vol. 278, no. 10, pp. 8745–8750, 2003.

[111] S. Watanabe, M. Yamanaka, A. Sakai, K. Sawada, and T. Iwasa, "Laser Raman Spectroscopic Study on Magnetite Formation in Magnetotactic Bacteria," *Materials Transactions*, vol. 49, no. 4, pp. 874–878, 2008.

[112] S. Staniland, B. Ward, A. Harrison, G. van der Laan, and N. Telling, "Rapid magnetosome formation shown by real-time x-ray magnetic circular dichroism," *Proceedings of the National Academy of Sciences*, vol. 104, no. 49, pp. 19524–19528, 2007.

[113] M. L. Fdez-Gubieda, A. Muela, J. Alonso, A. García Prieto, L. Olivi, J. M. Barandiarán, and R. Fernández-Pacheco, "Magnetite Biomineralization in *Magnetospirillum gryphiswaldense*: Time-Resolved Magnetic and Structural Studies," *ACS nano*, vol. 7, pp. 3297–3305, 2013.

[114] E. C. Theil, "Ferritin: Structure, Gene Regulation, and Cellular Function in Animals, Plants, and Microorganisms," *Annual Review of Biochemistry*, vol. 56, no. 1, pp. 289–315, 1987.

[115] J. L. Smith, "The Physiological Role of Ferritin-Like Compounds in Bacteria," *Critical Reviews in Microbiology*, vol. 30, no. 3, pp. 173–185, 2004.

[116] E. C. Theil, "Ferritin: The Protein Nanocage and Iron Biomineral in Health and in Disease," *Inorganic Chemistry*, vol. 52, no. 21, pp. 12223–12233, 2013.

[117] E. C. Theil, R. K. Behera, and T. Tosha, "Ferritins for chemistry and for life," *Coordination Chemistry Reviews*, vol. 257, no. 2, pp. 579–586, 2013.

[118] N. E. Le Brun, A. Crow, M. E. Murphy, A. G. Mauk, and G. R. Moore, "Iron core mineralisation in prokaryotic ferritins," *Biochimica et Biophysica Acta (BBA) - General Subjects*, vol. 1800, no. 8, pp. 732–744, 2010.

[119] A. García-Prieto, J. Alonso, D. Muñoz, L. Marcano, A. Abad Díaz de Cerio, R. Fernández de Luis, I. Orue, O. Mathon, A. Muela, and M. L. Fdez-Gubieda, "On the mineral core of ferritin-like proteins: structural and magnetic characterization," *Nanoscale*, vol. 8, no. 2, pp. 1088–1099, 2016.

[120] L. Elizabeth Bertani, J. S. Huang, B. A. Weir, and J. L. Kirschvink, "Evidence for two types of subunits in the bacterioferritin of *Magnetospirillum magnetotacticum*," *Gene*, vol. 201, no. 1-2, pp. 31–36, 1997.

[121] The UniProt Consortium, "UniProt: the universal protein knowledgebase," *Nucleic Acids Research*, vol. 45, no. D1, pp. D158–D169, 2017.

[122] L. E. Bevers and E. C. Theil, "Maxi- and Mini-Ferritins: Minerals and Protein Nanocages," in *Molecular Biomineralization* (W. E. G. Müller, ed.), vol. 52, pp. 29–47, Berlin, Heidelberg: Springer Berlin Heidelberg, 2011.

[123] S. C. Andrews, P. M. Harrison, and J. R. Guest, "Cloning, sequencing, and mapping of the bacterioferritin gene (bfr) of Escherichia coli K-12.," *Journal of bacteriology*, vol. 171, no. 7, pp. 3940–3947, 1989.

[124] D. Schüler, R. Uhl, and E. Bäuerlein, "A simple light scattering method to assay magnetism in *Magnetospirillum gryphiswaldense*," *FEMS microbiology letters*, vol. 132, no. 1-2, pp. 139–145, 1995.

[125] C. A. Schneider, W. S. Rasband, and K. W. Eliceiri, "NIH Image to ImageJ: 25 years of image analysis," *Nature methods*, vol. 9, no. 7, p. 671, 2012.

[126] P. M. Harrison and P. Arosio, "The ferritins: molecular properties, iron storage function and cellular regulation," *Biochimica et Biophysica Acta (BBA) - Bioenergetics*, vol. 1275, no. 3, pp. 161–203, 1996.

[127] A. J. Hudson, S. C. Andrews, C. Hawkins, J. M. Williams, M. Izuhara, F. C. Meldrum, S. Mann, P. M. Harrison, and J. R. Guest, "Overproduction, purification and characterization of the Escherichia coli ferritin," *European Journal of Biochemistry*, vol. 218, no. 3, pp. 985–995, 1993.

[128] D. Faivre, A. Fischer, I. Garcia-Rubio, G. Mastrogiacomo, and A. U. Gehring, "Development of Cellular Magnetic Dipoles in Magnetotactic Bacteria," *Biophysical Journal*, vol. 99, no. 4, pp. 1268–1273, 2010.

[129] L. Marcano, A. García-Prieto, D. Muñoz, L. Fernández Barquín, I. Orue, J. Alonso, A. Muela, and M. Fdez-Gubieda, "Influence of the bacterial growth phase on the magnetic properties of magnetosomes synthesized by *Magnetospirillum gryphiswaldense*," *Biochimica et Biophysica Acta (BBA) - General Subjects*, vol. 1861, no. 6, pp. 1507–1514, 2017.

[130] R. J. Pollard, C. M. Cardile, D. G. Lewis, and L. J. Brown, "Characterization of FeOOH polymorphs and ferrihydrite using low-temperature, applied-field, Mössbauer spectroscopy," *Clay Minerals*, vol. 27, no. 01, pp. 57–71, 1992.

[131] M. L. Fdez-Gubieda, A. García-Prieto, J. Alonso, and C. Meneghini, "X-Ray Absorption Fine Structure Spectroscopy in Fe Oxides and Oxyhydroxides," *Iron Oxides: From Nature to Applications*, pp. 397–422, 2016.

[132] M. Wilke, F. Farges, P.-E. Petit, G. E. Brown Jr., and F. Martin, "Oxidation state and coordination of Fe in minerals: An Fe K-XANES spectroscopy study," *American Mineralogist*, vol. 86, pp. 714–730, 2001.

[133] S. Pascarelli, "Studies of Matter at Extreme Conditions," in *Synchrotron Radiation* (S. Mobilio, F. Boscherini, and C. Meneghini, eds.), pp. 737–760, Berlin, Heidelberg: Springer Berlin Heidelberg, 2015.

[134] G. S. Henderson, F. M. F. de Groot, and B. J. A. Moulton, "X-ray Absorption Near-Edge Structure (XANES) Spectroscopy," *Reviews in Mineralogy and Geochemistry*, vol. 78, no. 1, pp. 75–138, 2014.

[135] A. Voegelin, R. Kaegi, J. Frommer, D. Vantelon, and S. J. Hug, "Effect of phosphate, silicate, and Ca on Fe(III)-precipitates formed in aerated Fe(II)- and As(III)-containing water studied by X-ray absorption spectroscopy," *Geochimica et Cosmochimica Acta*, vol. 74, no. 1, pp. 164–186, 2010.

[136] A. Kauko, A. T. Pulliainen, S. Haataja, W. Meyer-Klaucke, J. Finne, and A. C. Papageorgiou, "Iron Incorporation in Streptococcus suis Dps-like Peroxide Resistance Protein Dpr Requires Mobility in the Ferroxidase Center and Leads to the Formation of a Ferrihydrite-like Core," *Journal of Molecular Biology*, vol. 364, no. 1, pp. 97–109, 2006.

[137] C. R. Natoli, M. Benfatto, S. Della Longa, and K. Hatada, "X-ray absorption spectroscopy: state-of-the-art analysis," *Journal of Synchrotron Radiation*, vol. 10, no. 1, pp. 26–42, 2003.

[138] D. A. Venero, F. B. L, J. Alonso, M. L. Fdez-Gubieda, L. Rodríguez Fernández, R. Boada, and J. Chaboy, "Magnetic disorder in diluted Fe_xM_{100-x} granular thin films (M=Au, Ag, Cu; $x < 10$ at.%)," *Journal of Physics: Condensed Matter*, vol. 25, no. 27, p. 276001, 2013.

[139] J. Chaboy and S. Quartieri, "X-ray absorption at the Ca *K* edge in natural-garnet solid solutions: A full-multiple-scattering investigation," *Physical Review B*, vol. 52, no. 9, pp. 6349–6357, 1995.

[140] D. Koningsberger and R. e. Prins, *X-ray absorption: principles, applications, techniques of EXAFS, SEXAFS, and XANES*. United States: John Wiley and Sons,New York, NY, 1988.

[141] G. Bunker, *Introduction to XAFS: A Practical Guide to X-ray Absorption Fine Structure Spectroscopy*. Cambridge: Cambridge University Press, 2010.

[142] S. Calvin, *XAFS for Everyone*. Taylor & Francis, 2013.

[143] J. J. Rehr, J. J. Kas, M. P. Prange, A. P. Sorini, Y. Takimoto, and F. Vila, "Ab initio theory and calculations of X-ray spectra," *Comptes Rendus Physique*, vol. 10, no. 6, pp. 548–559, 2009.

[144] A. L. Ankudinov, B. Ravel, J. J. Rehr, and S. D. Conradson, "Real-space multiple-scattering calculation and interpretation of x-ray-absorption near-edge structure," *Physical Review B*, vol. 58, no. 12, pp. 7565–7576, 1998.

[145] G. Subías, J. García, and J. Blasco, "EXAFS spectroscopic analysis of the Verwey transition in Fe3o4," *Physical Review B*, vol. 71, no. 15, 2005.

[146] M. Newville, "*IFEFFIT* : interactive XAFS analysis and *FEFF* fitting," *Journal of Synchrotron Radiation*, vol. 8, no. 2, pp. 322–324, 2001.

[147] B. Ravel and M. Newville, "*ATHENA* , *ARTEMIS* , *HEPHAESTUS* : data analysis for X-ray absorption spectroscopy using *IFEFFIT*," *Journal of Synchrotron Radiation*, vol. 12, no. 4, pp. 537–541, 2005.

[148] J. Werckmann, J. Cypriano, C. T. Lefèvre, K. Dembelé, O. Ersen, D. A. Bazylinski, U. Lins, and M. Farina, "Localized iron accumulation precedes nucleation and growth of magnetite crystals in magnetotactic bacteria," *Scientific Reports*, vol. 7, no. 1, p. 8291, 2017.

[149] J. Baumgartner, A. Dey, P. H. H. Bomans, C. Le Coadou, P. Fratzl, N. A. J. M. Sommerdijk, and D. Faivre, "Nucleation and growth of magnetite from solution," *Nature Materials*, vol. 12, no. 4, pp. 310–314, 2013.

[150] T. Borch, Y. Masue, R. K. Kukkadapu, and S. Fendorf, "Phosphate Imposed Limitations on Biological Reduction and Alteration of Ferrihydrite," *Environmental Science & Technology*, vol. 41, no. 1, pp. 166–172, 2007.

[151] P. A. van Aken, B. Liebscher, and V. J. Styrsa, "Quantitative determination of iron oxidation states in minerals using Fe L 2,3 -edge electron energy-loss near-edge structure spectroscopy," *Physics and Chemistry of Minerals*, vol. 25, no. 5, pp. 323–327, 1998.

[152] E. Firlar, T. Perez-Gonzalez, A. Olszewska, D. Faivre, and T. Prozorov, "Following iron speciation in the early stages of magnetite magnetosome biomineralization," *Journal of Materials Research*, pp. 1–9, 2016.

[153] T. Prozorov, T. Perez-Gonzalez, C. Valverde-Tercedor, C. Jimenez-Lopez, A. Yebra-Rodriguez, A. Körnig, D. Faivre, S. K. Mallapragada, P. A. Howse, D. A. Bazylinski, and R. Prozorov, "Manganese incorporation into the magnetosome magnetite: magnetic signature of doping," *European Journal of Mineralogy*, vol. 26, no. 4, pp. 457–471, 2014.

[154] A. Arakaki, F. Masuda, Y. Amemiya, T. Tanaka, and T. Matsunaga, "Control of the morphology and size of magnetite particles with peptides mimicking the Mms6 protein from magnetotactic bacteria," *Journal of Colloid and Interface Science*, vol. 343, no. 1, pp. 65–70, 2010.

[155] J. M. Galloway, A. Arakaki, F. Masuda, T. Tanaka, T. Matsunaga, and S. S. Staniland, "Magnetic bacterial protein Mms6 controls morphology, crystallinity and magnetism of cobalt-doped magnetite nanoparticles in vitro," *Journal of Materials Chemistry*, vol. 21, no. 39, p. 15244, 2011.

[156] S. Larumbe, C. Gomez-Polo, J. I. Pérez-Landazábal, A. García-Prieto, J. Alonso, M. L. Fdez-Gubieda, D. Cordero, and J. Gómez, "Ni Doped Fe_3O_4 Magnetic Nanoparticles," *Journal of Nanoscience and Nanotechnology*, vol. 12, no. 3, pp. 2652–2660, 2012.

[157] M. Veverka, P. Veverka, O. Kaman, A. Lančok, K. Závěta, E. Pollert, K. Knížek, J. Boháeek, M. Beneš, P. Kašpar, E. Duguet, and S. Vasseur, "Magnetic heating by cobalt ferrite nanoparticles," *Nanotechnology*, vol. 18, no. 34, p. 345704, 2007.

[158] I. Sharifi, H. Shokrollahi, and S. Amiri, "Ferrite-based magnetic nanofluids used in hyperthermia applications," *Journal of Magnetism and Magnetic Materials*, vol. 324, no. 6, pp. 903–915, 2012.

[159] D. A. Bazylinski, A. J. Garratt-Reed, A. Abedi, and R. B. Frankel, "Copper association with iron sulfide magnetosomes in a magnetotactic bacterium," p. 8, 1993.

[160] R. Li, "A study of the magnetotactic bacteria and their magnetosomes from a section of loess in the shanxi province," *Diqiu Huaxue*, vol. 25, pp. 251–254, 1996.

[161] C. N. Keim, U. Lins, and M. Farina, "Manganese in biogenic magnetite crystals from magnetotactic bacteria," *FEMS Microbiology Letters*, vol. 292, no. 2, pp. 250–253, 2009.

[162] T. Pérez-Gonzalez, T. Prozorov, A. Yebra-Rodríguez, D. Bazylinski, and C. Jimenez-López, "Mn incorporation in magnetosomes: New possibilities for the nanotechnological applications of biomagnetite," *Macla (Sociedad Española de Mineralogía)*, vol. 13, p. 171, 2010.

[163] L. Marcano, D. Muñoz, R. Martín-RodrÃguez, I. n. Orue, J. Alonso, A. García-Prieto, A. Serrano, S. Valencia, R. Abrudan, L. Fernández Barquín, A. García-Arribas, A. Muela, and M. L. Fdez-Gubieda, "Magnetic Study of Co-Doped Magnetosome Chains," *The Journal of Physical Chemistry C*, vol. 122, no. 13, pp. 7541–7550, 2018.

[164] B. L. Vallee, "Perspectives in Biochemistry," p. 13, 1990.

[165] L. P. Wackett, A. G. Dodge, and L. B. M. Ellis, "Microbial Genomics and the Periodic Table," *Applied and Environmental Microbiology*, vol. 70, no. 2, pp. 647–655, 2004.

[166] M. R. Bruins, S. Kapil, and F. W. Oehme, "Microbial Resistance to Metals in the Environment," *Ecotoxicology and Environmental Safety*, vol. 45, no. 3, pp. 198–207, 2000.

[167] D. H. Nies and S. Silver, eds., *Molecular microbiology of heavy metals*. No. 6 in Microbiology monographs, Berlin ; New York: Springer, 2007.

[168] D. Schüler, "Formation of Magnetosomes in Magnetotactic Bacteria," *Journal of Molecular Microbiology and Biotechnology*, vol. 1, no. 1, pp. 79–86, 1999.

[169] G. R. Castro, "Optical design of the general-purpose Spanish X-ray beamline for absorption and diffraction," *Journal of synchrotron radiation*, vol. 5, no. 3, pp. 657–660, 1998.

[170] S. Pascarelli, "Studies of Matter at Extreme Conditions," in *Synchrotron Radiation* (S. Mobilio, F. Boscherini, and C. Meneghini, eds.), pp. 737–760, Berlin, Heidelberg: Springer Berlin Heidelberg, 2015.

[171] E. Mazarío, A. Mayoral, E. Salas, N. Menéndez, P. Herrasti, and J. Sánchez-Marcos, "Synthesis and characterization of manganese ferrite nanoparticles obtained by electrochemical/chemical method," *Materials & Design*, vol. 111, pp. 646–650, 2016.

[172] D. Carta, M. F. Casula, G. Mountjoy, and A. Corrias, "Formation and cation distribution in supported manganese ferrite nanoparticles: an X-ray absorption study," *Physical Chemistry Chemical Physics*, vol. 10, no. 21, p. 3108, 2008.

[173] X. Liang, Y. Zhong, S. Zhu, H. He, P. Yuan, J. Zhu, and Z. Jiang, "The valence and site occupancy of substituting metals in magnetite spinel structure $Fe_{3-x}m_xo_4$ (M = Cr, Mn, Co and Ni) and their influence on thermal stability: An XANES and TG-DSC investigation," *Solid State Sciences*, vol. 15, pp. 115–122, 2013.

[174] A. Kuzmin, S. Larcheri, and F. Rocca, "Zn K-edge XANES in nanocrystalline ZnO," *Journal of Physics: Conference Series*, vol. 93, p. 012045, 2007.

[175] J. Fock, L. K. Bogart, D. González-Alonso, J. I. Espeso, M. F. Hansen, M. Varón, C. Frandsen, and Q. A. Pankhurst, "On the 'centre of gravity' method for measuring the composition of magnetite/maghemite mixtures, or the stoichiometry of magnetite-maghemite solid solutions, via ^{57} Fe Mössbauer spectroscopy," *Journal of Physics D: Applied Physics*, vol. 50, no. 26, p. 265005, 2017.

[176] H. Fischer, G. Mastrogiacomo, J. F. Loffler, R. J. Warthmann, P. G. Weidler, and A. U. Gehring, "Ferromagnetic resonance and magnetic characteristics of intact magnetosome chains in *Magnetospirillum gryphiswaldense*," *Earth and Planetary Science Letters*, vol. 270, no. 3-4, pp. 200–208, 2008.

[177] H. Kronmuller and F. Walz, "Magnetic after-effects in Fe $_3$ O $_4$ and vacancy-doped magnetite," *Philosophical Magazine Part B*, vol. 42, no. 3, pp. 433–452, 1980.

[178] A. R. Muxworthy and E. McClelland, "Review of the low-temperature magnetic properties of magnetite from a rock magnetic perspective," *Geophysical Journal International*, vol. 140, no. 1, pp. 101–114, 2000.

[179] J. Grabis, A. Nefedov, and H. Zabel, "Diffractometer for soft x-ray resonant magnetic scattering," *Review of Scientific Instruments*, vol. 74, no. 9, pp. 4048–4051, 2003.

[180] R. Abrudan, F. Brüssing, R. Salikhov, J. Meermann, I. Radu, H. Ryll, F. Radu, and H. Zabel, "ALICE-An advanced reflectometer for static and dynamic experiments in magnetism at synchrotron radiation facilities," *Review of Scientific Instruments*, vol. 86, no. 6, p. 063902, 2015.

[181] G. van der Laan and A. I. Figueroa, "X-ray magnetic circular dichroismâ"A versatile tool to study magnetism," *Coordination Chemistry Reviews*, vol. 277-278, pp. 95–129, 2014.

[182] R. A. D. Pattrick, G. Van Der Laan, C. M. B. Henderson, P. Kuiper, E. Dudzik, and D. J. Vaughan, "Cation site occupancy in spinel ferrites studied by X-ray magnetic circular dichroism: developing a method for mineralogists," *European Journal of Mineralogy*, vol. 14, no. 6, pp. 1095–1102, 2002.

[183] E. Stavitski and F. M. de Groot, "The CTM4xas program for EELS and XAS spectral shape analysis of transition metal L edges," *Micron*, vol. 41, no. 7, pp. 687–694, 2010.

[184] C. I. Pearce, C. M. B. Henderson, N. D. Telling, R. A. D. Pattrick, D. J. Vaughan, J. M. Charnock, E. Arenholz, F. Tuna, V. S. Coker, and G. van der Laan, "Iron site occupancies in magnetite-ulvospinel solid solution: A new approach using XMCD," *American Mineralogist*, 2009.

[185] A. M. Huizar-Felix, D. Muñoz, I. Orue, C. Magen, A. Ibarra, J. M. Barandiaran, A. Muela, and M. L. Fdez-Gubieda, "Assemblies of magnetite nanoparticles extracted from magnetotactic bacteria: A magnetic study," *Applied Physics Letters*, vol. 108, no. 6, p. 063109, 2016.

[186] M. Charilaou, J. Kind, I. García-Rubio, D. Schüler, and A. U. Gehring, "Magnetic anisotropy of non-interacting collinear nanocrystal-chains," *Appl. Phys. Lett.*, vol. 104, no. 21, p. 112406, 2014.

[187] "Magnetic anisotropy and Verwey transition of magnetosome chains in *Magnetospirillum gryphiswaldense*: Magnetic anisotropy and Verwey transition," vol. 187.

[188] I. Orue, L. Marcano, P. Bender, A. García-Prieto, S. Valencia, M. A. Mawass, D. Gil Carton, D. Alba Venero, D. Honecker, A. García-Arribas, L. Fernández Barquín, A. Muela, and M. L. Fdez-Gubieda, "Configuration of the magnetosome chain: a natural magnetic nanoarchitecture," *Nanoscale*, 2018.

[189] L. R. Bickford, J. M. Brownlow, and R. F. Penoyer, "Magnetocrystalline anisotropy in cobalt-substituted magnetite single crystals," *Proceedings of the IEE-Part B: Radio and Electronic Engineering*, vol. 104, no. 5S, pp. 238–244, 1957.

[190] K. Abe, Y. Miyamotto, and S. Chikazumi, "Magnetocrystalline Anisotropy of Low Temperature Phase of Magnetite," *Journal of the Physical Society of Japan*, vol. 41, no. 6, 1976.

[191] M. Tachiki, "Origin of the magnetic anisotropy energy of cobalt ferrite," *Progress of Theoretical Physics*, vol. 23, no. 6, pp. 1055–1072, 1960.

[192] Q. Zhang, I. Castellanos-Rubio, R. Munshi, I. Orue, B. Pelaz, K. I. Gries, W. J. Parak, P. del Pino, and A. Pralle, "Model Driven Optimization of Magnetic Anisotropy of Exchange-Coupled Core-Shell Ferrite Nanoparticles for Maximal Hysteretic Loss," *Chemistry of Materials*, vol. 27, no. 21, pp. 7380–7387, 2015.

List of Figures

1.1 Schematic model of magnetotaxis in the oxic-anoxic transition zone (OATZ). 10
1.2 TEM image of diversity of magnetotactic bacteria and magnetosomes. 10
1.3 Electron micrographs of cells and magnetosomes of *Magnetospirillum gryphiswaldense*. 12
1.4 M(T) curve of *M. grysphiswaldense* and Verwey transition. 13
1.5 Crystal structure of magnetite. 14
1.6 Applications diagram. 14

2.1 Electron cryotomography (ECT) of magnetosome chains. 24
2.2 Electron cryotomography (ECT) of extracted magnetosomes. 24
2.3 Magnetization curve of the colloidal dispersion of bacteria and sketches of the two-step magnetization process either due to the misalignment of the magnetization with the chain axis or owing to the angular dispersion of cells in the colloid. 26
2.4 1D scattering intensities measured by SAXS and SANS and pair distance distribution functions $P(r)$. 27
2.5 TEM image of bacteria arranged in a 2D configuration with their chain axes either random or oriented along the aligned magnetic field 29
2.6 Hysteresis loops of random and oriented bacteria in 3D and 2D arrangements. 30
2.7 Schematic representation of a uniaxial single domain magnetic nanoparticle (MNP) and ilustration of the energy landscape as function of θ in the presence of arbitrary fixed external magnetic field. 32
2.8 Polar (α) and azimuthal (λ) angles defining the orientation of the external field relative to the chain axis. 33
2.9 H 34
2.10 Hysteresis loops of random and oriented bacteria in 3D and 2D arrangements compared to simulation considering an uniaxial easy axis $\hat{u}_{uni}$ tilted 25° with the chain axis. 35
2.11 X-ray photoemission electron microscopy (XPEEM) images and hysteresis loops of randomly arranged magnetosomes and oriented magnetosomes. 37
2.12 Equilibrium configuration of the magnetosome chain. Schematic representation of two competing mechanisms. 39

2.13 Sketch showing the orientation of the magnetic dipoles and the elastic force acting on them, and schematic representation of the magnetic dipoles and the three independent variables used in the simulation. . . 40
2.14 Experimental reconstructions of the magnetosome chains obtained from ECT imaging compared to three stable solutions (n=1,2,3) for the chain patterns. 41
2.15 2D projection on the *yz* plane of the magnetic dipoles configuration. . . 42
2.16 Chain geometries simulated for the three stable solution (n=1, 2, 3) for different values of the elastic constant. 43
2.17 Schematic representation of the SAXS and SANS experiment. 45
2.18 XMCD mechanism diagram and schematic drawing of the photoemission electron microscope installed the BESSY II storage ring. 47

3.1 Coefficient of magnetically induced differential light scattering (C_{mag}) as a function of the biomineralization time. 53
3.2 TEM images of *E. coli* overexpressing Bfr and size histograms. 54
3.3 TEM images and size histograms at several time steps of the biomineralization process. 54
3.4 X-ray absorption spectrum of magnetite biomineralized by *M. gryphiswaldense* bacterium. The two characteristic regions, near-edge (XANES) and extended (EXAFS), are indicated. 56
3.5 Comparison of the normalized XANES spectra of bacteria at t=20 min after Fe incubation, presented by Fdez-Gubieda et al.[113], with inorganic ferrihydrite and with *E. coli* overexpressing Bfr. And XANES spectra of bacteria at t=1440 min compared to inorganic magnetite. . . 57
3.6 Normalized XANES spectra at Fe *K*-edge obtained from the samples at specific times after the Fe incubation. 58
3.7 Normalized XANES spectra of several Fe compounds: FeO (Fe^{2+}), Fe(III)-citrate (Fe^{3+}), ferrihydrite (Fe^{3+}) and magnetite (Fe^{2+},Fe^{3+}). . . 58
3.8 Linear combination fits of normalized XANES spectra at the different times after Fe incubation considering Bfr and magnetite phases as references and evolution of the atomic fraction of Fe in Bfr and magnetite phases along the biomineralization process. 60
3.9 Schematic representation of the photoelectron wave. 61
3.10 EXAFS spectra and Fourier transforms of Bfr and samples at specific times after the iron incubation. 62
3.11 Evolution of coordination numbers and interatomic distances obtained by EXAFS fitting as function of the atomic fraction of magnetite. 64
3.12 HRTEM image and Fourier transform of *E. coli* overexpressing bacterioferrtin. 66
3.13 HRTEM images and Fourier transform of selected regions of ultrathin sections of *M. gryphiswaldense* at t=60 min. 67
3.14 TEM image of a *M. gryphiswaldense* cell at t=60 min after the iron incubation and Fe $L_{2,3}$-edge EEL spectra of the particles shown compared to Fe-references. 70
3.15 Integral peak intensity ratio I(L_3)/I(L_2) as function of the $Fe^{3+}/\sum Fe$ using two integrating windows 2 eV width. 71

3.16 Schematic drawing of the proposal for the magnetosome biomineralization process. . . . 72
3.17 Spectrophotometer and C_{mag} setup and schematic representations of cell configuration regarding to the incoming light beam. . . . 73
3.18 Schematic representation of the x-ray absorption mechanism of an Fe 1*s* electron (*K*-edge). . . . 74
3.19 Standard set-up of XAFS beamline in transmission and fluorescence mode. . . . 75

4.1 Optical density (OD) measured at 565 nm as a function of Mn^{2+}, Co^{2+}, Ni^{2+}, Cu^{2+} and Zn^{2+} concentrations. . . . 79
4.2 Optical density (OD) measured at 565 nm as a function of Fe^{3+} concentration for set Mn^{2+}, Co^{2+}, Ni^{2+}, Cu^{2+} and Zn^{2+} concentrations. . . . 80
4.3 Representative TEM images and size distributions for control and M-doped magnetosomes. . . . 82
4.4 Comparison of the number of particle per chain in the M-doped samples. . . . 83
4.5 EDS analysis carried out on small clusters of M-doped extracted magnetosomes. . . . 85
4.6 EDS measurements performed on individual Co-doped magnetosomes extracted from bacteria. . . . 86
4.7 EDS measurements performed on individual magnetosomes inside a bacterium grown in a Co-supplemented medium. . . . 86
4.8 Normalized Fe-*K*-edge XANES spectra of control magnetosomes (pure magnetite) and M-doped magnetosomes. . . . 88
4.9 Normalized XANES spectra at the different M *K*-edges. . . . 90
4.10 Linear combination fit of Zn-doped magnetosomes XANES spectrum by considering 71% ZnO and 29% $ZnFe_2O_4$. . . . 91
4.11 Magnetization curves measured at 50 mT for the control, Mn and Co-doped magnetosome chains. . . . 93
4.12 Hysteresis loops of the control, Mn and Co-doped magnetosome chains measured at 300 K, 110 K and 30 K. Coercive field ($\mu_0 H_c$) and e) reduced remanence magnetization (M_r/M_s) comparison as a function of temperature. . . . 94
4.13 XAS and XMCD spectra at Fe and Co $L_{2,3}$-edges of control magnetosomes and Co-doped magnetosomes. . . . 96
4.14 Element-specific hysteresis loops measured at 5K by XMCD at Fe and Co $L_{2,3}$-edge of control and Co-doped magnetosomes. . . . 97
4.15 Schematic representation of an individual magnetosome where x, y and z conform the coordinate axes selected in the simulations coincident to $\langle 100 \rangle$ directions. . . . 97
4.16 Hysteresis loops of the control and Co-doped magnetosome chains measured at (a) 300 K, (b) 110 K and (c) 30 K compared to simulated hysteresis loops. . . . 99
4.17 Temperature evolution of the anisotropy constants for (a) control magnetosomes and (b) Co-doped magnetosomes. . . . 100

4.18 Zero-field energy landscapes at 300, 110 and 30 K of the control and Co-doped magnetosomes obtained from the simulations. 100
4.19 Image of a microplate with the employed multi-channel pipete, schematic representation of microplate with the increasing metal concentrations MIC assay and schematic drawing of the microplate reader. 102

List of Tables

3.1 Integral peak intensity ratio I(L_3)/I(L_2) obtained from EELS. 70

4.1 Metal concentration values added to the growth media derived from the MIC assays. 80
4.2 Metal concentration values registered in the growth media by ICP-AES. 81